







UNIVERSITÀ POLITECNICA DELLE MARCHE  
SCUOLA DI DOTTORATO DI RICERCA IN SCIENZE DELL'INGEGNERIA  
CORSO DI DOTTORATO IN INGEGNERIA CIVILE, AMBIENTALE, EDILE E  
ARCHITETTURA

---

# On the hydro-morphodynamics of river mouths: the role of waves

Ph.D. Dissertation of:  
**Lorenzo Melito**

Advisor:  
**Prof. Maurizio Brocchini**

Coadvisor:  
**Dott. Giovanna Darvini**

Curriculum Supervisor:  
**Prof. Stefano Lenci**





UNIVERSITÀ POLITECNICA DELLE MARCHE  
SCUOLA DI DOTTORATO DI RICERCA IN SCIENZE DELL'INGEGNERIA  
CORSO DI DOTTORATO IN INGEGNERIA CIVILE, AMBIENTALE, EDILE E  
ARCHITETTURA

---

# On the hydro-morphodynamics of river mouths: the role of waves

Ph.D. Dissertation of:  
**Lorenzo Melito**

Advisor:  
**Prof. Maurizio Brocchini**

Coadvisor:  
**Dott. Giovanna Darvini**

Curriculum Supervisor:  
**Prof. Stefano Lenci**

---

UNIVERSITÀ POLITECNICA DELLE MARCHE  
SCUOLA DI DOTTORATO DI RICERCA IN SCIENZE DELL'INGEGNERIA  
FACOLTÀ DI INGEGNERIA  
Via Brecce Bianche – 60131 Ancona (AN), Italy





# Acknowledgments

I would like to thank my advisors, Prof. Maurizio Brocchini and Dr. Giovanna Darvini, and all the colleagues at the department DICEA, for entrusting me with the opportunity to test myself on this project, for the knowledge, the directions, the sincere suggestions and critiques.

A special thanks goes to Dr. Matteo Postacchini for his continuous encouragement and motivation, for the thoughtful discussions, and for bearing with my doubts and pointless questions in the last three years. This thesis would have been much worse without his essential support.

My gratitude to Prof. Enrico Foti and Prof. Riccardo Briganti for reviewing the thesis and providing useful suggestions.

My heartfelt thanks to (in strict alphabetical order!) Carlo, Eleonora, Federica, Francesco, Gianluca, Giulia, Giulia, Marco, Martina, Paolo, and all the friends and colleagues that accompanied me in the harsh path to the PhD degree, for the moral support, the company, and the good laughs.

To Tommaso, because he knows.

Last but not least, my endless gratitude to my family. In spite of the rough times, we are still here.

*Ancona, February 2018*

Lorenzo Melito



# Abstract

In the present thesis a numerical analysis of the role of wave forcing on the hydrodynamics, sediment transport and vorticity patterns in inlets and estuary mouths is proposed.

A novel solver for the hydro-morphodynamics of shallow flows in presence of an estuary is described. The solver builds upon a previous robust finite-volume model for shallow waters by Brocchini et al. [1] and is complemented by a suitable routine for the inclusion of simplified estuarine inlets at a certain portion of the computational domain boundary. The estuarine input is imposed at all nodes of the numerical inlet as a prescribed time series of water elevation and/or fluid velocity. A simple and robust mesher for the generation of computational meshes from bathymetric surveys datasets has also been devised, in order to represent real-case bottom profiles for use in numerical simulations.

The performance of the estuarine solver is tested against two sets of numerical trials. The first set of tests aims at reproducing the structure of wave-current interaction, morphodynamic patterns and vorticity at an idealized inlet configuration, in similarity of the numerical campaign performed by Olabarrieta et al. [2]. With the second type of tests the morphological evolution at the estuary of the Misa River, Senigallia, Italy are reproduced.

The model is generally capable of describing the main features of the investigated flows, although the capability of modelling sediment transport and the related morphological variations of real case scenarios need some improvement.



# Contents

<b>1</b>	<b>Introduction</b>	<b>1</b>
1.1	Estuaries . . . . .	1
1.2	Classical definitions for estuaries . . . . .	1
1.3	Classification of estuaries . . . . .	3
1.3.1	Classification based on tidal range . . . . .	3
1.3.2	Classification based on salinity . . . . .	5
1.3.3	Classification based on dominant processes . . . . .	6
1.4	The influence of waves on estuary mouths and inlets . . . . .	12
1.5	Numerical modeling of estuaries . . . . .	14
<b>2</b>	<b>The hydro-morphodynamic numerical model</b>	<b>17</b>
2.1	The nonlinear shallow water equations . . . . .	17
2.2	The Exner equation . . . . .	18
2.3	The complete system . . . . .	18
2.4	The numerical solver . . . . .	22
2.4.1	The hydrodynamic module . . . . .	22
2.4.2	The morphodynamic module . . . . .	34
2.4.3	The LES model . . . . .	36
2.4.4	The estuary model . . . . .	39
2.4.5	Mesh generation . . . . .	45
<b>3</b>	<b>Numerical tests</b>	<b>51</b>
3.1	A simple wave propagation test . . . . .	52
3.2	Wave-current interaction on a simplified inlet . . . . .	53
3.3	Estuarine morphodynamics at the Misa River mouth . . . . .	57
<b>4</b>	<b>Results and discussion</b>	<b>61</b>
4.1	A simple wave propagation test . . . . .	61
4.2	Wave-current interaction on a simplified inlet . . . . .	63
4.2.1	Interaction of waves, currents, and morphology . . . . .	63
4.2.2	Morphodynamic patterns . . . . .	70
4.2.3	Vorticity . . . . .	72
4.3	Estuarine morphodynamics at the Misa River mouth . . . . .	81
<b>5</b>	<b>In progress: a bottom boundary layer model</b>	<b>85</b>



# List of Figures

1.1	Variation of coastal and estuarine morphological features with respect to the extension of tidal range, in medium wave condition. Adapted from Hayes, 1975 . . . . .	4
1.2	Classification of estuaries based on salinity gradient and consequent water stratification. The black lines are isohalines, i.e. lines connecting points with the same salinity. Adapted from Valle-Levinson, 2010 . . . . .	7
1.3	Distribution of energy types and main morphological features in a simplified wave-dominated estuary. Adapted from Dalrymple et al., 1992 . . . . .	8
1.4	Distribution of energy types and main morphological features in a simplified tide-dominated estuary. Adapted from Dalrymple et al., 1992 . . . . .	9
1.5	Tripartite classification scheme of coastal facies based on the relative importance of river, wave, and tide action. Adapted from Boyd et al., 1992 . . . . .	11
1.6	An example of evolutionary process of estuarine environments. The gradual progradation of coasts corresponds to a movement towards the back of the prism; a transgressive behavior is represented by a movement towards the front of the prism. Adapted from Boyd et al., 1992 . . . . .	11
1.7	Range of main shallow-water coastal depositional features, arranged as a function of tidal and wave power. Adapted from Boyd et al., 1992 . . . . .	12
2.1	Schematic of the nearshore. . . . .	19
2.2	Flow chart of the numerical integration procedure. . . . .	22
2.3	Sketch of the control volume $R$ used for the $x - t$ domain discretization and the integral form of the monodimensional homogeneous system $H_x$ (2.9). . . . .	24
2.4	Representation of the averaged variables in equation (2.17) along the boundary of a control volume $R$ . . . . .	25

List of Figures

2.5	Solution of the Riemann problem (2.18). (a): complete structure of the solution in the $x - t$ plane. Two unknown states $\mathbf{U}_L^*$ and $\mathbf{U}_R^*$ arise in the shaded areas. (b): piecewise constant initial condition of the problem, defined between the cells $i$ and $i + 1$ .	28
2.6	Structure of the solution of the Riemann problem (2.18). The flux is computed from all the constant $\mathbf{U}$ states originating from the solution of the Riemann problem, and evaluated along the segment $P_0P_4$ .	29
2.7	Structure of the solution of the wet-dry Riemann problem (2.31). The WAF flux at the shoreline is computed from the $\mathbf{U}$ states along the segment $D_0D_2$ .	33
2.8	Example of a generic time history for the values of fluid velocity $v_b$ and water elevation $\eta_b$ . At the time instant $t_j$ correspond prescribed values $v_b^j$ and $\eta_b^j$ to be imposed at the boundary nodes.	40
2.9	Geometrical scheme for the case of an estuary boundary condition entering the domain at an angle $\theta$ . A single boundary condition is read by node $(x_0, y_0)$ at time $t_0$ , and reaches node $(\hat{x}, \hat{y})$ at time $\hat{t} = t_0 + \partial\hat{t}$ .	42
2.10	Scheme for the evaluation of the boundary conditions at each estuary node.	43
2.11	Example of a data cloud serving as a base for the mesh generation. Each blue dot represents a point of the surveyed bathymetry in a cartesian georeferenced system of coordinates.	46
3.1	Plain view of the basin for the preliminary test. The figure shows both the seaward waves (entering from the left side) and the landward waves (entering from the estuary window on the right side). The black dots represent the gauges locations.	52
3.2	Sketches of a shoal bathymetry. <i>Top panel</i> : plan view of the idealized configuration of an inlet mouth with shoal used in the tests by Olabarrieta et al., 2014. The colorbar refers to the depth with respect to the still water level. <i>Bottom panel</i> : 3-dimensional view of the shoal bathymetry used in our simulations.	54
3.3	Samples of the wave series generated through the single peak JONSWAP spectrum (3.3) for the wave-current interaction tests. <i>Top panel</i> : weak wave condition ( $H_s = 0.5$ m, $T_p = 10$ seconds). <i>Bottom panel</i> : strong wave condition ( $H_s = 1.5$ m, $T_p = 10$ seconds).	56
3.4	Sketches of the mesh employed for the morphodynamics tests at the Misa River mouth. <i>Top panel</i> : plan view. <i>Bottom panel</i> : 3-dimensional view.	59

4.1	Time series of water level for gauges 1 ( $x = 0$ m; dotted line), 11 ( $x = 30$ m; red line), and 12 ( $x = 40$ m; blue line), located in the estuary side of the basin. . . . .	62
4.2	Time series of water level for gauges 29 ( $x = 45$ m; light blue line), and 32 ( $x = 50$ m; yellow line), located in the reflective side of the basin. . . . .	63
4.3	Velocity contour fields for wave-current interaction tests with weak outflow ( $u \approx 0.6$ m/s). <i>From top to bottom</i> : T1 (no waves, $H_s = 0$ m); T4 (weak wave regime, $H_s = 0.5$ m); T7 (strong wave regime, $H_s = 1.5$ m). The tests by Olabarrieta et al. (adapted with permission) are shown in the left column; our NSW simulations are shown in the right column. . . . .	65
4.4	Velocity contour fields for wave-current interaction tests with medium outflow ( $u \approx 1.1$ m/s). <i>From top to bottom</i> : T2 (no waves, $H_s = 0$ m); T5 (weak wave regime, $H_s = 0.5$ m); T8 (strong wave regime, $H_s = 1.5$ m). The tests by Olabarrieta et al. (adapted with permission) are shown in the left column; our NSW simulations are shown in the right column. . . . .	66
4.5	Velocity contour fields for wave-current interaction tests with strong outflow ( $u \approx 1.6$ m/s). <i>From top to bottom</i> : T3 (no waves, $H_s = 0$ m); T6 (weak wave regime, $H_s = 0.5$ m); T9 (strong wave regime, $H_s = 1.5$ m). The tests by Olabarrieta et al. (adapted with permission) are shown in the left column; our NSW simulations are shown in the right column. . . . .	67
4.6	Fluid velocity along the main channel central axis as a function of the significant wave height of the opposing waves. <i>Top panel</i> : tests with medium outflow (T2, T5, and T8). <i>Bottom panel</i> : tests with strong outflow (T3, T6, and T9). The tests by Olabarrieta et al. (adapted with permission) are shown in the left column; our NSW simulations are shown in the right column. . . . .	69
4.7	Sediment distribution patterns for two wave-current interaction tests with medium outflow. <i>Top panel</i> : test T5 (weak wave regime). <i>Bottom panel</i> : test T8 (strong wave regime). . . . .	71
4.8	Maps for the Okubo-Weiss parameter in the vorticity tests with $\lambda = 0.001$ at $t = 700$ seconds. . . . .	73
4.9	Temporal evolution of macrovortices for test T8 (medium outflow, strong wave regime) with $\lambda = 0.001$ at simulated times between 500 and 3000 seconds. . . . .	76
4.10	Maps for the Okubo-Weiss parameter for test T8 (medium outflow, strong wave regime) at $t = 1000$ seconds with different values of the LES calibration parameter. . . . .	77

List of Figures

4.11 Time series of the integral Okubo-Weiss parameter for the tests with medium outflow as a function of the calibration parameter  $\lambda$ . *Top panel*: test T5 (weak wave regime,  $H_s = 0.5$  m). *Bottom panel*: test T8 (strong wave regime,  $H_s = 1.5$  m) . . . . . 79

4.12 Time series of the integral Okubo-Weiss parameter for the tests with strong outflow as a function of the calibration parameter  $\lambda$ . *Top panel*: test T6 (weak wave regime,  $H_s = 0.5$  m). *Bottom panel*: test T9 (strong wave regime,  $H_s = 1.5$  m) . . . . . 80

4.13 Qualitative sedimentary patterns around the mouth of the Misa River after about 5.5 hours of simulated time. Blue regions represent deposition, whereas yellow/red areas represent erosion. 82

4.14 Bed variation observed within the main channel and around the mouth of the Misa River during a wintertime period (from September 2013 to January 2014). Zones with colours ranging from light blue to deep blue represent depositional areas; zones with colours ranging from yellow to red are erosive regions. Adapted from Brocchini et al., 2017 . . . . . 83

5.1 Sketch of the bottom boundary layer and the relative velocity log profile . . . . . 86

# List of Tables

3.1 Summary of the wave-current interaction tests. . . . . 57



# Chapter 1

## Introduction

### 1.1 Estuaries

On merely intuitive grounds, we can identify an estuary as the ending part of a river, where a current coming from the hinterland reaches the open sea and establish complicated interactions with a variety of marine processes.

Estuaries provide natural habitats for a great biodiversity in flora and fauna and are excellent hosts for commercial, agricultural, fishing and recreational activities. They are, therefore, areas of great relevance from environmental, social and economic viewpoints and are clearly some of the most complex and dynamic ecosystems in the world. The extreme importance of estuaries in the socio-economic evolution of mankind is exemplified by the fact that 22 of the 32 largest cities in the world are located within estuarine regions [3].

In light of such a great complexity, the study of estuaries requires consideration, knowledge and mutual integration of several disciplines such as physics, hydrology, geography, geology, chemistry, and biology. Nonetheless, a deeper understanding of estuarine ecosystems is essential in order to build a solid framework in which to establish and regulate the multiplicity of activities, events and processes taking place in estuarine areas: urban development, pollution control to the purpose of water quality management, regulations of agriculture and fishery, and establishment of recreational facilities, to name but a few [4].

### 1.2 Classical definitions for estuaries

In the last half century, many definitions of estuaries have been put forward by the community of coastal and maritime specialists [4]. The most historically significant of them, still widely quoted and accepted to some extent, has been proposed by Cameron and Pritchard in 1963 [5, 6]:

*An estuary is a semi-enclosed coastal body of water which has a free connection with the open sea and within which sea water is*

*measurably diluted with fresh water derived from land drainage.*

This definition already addresses some of the key aspects of estuaries, but although rather detailed in its conciseness it presents a few omissions that make it unsuitable to describe the total range of estuarine features detectable in nature. Cameron and Pritchard's statement was in fact suited to describe estuarine features that they were mostly familiar with at the time, but failed to include a crucial characteristic trait, notably the importance of tidal motions [7, 8]. The lack of an explicit mention of tide seems all the more surprising if we consider that, etymologically, the word *estuary* itself derives from the Latin word *aestus*, which means *tide* [9]. Indeed, the tide is the main agent that provides the energy input responsible for water mixing in the majority of estuaries. Tides play an important role in erosion processes and in the movement and deposition of the large amount of sediment contributed by rivers and stirred up by waves in the most shallow reaches of the estuary [4], exerting a strong influence even further landward of the limit of saltwater intrusion [10, 11]. In an attempt to fill the conceptual gaps and limitations of Cameron and Pritchard's definition, Fairbridge itself provided a more comprehensive definition of estuary including an explicit reference to the essential tidal influence [7]:

*An estuary is an inlet of the sea reaching into a river valley as far as the upper limit of tidal rise, usually being divisible into three sectors: (a) a marine or lower estuary, in free connection with the open sea; (b) a middle estuary subject to strong salt and fresh water mixing; and (c) an upper or fluvial estuary, characterized by fresh water but subject to daily tidal action.*

However, both the simple definition by Cameron and Pritchard and the more comprehensive definition by Fairbridge still rule out other coastal water bodies with periodically variable topological features, such as coastal lagoons, as well as estuarine basins in arid and tropical areas, where the balance between freshwater from land and marine water is strongly skewed due to seasonal regimes and extreme climate.

In more recent times, Dalrymple et al. introduced a geologically-oriented definition developed as the base for the construction of an estuarine facies model [12]:

*[An estuary is] the seaward portion of a drowned valley system that receives sediment from both fluvial and marine sources, and contains facies influenced by tide, wave and fluvial processes. The estuary is considered to extend from the inner limit of tidal facies at its head to the outer limit of coastal facies at its mouth.*

In formulating their definition, the authors recognized that the near totality of present day estuaries are originated in river valleys that have been flooded after the global sea rise to near its present level as a consequence of the last ice age (ended around 12 000 years ago). Besides this purely geological fact, estuaries can also be envisaged as efficient sediment traps for both terrestrial and marine sediments [13]: nonetheless the general transgressive nature of estuaries, in opposition to deltas which are typically prograding systems, suggests that the global net balance of sediments received by estuarine valleys is oriented landward. Dalrymple's definition, at last, explicitly acknowledges the morphogenic power of the three most relevant energy sources for estuarine environments: rivers, waves, and tides. The relative importance of riverine, wave and tidal processes is, indeed, the foundation concept for some of the most comprehensive methods to date for the classification of estuarine and coastal structures; such schemes of both historical and practical interest will be examined in the following section.

## 1.3 Classification of estuaries

In line with the everlasting search of the "perfect" definition for estuaries, the last decades have seen the birth, development and refinement of several classification methods for estuaries [14, 15, 16]. However, as estuaries all over the world exhibit a striking diversity of size, shape, origin, hydrology, geomorphology and evolutionary patterns, designing a classification method encompassing all the global variables into a coherent subdivision is a prohibitive, if not impossible task. Moreover, fitting a given estuarine or coastal basin into any defined classification is an operation that must be undertaken with extreme caution, since the very same estuary or coastal embayment may show radically different characteristics according to the season, the tidal phase or even the atmospheric conditions. In spite of these deterrents, though, a few traditional approaches gained and preserved a certain popularity over the years, thanks to their capability of giving a sound description of a great number of estuaries around the world through evaluation of their most common characteristics: this section is devoted to a brief overview of such classifications.

### 1.3.1 Classification based on tidal range

One of the first attempts to develop a coastal classification scheme is attributed to Davies, who subdivided coastline features and structures on the basis of the tidal range intensity [17]. According to this seminal classification, microtidal coasts and environments are characterized by a typical tidal range of less than 2

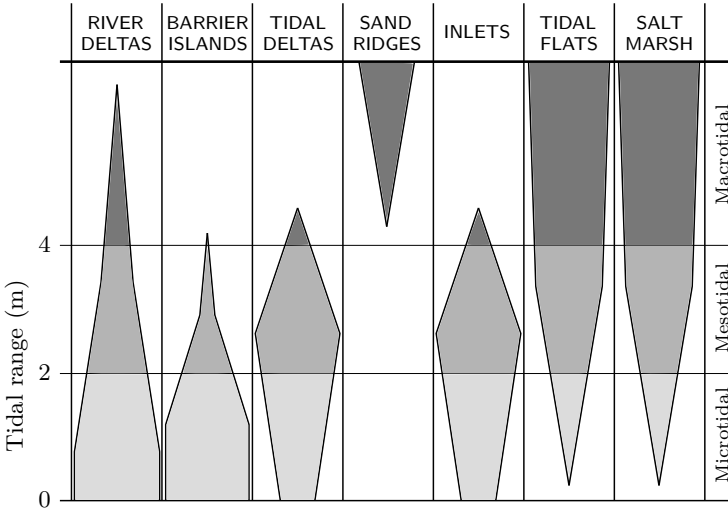


Figure 1.1: Variation of coastal and estuarine morphological features with respect to the extension of tidal range, in medium wave condition. Adapted from Hayes, 1975

meters; mesotidal coasts feature tidal ranges between 2 and 4 meters; macrotidal coasts, finally, present a tidal range greater than 4 meters. Hayes, in his analysis of the morphology of sand deposits associated with estuaries, further expanded and complemented the work of Davies by recognizing the different characteristics of barrier islands and other estuarine deposits according to the tidal excursion. Hayes furthermore noted that an increase in tidal range is accompanied by a general reduction of wave action and an intensification of tide-related currents [18, 19]. Hayes proposed a classification of estuaries based on tidal range as follows:

- microtidal estuaries* (tidal range lower than 2 meters), which are dominated by the action of both riverine discharge from land and wind waves coming from the open sea. The effect of tidal excursion and the associated currents is felt mainly at the most seaward reaches of the estuary, and within barrier inlets if present. Microtidal estuaries can evolve into deltas, if the sediment contribution supplied by the river is strong enough. The main forms of sediment deposition are long and continuous barrier islands, seldomly interrupted by inlets. Associated with the periodic movement of flood and ebb phase tides through inlets are the so-called tidal deltas, i.e. flood-tide and ebb-tide deltas [20]. The reduced influence of tide also favours the development of wave-generated features like bars and coastal berms. In the family of microtidal estuaries we find one of the best studied estuaries in literature: the Chesapeake Bay, in

the United States [21, 22, 23, 24].

- *mesotidal estuaries* (tidal range between 2 and 4 meters) in which the increased tide range is comparable with the marine and riverine forces in the definition and evolution of estuarine features. Coastal barrier systems are still present, but not as extensively as for microtidal estuaries; in turn, there is an increase in the number and width of tidal inlets and affiliated sedimentary units [25]. The moderate action of tidal currents promotes the growth of wide, tide-dominated regions like salt marshes [26] and, to a lesser extent, tidal flats [27].
- *macrotidal estuaries* (tidal range greater than 4 meters), where the action of tides is strongly dominant over the other agents, and roughly comparable to the mean estuary depth. Peculiar of macrotidal coasts and estuaries are the relative absence of barrier islands and tidal inlets and the presence of systems of salt marshes and extensive tidal flats. The main sedimentary structures are limited to linear sand ridges developing in the more offshore reaches of the estuary, orientated in the dominant direction of flood and ebb flows and often organized into ridge fields.

A schematic representing the variation of coastal features as a function of the tidal range is presented in Figure 1.1.

### 1.3.2 Classification based on salinity

Although of limited practical use whenever estuaries are studied in a morphological sense, another common classification for estuarine environments is based on the salinity gradient [3, 5, 28]. The distribution of salt concentration in the water body of an estuary is strictly connected with the way layers of sea water and fresh water are formed and distributed into more or less distinguishable vertical stratification patterns. According to this criterion estuaries can be subdivided into salt-wedge, strongly stratified, weakly stratified, and well-mixed estuaries (see Figure 1.2):

- *Salt-wedge estuaries* [29] occur when the freshwater outflow is strong enough to win the mixing action promoted by waves and tide and maintains a sharp separating interface between the water bodies at different salinity. Since freshwater is less dense than salt water, the river discharge does not mix with sea water, but expands as an homogeneous layer above an underflowing saline wedge [30]. The resulting salinity configuration exhibits a sharp and thin halocline layer, i.e. the layer in which the salinity gradient is greatest. In salt-wedge estuaries the tide action is so weak that the stratification of freshwater over sea water is often conserved

throughout a whole tidal cycle. Salt-wedge estuaries are typical of rivers with considerable flows discharging in seas with little to no tidal motion: examples are the Rhône, the Ebro, and the Mississippi.

- When the strength of tidal forcing increases, but is not yet comparable with the intensity of river outflow, the estuarine circulation produces a *strongly stratified estuary*, characterized by a stratification similar to salt-wedge estuaries, albeit not as sharp. Here, the tidal excursion succeeds in promoting a partial mixing between salt and fresh water and produces a slightly milder salinity gradient than those in a salt-wedge estuary.
- *Weakly stratified estuaries* are a consequence of a moderate-to-strong tidal forcing coupled with a weak-to-moderate riverine discharge. Due to the comparable strength of both river and marine agents the mean exchange flows are more intense with respect to the previous type of estuaries, and result in a weak gradient of the salt content within the tide-influenced range of the estuary, a reduced vertical stratification of fresh and salt water and a more vigorous mixing. Weakly stratified estuaries are frequent in temperate climate zones.
- *Well-mixed estuaries*, or vertically mixed estuaries, are estuaries in which the tidal range and associated tidal currents are energetic enough to efficiently mix salt and fresh water layers into the water column. No water stratification is identifiable and the isohalines are vertical or subvertical with respect to the river bottom; in other words, the salinity of water in a well-mixed estuary is the same from the water surface to the bottom of the estuary, with the salinity growing uniformly seaward of the maximum limit of salt intrusion. Very shallow estuaries like the Delaware Bay are typical examples.

### 1.3.3 Classification based on dominant processes

The definition of estuaries devised by Dalrymple and colleagues [12] is grounded on the realistic observation that any estuarine environment is a zone of complicated combination of numerous energy sources: among these the most relevant for the study in coastal engineering are tides and related currents, waves, and riverine discharges.

The deep influence of the first two of the abovementioned forcings is acknowledged by Zaitlin and Shultz [31] who proposed a conceptual distinction of estuarine complexes into wave-dominated and tide-dominated in the context of a case study to relate the physical and morphological characteristics of estuaries to the behavior of petroleum-producing reservoir basins. According to

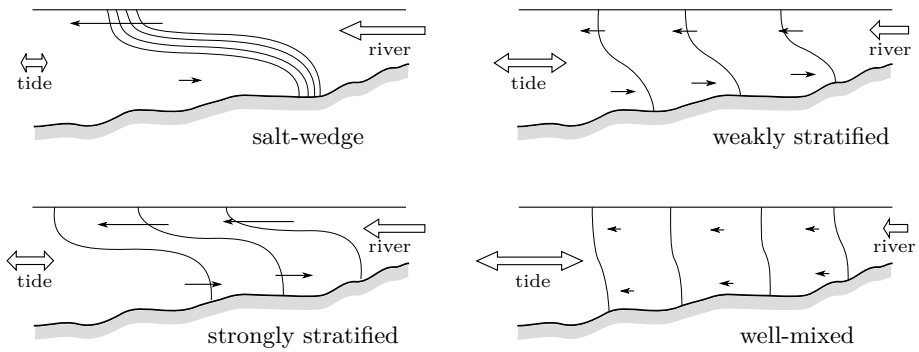


Figure 1.2: Classification of estuaries based on salinity gradient and consequent water stratification. The black lines are isohalines, i.e. lines connecting points with the same salinity. Adapted from Valle-Levinson, 2010

the relative importance of waves and tides estuarine features will span into a wide spectrum, at the extremes of which two simple conceptual end-member models can be identified:

- as their denomination suggests, *wave-dominated estuaries* [32, 33, 34] are strongly dominated by the action of waves entering the estuary from the open sea. They develop features normally determined by wave-driven sedimentary processes, like barrier islands spaced out by inlets in front of the mouth. Eventual intervention of tide keeps the inlets open and generates flood tidal deltas. In the central portion of the basin, generally a region of low global energy, the prevalent process is the deposition and local resuspension of fine material transported by both river currents and local waves. At the more landward region of the estuary, where the river forcing is dominant over both tide and wave action and the sediment-remodeling capabilities of the tide-induced circulation is limited, the riverine material often settle and redistribute into rudimental deltas. The features of wave-dominated estuaries and their spatial distribution generally are in correspondence with microtidal and lagunary coasts as defined by the classification by Davies [17, 35] and Hayes [18, 19]. An idealized wave-dominated estuary is sketched in Figure 1.3 along with an indicative distribution of energy types within the estuary basin;
- at the opposite side of the spectrum of estuarine types, *tide-dominated estuaries* [36] are mainly determined by the action of tides over waves. For a coastline to be tide-dominated, however, it is not necessary for the tide to be exceptionally strong or large: tide dominance may well occur in coastlines with moderate-to-low-ranging tides too, as long as the concur-

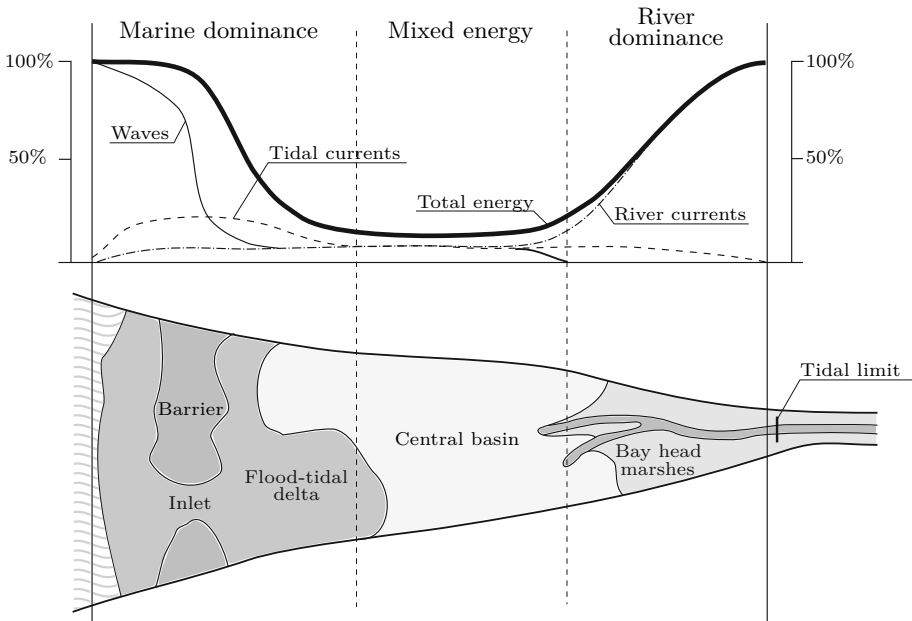


Figure 1.3: Distribution of energy types and main morphological features in a simplified wave-dominated estuary. Adapted from Dalrymple et al., 1992

ring wave action doesn't outrange tidal influence [19]. As an extreme case, a complete lack of waves is enough to generate a tide-dominated coastline even with limited tidal range. In the inner parts of the basin the influence exerted by tides is frequently stronger than riverine discharge and is successful in redistributing the finest, cohesive sediments into wide mudflats, sand marshes and/or tidal flats. At the basin mouth, where the tide importance is almost total (albeit a bit of wave action cannot be ruled out), typical longitudinal sandy features called tidal sand bars, or sand ridges [37, 38] can be found rather offshore, up to the continental shelf area, as a result of ebb-tidal flows. Tide-dominated estuaries are common in coasts classified as macrotidal according to Hayes [18, 19]. A sketch of an idealized tide-dominated estuary environment is shown in Figure 1.4.

Albeit rather comprehensive, the study by Zaitlin and Shultz presents a shortcoming as it assumes that estuarine features are defined mainly by the mutual interplay between marine forces only, and thus the effect of riverine discharge on the determination of estuarine facies is neglected. Indeed, rivers are crucial in shaping the temporal geomorphological evolution of estuarine systems, since they feed the estuarine basin with large amounts of land-originated

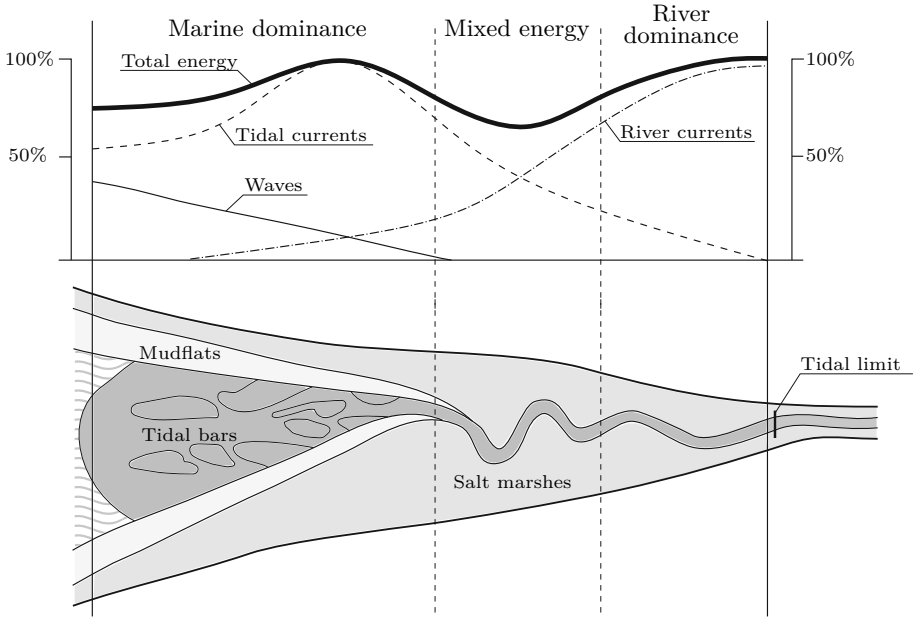


Figure 1.4: Distribution of energy types and main morphological features in a simplified tide-dominated estuary. Adapted from Dalrymple et al., 1992

sediment that, on the basis of years, decades or centuries, are deposited and stratified inside the basin in a large number of ways, according to the dominant energy and circulation patterns. Besides, the speed and flow rate of the river currents carrying such sediment cannot be left unconsidered, since they directly intervene in defining the extension of the outflow and the subsequent range of sediment deposition, and often resulting in characteristic sandy features like radial bars [20, 39].

Dalrymple et al. [12, 40] expanded on the arguments proposed by Zaitlin and Shultz by implementing their criteria into a wider, evolutionary-based classification. Their intent was to introduce also the important river processes in the method, so as to include into a single scheme the full spectrum of major depositional structures — deltas, strand plains, tidal flats, estuaries and lagoons — and enhance the standard (process-based) classification with temporal aspects. This is to give a conceptual explanation for the temporal evolution of coastal systems: an example of such a concept is the gradual infilling of estuary basins, especially the least energetic ones, which may eventually close or evolve into other types of coastal structures.

At the base of the evolutionary scheme is a trivariate process-based classification which builds upon the previous consideration by Zaitlin and Shultz [31]

by complementing the binary wave/tide criterion with the third, river-based contribution. The same tripartite framework has been employed in earlier times by Galloway [41] for deltas and Johnson and Baldwin [42] for continental shelves.

The ternary diagram illustrating the relationship of the three main genetic processes is presented in Figure 1.5. The horizontal axis of the diagram, at the base of the triangle, represents the relative influence of waves versus tides, as in the scheme by Zaitlin and Shultz [31]; the vertical axis indicates the intensity of fluvial influence, increasing from the bottom to the top of the triangle. It is immediately seen that the wave/tide-dominance classification of estuaries devised by Zaitlin and Shultz finds a place in the central trapezoid of the genetic triangle by Dalrymple et al., characterized by embayed coastlines with mixed wave-tide-river influence. The lowest part of the triangle is dedicated to coastal features originating from marine sediment contribution where the influence of the river discharge extremely low or null: these features are strandplains (or beach ridge plains) if the main genetic process is related to waves, or tidal flats if the dominant process is tide-based. The uppermost part of the triangle is occupied by deltaic structures, characterized by a prograding (not embayed) coastline of elongate or lobate shape nurtured by an intense fluvial income and an abundant sediment contribution. In this scheme lagoons lie at the borderline between estuaries, strandplains and tidal flats and can be interpreted as estuary-like environments where fluvial influence is negligible and the sediment input almost completely comes from wave action in microtidal-to-mesotidal coasts.

The introduction of evolutionary concepts into the scheme by Dalrymple et al. [12] is performed by adding a third "dimension" related to relative time to the process-based triangle in Figure 1.5. The result is the prism in Figure 1.6. Following the temporal evolution of coastal environments, an estuary may in time evolve into a prograding structure such as a delta thanks to possible basin infilling spanning years or decades: this prograding process is represented by a movement towards the back of the prism in Figure 1.6. Conversely, a well established delta may be flooded, remodeled or "pushed back" because of increments of wave action or sea level; such transgression-generating events lead to a movement towards the front face in the prismatic shape in Figure 1.6.

The full range of coastal sedimentary complexes included in the aforementioned classification is presented in Figure 1.7. The picture is arranged so that the relative dominance of waves over tide increases towards the right side of the figure, whereas the importance of tidal force over waves increases towards the left side. The upper part of the picture features transgressive scenarios, i.e. estuarine and coastal structures that hosts more or less pronounced embayments of the coastline: the most relevant of these are estuaries and lagoons. The lower

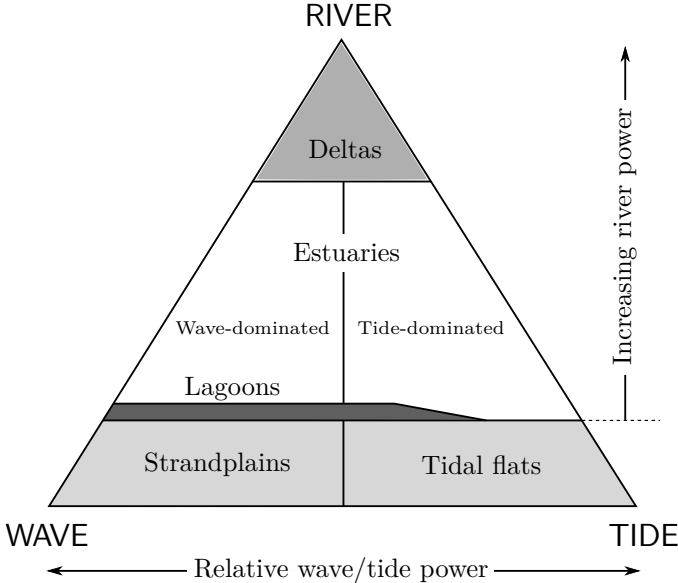


Figure 1.5: Tripartite classification scheme of coastal facies based on the relative importance of river, wave, and tide action. Adapted from Boyd et al., 1992

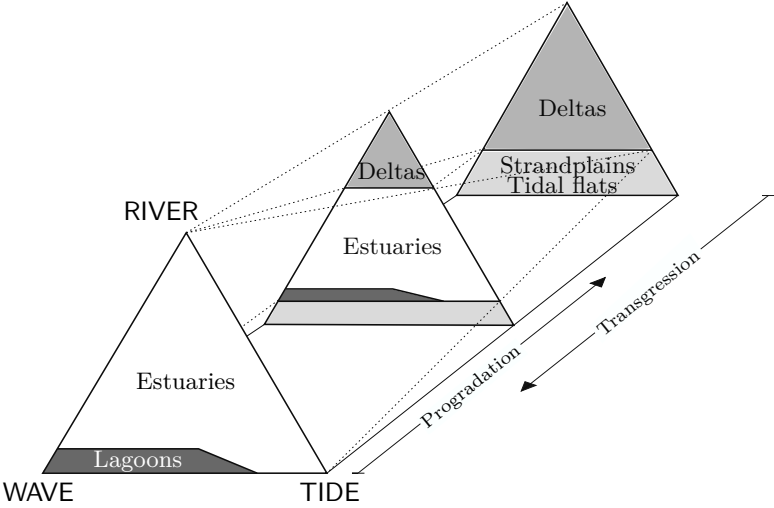


Figure 1.6: An example of evolutionary process of estuarine environments. The gradual progradation of coasts corresponds to a movement towards the back of the prism; a transgressive behavior is represented by a movement towards the front of the prism. Adapted from Boyd et al., 1992

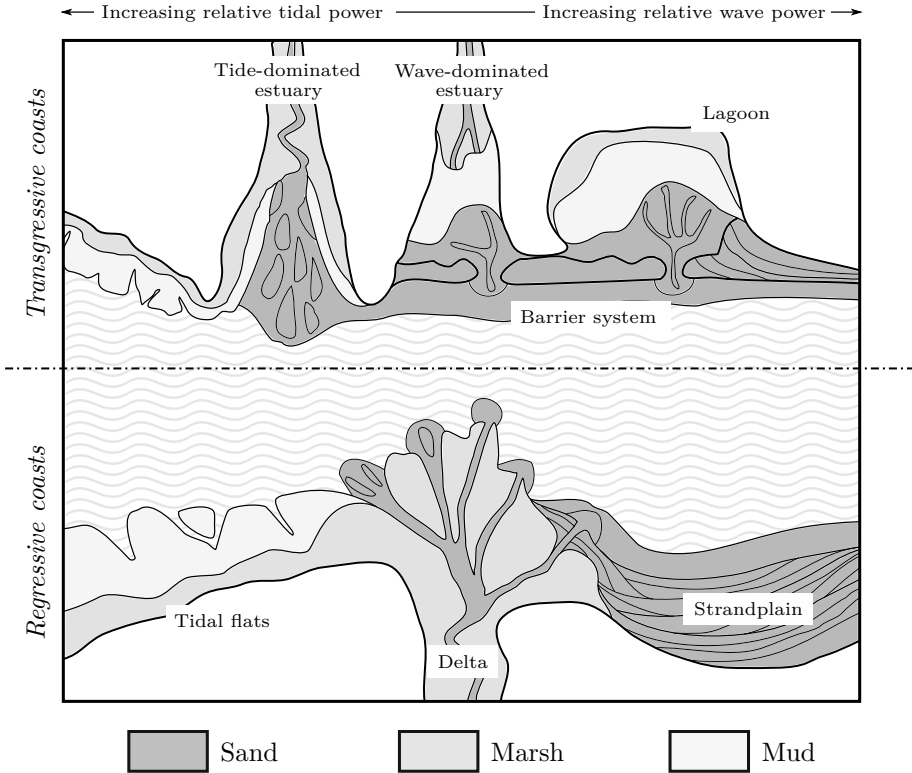


Figure 1.7: Range of main shallow-water coastal depositional features, arranged as a function of tidal and wave power. Adapted from Boyd et al., 1992

side of the picture, on the other hand, presents regressive coast complexes, in which the coastline grows towards the open sea: most notably, deltas (where the fluvial input is the most intense), tidal flat and strandplains (where fluvial influence is null or negligible).

## 1.4 The influence of waves on estuary mouths and inlets

In the light of the classifications and the abundant studies undertaken by the scientific community in the last decades, gravity waves and wave-related events and processes are clearly entitled to be considered an important agent in shaping and modifying coasts and related structures [32].

In recent times, attention has been dedicated specifically to the influence of waves in estuary mouths and tidal inlets. It is long clear, in fact, that the

approaching and transforming waves have a strong effect over the intensity, direction, extension and stability of river outflows and ebb currents [2, 43]. Moreover, waves breaking on ebb-tide shoals and other sand-made deposits typical of estuarine or deltaic regions will likely induce wave setup and cause an increase of the mean water level in enclosed basins to the likes of back-barrier lagoons and estuaries [43, 44].

With reference to a wave-dominated tidal inlet, where the ebb and flood currents generated by tidal motions are bound to interact with the incident wave regime, Dodet et al. [44] pointed out that the characteristics of broken waves in the vicinity and within the inlet mouth are different according to the concurrent tidal phase. During the ebb flow, the offshore-directed tidal currents increased the wave height at the inlet mouth, but decreased the wave height within the mouth. The opposite happens during a flood flow with onshore-directed currents, although with minor intensity. The overall stronger opposition of waves during the ebb flow has an effect in limiting the seaward extent of sediment fluxes and promotes the deposition of sediment in the interior of the inlet mouth and shoreward of it.

Waves also have a crucial impact on the global morphodynamics of inlets and embayed coasts. In coastal contexts where wave action is prominent and fluvial or tidal outflow rates are high, the strong current favours the blocking of waves and longshore currents, induces a strong overall energy dissipation and enhances the deposition of suspended sediment [44, 45]. This results in sand accumulations at the mouths, which often take the shape of bars and tidal deltas. In the absence of waves, the distance between the area of formation of the aforementioned sandy features and the inlet mouth is directly proportional to the jet momentum flux, and inversely proportional to the suspended sediment size [46]: the presence of a wave regime may effectively alter the exact location of this area or suppress it, according to different parameters like the wave height, the angle of incidence, and the wave period. As an example, large and long waves are more likely to suppress mouth-related sand formations, because of jet instabilization and the deviation of the outflowing jet promoted by oblique waves. Numerical analysis of a river jet subjected to frontal waves revealed that the incoming gravity waves increased the spreading of the river jet, and in the presence of waves, mouth bars form up to 35% closer to the river mouth and 40% faster when compared to the same situation when waves are absent. Moreover, the distance between the river mouth and the bar decreased with increasing wave height and wave period [47, 48].

The redistribution of sediment around an inlet mouth or estuary to the adjacent coasts is determined, in large part, by the constant action of wave-generated longshore currents. The intensity and patterns of this redistribution vary with the strength of the opposing river jet, the energy of incoming gravity

waves and the angle of wave incidence. In general, when waves approach the coast obliquely, the induced longshore currents may promote the progradation of skewed river mouths and, eventually, define the building of asymmetrical coastal structures over the time of several decades [49].

## 1.5 Numerical modeling of estuaries

Estuarine and in general coastal environments are zone of appalling complexity. An extremely wide range of different processes and variables are at play in an estuary: waves and wave-related currents, tide, river inputs, salinity, density, temperature, flora and fauna, nature of sediments, bottom friction, existing morphology, man-made intervention. Since such a complex situation cannot be fully understood and thoroughly analyzed only by means of experimental campaigns and real-case observations, use of technology as a tool to simulate and investigate the intricate nature of estuaries to the purpose of hydrodynamics and water-quality assessment is highly desirable [50].

Thanks to the great progresses achieved in the last sixty years in the fields of computational sciences and theory of numerical methods for hydraulics engineering, use of numerical models to achieve a correct representation of waves, currents and sediment transport mechanisms in coastal seas has seen a considerable increment. The best description of coastal evolution induced by the hydrodynamics in the nearshore has been pursued with increasing dedication over the last three decades: correspondently, several studies have been dedicated to analyze the capabilities of numerical models in reproducing flows and sediment dynamics in coasts and estuaries. As examples, numerical models have been applied to describe global nearshore hydrodynamics [51, 52, 53], tidal processes [54, 55, 56], and wave-current interactions in a broad range of tidal inlets ([2, 43, 57, 58, 59] among others).

In the present work focus will be given to wave-dominated inlets, to which shallow estuaries with a considerable wave influence may be assimilated. The main processes concerning the hydrological and morphologic evolution of such environments will be reproduced and investigated by means of a modified version of the finite volume-based numerical solver designed by Brocchini et al. [1]. Originally intended to recreate only problems of wave propagation in shallow waters without other external flow sources, the solver has been modified for the purpose of this investigation, in order to give proper account of the dynamics induced by a river discharging at sea. The modified solver will be then employed to carry out a series of numerical simulations, divided into two sets. The first set of tests will inspect the interaction between waves and river currents in the context of a simplified inlet; these tests have been inspired by a previous work on the same matter by Olabarrieta et al. [2]. The second set

of tests has been conceived to help shed some light over the morphodynamics of a real-case scenario: the Misa river estuary in Senigallia, Italy.

The thesis will be organized as follows. Chapter 2 presents a description of the hydro-morphodynamic numerical model for shallow waters developed by Brocchini et al [1], as well as the additions and improvements implemented to make it suitable to describe the flow circulation in simplified estuarine environments. Chapter 3 describes the numerical benchmarks used to validate the performance of the novel estuarine model: the results of these tests are presented and discussed in Chapter 4. In Chapter 5 a new approach for a bottom boundary layer model for 2-dimensional shallow water solvers with structured meshes is proposed; such a model is still in development and thus it has not been used for the simulations described in this thesis. Concluding remarks are finally presented in Chapter 6.



# Chapter 2

## The hydro-morphodynamic numerical model

### 2.1 The nonlinear shallow water equations

The nonlinear shallow water equations (NSWEs) are a set of hyperbolic partial differential equations describing the conservation of mass and momentum in fluid motion. They can be derived as an approximation of the Navier-Stokes equations for viscous fluids.

The 2-dimensional horizontal (2DH) version of the NSWEs, employed in the present thesis, is achieved by integrating the flow quantities over the height of the water column. This approximation is based on the assumption that the horizontal scale of the phenomenon under investigation (i.e. the characteristic wavelength in case of wave propagation) is much greater than the vertical scale (i.e. the water depth), so that the motion is assumed to take place in *shallow waters*. If this is the case, the effect of the vertical fluid acceleration on the pressure is considered to be negligible, which is the same as saying that the hydraulic pressure is hydrostatic. Extensive details on how NSWEs are derived can be found in the comprehensive books by Stoker [60] and Whitham [61].

In their primitive form, NSWEs neglect the effect of frictional forces developing at the interface between the bottom and the water body: for a more complete treatment of fluid flow problems, however, the standard NSWEs should be complemented with friction, whose action is all the more important in dealing with shallow water motions, since the effect of friction is stronger as the water depth decreases. Friction forces (like viscous contributions, wind forces and Coriolis forces, to name but a few) serve as an additional source term: therefore, they make the governing equation non-homogeneous and their accounting should be treated accordingly. Unfortunately, inclusion of source terms in a numerical solution procedure still poses several theoretical and analytical problems. An exhaustive treatise on numerical techniques for systems of PDEs with source terms can be found in the book by Toro [62]. Several works [63, 64, 65, 66] dealt with the treatment of source terms in the frame-

work of the NSWEs with encouraging results.

Regarding bottom friction specifically, Longuet-Higgins [67] long recognized its role in dissipating the energy of incoming waves (albeit its influence is not as relevant as wave breaking) and correlated friction forces with the generation of longshore currents. By implementing frictional effects through a simplified Chezy-like formulation, Watson et al [68] showed that including friction in the analysis of swash zone motions, even though in an approximate way, is important especially when beachface slopes are gentle.

## 2.2 The Exner equation

The Exner equation [69, 70, 71] is a sediment mass conservation equation that relates the local rate of change of the bed elevation with the spatial variation of the sediment fluxes entrained by fluid motion. Therefore it can aptly describe the overall evolution of a movable bed under fluid flows. The solver adopted in the present thesis complements the standard hydrodynamics equations with the Exner equation in order to attain a simple, yet rather reliable description of fluid and sediment dynamics in the nearshore.

Following Fredsøe [72, 73] sediment transport mechanisms can be roughly divided into two main modes: *bed load*, i.e. the part of the total load which is in more or less continuous contact with the bed and moves through rolling, sliding or jumping, and *sediment load*, i.e. the part of the total load that is put into suspension within the water column and is moved through advection. Nearshore morphodynamics models usually represent sediment transport as the sum of the two aforementioned contributions, whose numerical definition is often a delicate task. This difficulty is in no small part due to the wide range of closure formulae that has been conceived over the last decades [74, 75, 76, 77, 78, 79]: one has to carefully evaluate which relations are most suitable to be implemented according to the intended applications.

## 2.3 The complete system

The NSWEs-Exner equations system of conservation laws is presented here in *non-conservative* form:

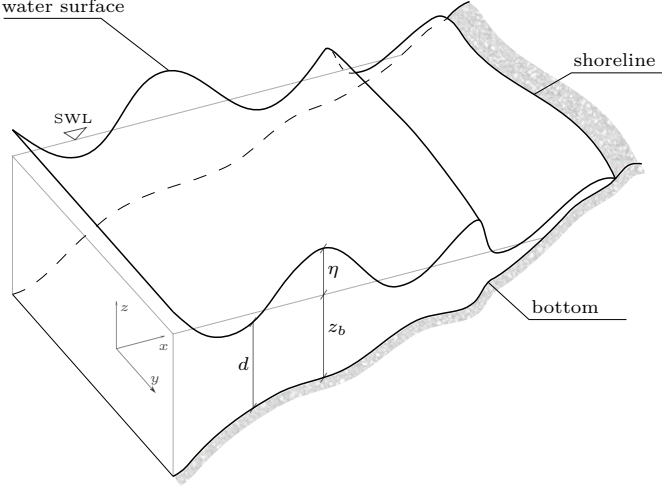


Figure 2.1: Schematic of the nearshore.

$$d_{,t} + (ud)_{,x} + (vd)_{,y} = 0, \quad (2.1a)$$

$$u_{,t} + uu_{,x} + vv_{,y} + gd_{,x} = -gz_{b,x} - B_x, \quad (2.1b)$$

$$v_{,t} + uv_{,x} + vv_{,y} + gd_{,y} = -gz_{b,y} - B_y, \quad (2.1c)$$

$$z_{b,t} + \frac{1}{\lambda} \nabla \cdot \mathbf{q} = 0, \quad (2.1d)$$

where (2.1a-c) are the 2DH nonlinear shallow water equations for the hydrodynamics, and (2.1d) is the 2-dimensional Exner equation for the morphodynamics.  $(x, y, z)$  is an orthogonal Cartesian system of spatial coordinates and  $t$  represents time. Subscripts after the commas represent partial differentiation with respect to space or time. The datum for the vertical coordinate  $z$  is located at the still water level  $z = 0$ .

The flow variables are the vector of depth-averaged horizontal velocities  $\mathbf{v} = (u, v)$  and the water depth  $d = \eta - z_b$ , where  $\eta$  is the elevation of the water surface and  $z_b$  is the bottom depth, both measured with respect to the still water level.  $\lambda$  is the grain packing of the beach sediment, which is defined as  $1 - p$ ,  $p$  being the beach porosity;  $\mathbf{q} = (q_x, q_y)$  is the vector of sediment fluxes;  $g$  is the acceleration of gravity.

$B_x$  and  $B_y$  represent the external contributions to the fluid momentum balance due to the seabed friction. In the present solver a Chezy-type formulation, known for providing convincing results in spite of its simplicity and semi-empirical nature, is assumed for modelling bed shear stresses. Following this assumption, the source terms for bed friction are correlated to fluid velocity

and water depth as follows:

$$B_x = \frac{\tau_x}{\rho} = c_\tau \frac{|\mathbf{v}|u}{d} \quad \text{and} \quad B_y = \frac{\tau_y}{\rho} = c_\tau \frac{|\mathbf{v}|v}{d}, \quad (2.2)$$

where  $c_\tau$  is a dimensionless Chezy friction coefficient, usually of order  $10^{-2} - 10^{-3}$  [1].

It is tempting to directly build and use numerical solution schemes for the non-conservative NSW system (2.1a-c). It has been proven, however, that adopting finite difference schemes for non-conservative forms of conservation laws introduces systematic numerical errors that generically grow in time [80]; therefore, non-conservative schemes do not converge on the proper solution and *conservative* formulations must be adopted instead. Moreover, conservative formulations heavily depends on the definition of the underlying *conserved variables*. Different choices of the conserved variables lead to different conservative formulations, not all of which make physical sense: hence particular care must be taken in deriving a conservative formulation that is consistent with the physics of the phenomenon under investigation. Furthermore, NSWs are intended to describe fluid motion in shallow waters, where bores are expected to propagate. In a numerical framework, bores and shock waves are represented as abrupt discontinuities of the solution; a conservative scheme that is able to properly treat such discontinuities is therefore highly desirable. For further details and examples about conservative and non-conservative forms for conservation laws the reader is referred to Chapter 3.3 in [62].

In the light of all the aforementioned requirements, the conservative form of the NSW system (2.1a-c) which is the most suitable for our purposes reads:

$$d_{,t} + (ud)_{,x} + (vd)_{,y} = 0, \quad (2.3a)$$

$$(ud)_{,t} + \left( u^2d + \frac{1}{2}gd^2 \right)_{,x} + (uvd)_{,y} = -gdz_{b,x} - c_\tau |\mathbf{v}|u, \quad (2.3b)$$

$$(vd)_{,t} + (uvd)_{,x} + \left( v^2d + \frac{1}{2}gd^2 \right)_{,y} = -gdz_{b,y} - c_\tau |\mathbf{v}|v, \quad (2.3c)$$

or, in vectorial form,

$$\mathbf{U}_{,t} + \mathbf{F}(\mathbf{U})_{,x} + \mathbf{G}(\mathbf{U})_{,y} = \mathbf{S}(\mathbf{U}) \quad (2.4)$$

where  $\mathbf{U}$  is the vector of conserved variables (its components representing the conserved quantities in the equations of mass,  $x$ -momentum and  $y$ -momentum respectively),  $\mathbf{F}(\mathbf{U})$  and  $\mathbf{G}(\mathbf{U})$  are the vectors of fluxes and  $\mathbf{S}(\mathbf{U})$  is the vector

of source terms:

$$\mathbf{U} = \begin{vmatrix} d \\ ud \\ vd \end{vmatrix} = \begin{vmatrix} U_1 \\ U_2 \\ U_3 \end{vmatrix}, \quad (2.5)$$

$$\mathbf{F}(\mathbf{U}) = \begin{vmatrix} ud \\ u^2d + \frac{1}{2}gd^2 \\ uvd \end{vmatrix} = \begin{vmatrix} U_2 \\ \frac{U_2^2}{U_1} + \frac{1}{2}gU_1^2 \\ \frac{U_2U_3}{U_1} \end{vmatrix} \quad (2.6)$$

$$\mathbf{G}(\mathbf{U}) = \begin{vmatrix} vd \\ uvd \\ v^2d + \frac{1}{2}gd^2 \end{vmatrix} = \begin{vmatrix} U_3 \\ \frac{U_2U_3}{U_1} \\ \frac{U_3^2}{U_1} + \frac{1}{2}gU_1^2 \end{vmatrix} \quad (2.7)$$

$$\mathbf{S}(\mathbf{U}) = \begin{vmatrix} 0 \\ -gdz_{b,x} - c_\tau |\mathbf{v}|u \\ -gdz_{b,y} - c_\tau |\mathbf{v}|v \end{vmatrix}. \quad (2.8)$$

A complete solution of both hydrodynamic and morphodynamic features from the *fully coupled* complete system (2.1) by means of a single numerical scheme is not an easy task in most cases, due to the complex structure of the corresponding eigenvalue problems and the relative difficulty in evaluating eigenvalues and eigenvectors [81, 82, 83]: furthermore, such numerical approaches often require significantly large computational time.

The solver used in the present study, based on the work by Brocchini et al [1] and further complemented by Postacchini [79, 84], on the contrary, is *weakly coupled*. From an operative point of view, a weakly coupled solver resolves the hydrodynamic (2.1a-c) and morphodynamic (2.1d) equations separately (as a totally uncoupled model does) and consecutively: then, at the end of each time step the bed evolution obtained from the resolution of the morphodynamic part (the Exner equation) is enforced at the hydrodynamic module, altering its solution for the subsequent step. In any resolution of the hydrodynamic system only the flow variables  $u, v$  and  $d$  are updated, while the bed depth  $z_b$  remains constant; the morphodynamic scheme is then applied to resolve the Exner equation and advance  $z_b$ , the flow variables staying univariate at this time. As a result, the initial state of variables  $W^n = (d^n, u^n, v^n, z_b^n)$  at time  $n$  is advanced through the time step to the solution  $W^{n+1} = (d^{n+1}, u^{n+1}, v^{n+1}, z_b^{n+1})$  at time  $n + 1$ . A flow chart of the integration procedure through a single time step is illustrated in Figure 2.2.

## 2.4 The numerical solver

Once the complete system is posed in the appropriate conservative form, the NSWE system for the hydrodynamics (2.4) is solved numerically by means of the WAF method described by Toro [62, 85, 86], whereas the Exner equation for the morphodynamic evolution of the bed (2.1d) is solved separately through a similar finite-volume approach. The solving schemes for NSWE and Exner equations will be labeled  $H$  and  $M$ , and will be briefly described in sections 2.4.1 and 2.4.2 respectively. A flow chart of the numerical integration is shown in Figure 2.2.

### 2.4.1 The hydrodynamic module

The hydrodynamic solver ( $H$ ), described in detail in [1], is employed for the resolution of the 2-dimensional NSWE system (2.4) and the advancing of flow variables  $u$ ,  $v$  and  $d$  through a single time step  $\Delta t$  (note that, throughout the hydrodynamic step, the bed elevation  $z_b$  is kept constant). The solver

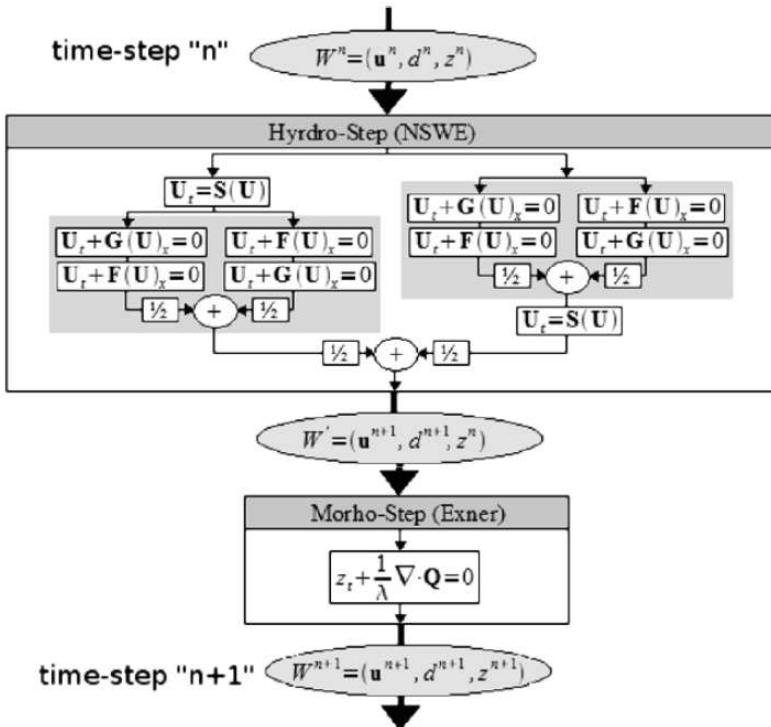


Figure 2.2: Flow chart of the numerical integration procedure.

is founded on the weighted averaged flux (WAF) method, a discrete finite-volume numerical approach for conservation laws which is particularly effective in treating discontinuous solutions, such as wave propagation in shallow waters.

The difficulty of dealing with a 2-dimensional non-homogeneous problem is removed by operating a dimensional and operational splitting [62]: the initial NSWE system (2.4) is split into two homogeneous systems (so that 1-dimensional methods can be applied in each spatial direction) and one "source" system:

$$\mathbf{U}_{,t} + \mathbf{F}(\mathbf{U})_{,x} = 0 \quad (2.9)$$

$$\mathbf{U}_{,t} + \mathbf{G}(\mathbf{U})_{,y} = 0 \quad (2.10)$$

$$\mathbf{U}_{,t} = \mathbf{S}(\mathbf{U}) \quad (2.11)$$

Labeling with  $H_x$  and  $H_y$  the solving schemes for the homogeneous systems (2.9) and (2.10) respectively, and with  $S$  the scheme for the "source" system (2.11), the numerical procedure which advances the flow variables from the starting values  $W^n = (u^n, v^n, d^n)$  to the final values  $W^{n+1} = (u^{n+1}, v^{n+1}, d^{n+1})$ , with the bed depth  $z_b^n$  remaining constant, is summarized as follows:

$$W^{n+1} = \frac{1}{2} \{H_{xy} [S(W^n)] + S[H_{xy}(W^n)]\} \quad (2.12)$$

where

$$H_{xy}(W) = \frac{1}{2} \{H_x[H_y(W)] + H_y[H_x(W)]\}. \quad (2.13)$$

### Finite-volume discretization

Schemes  $H_x$  and  $H_y$ , which are formally the same except for the coordinate direction considered, are based on a finite-volume approach executed on a discretization of the computational domain into operational *cells*. By performing the discretization, the *continuous* domain is replaced by a *finite* set of cells at which an approximate value of the real solution is computed.

As an example, consider the scheme  $H_x$  for the augmented 1-dimensional homogeneous system (2.9):

$$H_x : \mathbf{U}_{,t} + \mathbf{F}(\mathbf{U})_{,x} = 0 \quad (2.14)$$

In order to solve (2.14) the  $x - t$  domain is discretized beforehand; the spatial domain  $x$  is replaced by a certain number of computing cells of width  $\Delta x$ , while the temporal range  $t$  is divided into a succession of time step of

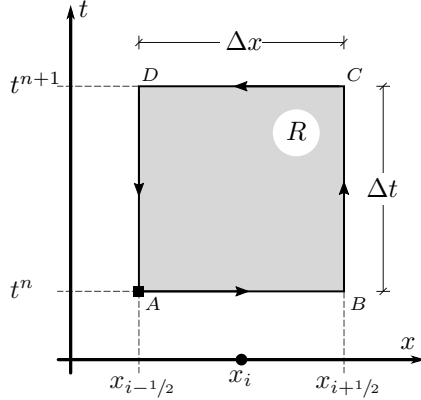


Figure 2.3: Sketch of the control volume  $R$  used for the  $x-t$  domain discretization and the integral form of the monodimensional homogeneous system  $H_x$  (2.9).

length  $\Delta t$ . The rectangular subdomain  $R = [x_{i-1/2}, x_{i+1/2}] \times [t^n, t^{n+1}]$  is then assumed as a *control volume*, the fundamental unit of the discretization. A schematic of the control volume adopted for the discretization is presented in Figure 2.3. From here on, the subscript  $i$  denotes the computing cell, whereas the superscript  $n$  denotes the time step.  $x_{i-1/2}$  and  $x_{i+1/2}$  identify the intercell boundaries, between  $x_{i-1}$  and  $x_i$  and between  $x_i$  and  $x_{i+1}$  respectively.

System (2.14) is integrated over the control volume  $R$ : to this purpose the integral form of system (2.14) is adopted, since it provides useful integral expressions of the involved quantities and requires less smoothness to the solution, thus allowing shock waves as discontinuities. Through application of the Green theorem to convert a double integral into a line integral defined over the boundary of a closed region, the following relation is obtained:

$$\int_R [\mathbf{U},_t + \mathbf{F}(\mathbf{U}),_x] \, dr = \oint_{\partial R} [\mathbf{U} \, dx - \mathbf{F}(\mathbf{U}) \, dt] = 0. \quad (2.15)$$

Now we integrate the line integral in (2.15) along the boundary of the control volume. With reference to Figure 2.3, starting from point  $A$  and proceeding in an anticlockwise manner, one obtains:

$$\underbrace{\int_{x_{i-1/2}}^{x_{i+1/2}} \mathbf{U}(x, t^n) \, dx}_{AB} - \underbrace{\int_{t^n}^{t^{n+1}} \mathbf{F}(x_{i+1/2}, t) \, dt}_{BC} + \underbrace{\int_{x_{i-1/2}}^{x_{i+1/2}} \mathbf{U}(x, t^{n+1}) \, dx}_{CD} - \underbrace{\int_{t^n}^{t^{n+1}} \mathbf{F}(x_{i-1/2}, t) \, dt}_{DA} = 0. \quad (2.16)$$

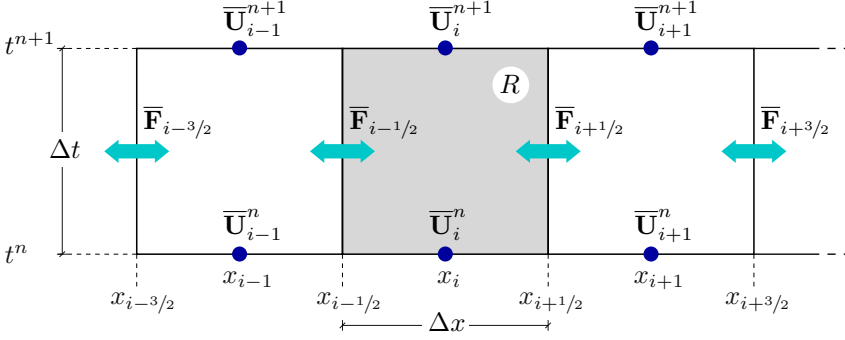


Figure 2.4: Representation of the averaged variables in equation (2.17) along the boundary of a control volume  $R$ .

The four integrals in (2.16) represent the integrals of the components of the variables vector  $\mathbf{U}$  and the flux vector  $\mathbf{F}$  along the four edges of the control volume  $R$ . We now replace all of them with their respective spatial or temporal averages, defined as follows:

$$\bar{\mathbf{U}}_i^n = \frac{1}{\Delta x} \int_{x_{i-1/2}}^{x_{i+1/2}} \mathbf{U}(x, t^n) dx, \quad \bar{\mathbf{U}}_i^{n+1} = \frac{1}{\Delta x} \int_{x_{i-1/2}}^{x_{i+1/2}} \mathbf{U}(x, t^{n+1}) dx,$$

$$\bar{\mathbf{F}}_{i+1/2} = \frac{1}{\Delta t} \int_{t^n}^{t^{n+1}} \mathbf{F}(x_{i+1/2}, t) dt, \quad \bar{\mathbf{F}}_{i-1/2} = \frac{1}{\Delta t} \int_{t^n}^{t^{n+1}} \mathbf{F}(x_{i-1/2}, t) dt.$$

Plugging the integral averages into (2.16) and rearranging the terms, one obtains the following explicit conservative formula for the unknown averaged vector  $\bar{\mathbf{U}}_i^{n+1}$ :

$$\bar{\mathbf{U}}_i^{n+1} = \bar{\mathbf{U}}_i^n + \frac{\Delta t}{\Delta x} (\bar{\mathbf{F}}_{i-1/2} - \bar{\mathbf{F}}_{i+1/2}). \quad (2.17)$$

A sketch of the involved quantities and their location within the control volume is represented in Figure 2.4. In the picture, the averaged vectors of the unknowns  $\bar{\mathbf{U}}$  are represented by the blue dots, while the numerical fluxes  $\bar{\mathbf{F}}$  are represented by the teal bidirectional arrows. The control volume for which equation (2.17) is defined is shaded in gray and is represented with two adjacent control volumes, with which it shares the boundary fluxes. It is worth recalling that (2.17) is a vector equation, that translates into three scalar equations, each involving the homologous components of  $\bar{\mathbf{U}}$  and  $\bar{\mathbf{F}}$ .

Equation (2.17) allows to advance the averaged values of the conserved variables ( $d$ ,  $ud$ , and  $vd$ ) from the time level  $n$  to the time level  $n+1$ . For the equation to be solvable, though, one needs to prescribe suitable approximations for the *numerical fluxes*  $\bar{\mathbf{F}}_{i\pm 1/2}$  that appear at the right hand side of the equation. Several different definitions for the numerical fluxes are available in the literature: in the present solver, fluxes are evaluated with the WAF method,

which will be briefly described in the following section.

The "source" system (2.11), which encloses gravity and friction terms, does not have any flux contribution and therefore can be easily resolved using standard methods for solving sets of ODEs, such as the Euler method and the Runge-Kutta method.

## The WAF method

The WAF method [62, 86] is intended to solve initial value problems for systems of conservation laws in the form (2.9). It is a generalization of the Lax-Wendroff and the Godunov first-order upwind schemes for nonlinear systems: the novelty resides in how the intercell fluxes appearing in formula (2.17) are evaluated. Whereas the Godunov method samples a flux estimate at a single point, i.e. at the interface between computing cells, the WAF method executes a weighted average of the flux function over the whole solution structure of a specific initial value problem (IVP) called Riemann problem, and at a specific time instant within the computational time step  $\Delta t$ . If the flux estimate is evaluated at half the time step,  $t^* = \frac{1}{2}\Delta t$ , the WAF method coincides with the well-known Lax-Wendroff scheme. The WAF method, which is inherently second-order accurate, has been successfully applied to problems of gas dynamics (Euler equations) with shock waves [87] and to shallow water propagation problems [85, 88, 89]. The basic form of the WAF method is unusable in practice since it produces spurious oscillations in presence of shock waves; a simple adjustment of the method has been since developed to deal with singularities and other events involving steep gradients in the solution.

At the basis of the method is the assumption that, for any time level, the solution  $\bar{\mathbf{U}}_i^n$  is represented by a piecewise constant distribution. In other words, the solution at any cell  $i$  is a constant value defined by the integral spatial average of the true data over the cell width  $\Delta x$ . Therefore, the solution itself can be regarded as pairs of constant data separated by jump discontinuities at the interfaces between adjacent cells. Hereinafter we will neglect the overbar symbol since we have clarified that the components of the variable vector  $\mathbf{U}$  are spatial-averaged and, thus, piecewise constant over a single cell.

Without loss of generality, at the boundary  $x_{i+1/2}$  between cells  $i$  and  $i+1$  we can ultimately define a particular IVP, called *Riemann problem*. A comprehensive review of the pivotal role of the Riemann problem in computational sciences is presented in [90]. In the Riemann problem the set of nonlinear conservation laws (2.9), rewritten in quasi-linear form for solving purposes, is equipped with a piecewise initial state made of two constant values separated

by a discontinuity at the interface:

$$RP : \begin{cases} \mathbf{U}_{,t} + \mathbf{F}(\mathbf{U})_{,x} = \mathbf{U}_{,t} + \mathbf{A}\mathbf{U}_{,x} = 0 \\ \mathbf{U}(x, t = 0) = \begin{cases} \mathbf{U}_L = \mathbf{U}_i^n & \text{if } x < x_{i+1/2} \\ \mathbf{U}_R = \mathbf{U}_{i+1}^n & \text{if } x > x_{i+1/2} \end{cases} \end{cases} \quad (2.18)$$

System (2.9) is a set of conservation laws, hence it is hyperbolic and its structure can be analyzed using classic methods available for solving systems of hyperbolic first-order PDEs. Among these, one of the most popular and useful is the method of characteristics [61, 91]: according to this method, the characteristics curves describing the propagation of signals in the medium are obtained as eigenvalues of the Jacobian matrix  $\mathbf{A} = \partial\mathbf{F}(\mathbf{U})/\partial\mathbf{U}$ . For the Riemann problem (2.18), the Jacobian matrix  $\mathbf{A}$  reads:

$$\mathbf{A} = \begin{vmatrix} 0 & 1 & 0 \\ c^2 - u^2 & 2u & 0 \\ -uv & v & u \end{vmatrix} \quad \text{with } c = \sqrt{gd}. \quad (2.19)$$

The eigenvalues  $\lambda_k$  of  $\mathbf{A}$  are the roots of its characteristic polynomial

$$P(\lambda) = \det(\mathbf{A} - \lambda\mathbf{I}) = (u - \lambda) [\lambda(2u - \lambda) + c^2 - u^2] = 0 \quad (2.20)$$

which is a cubic equation, thus admitting three roots. It is readily seen that the three eigenvalues are  $(\lambda_1, \lambda_2, \lambda_3) = (u - c, u, u + c)$ : they are all real (note that this is a necessary, but not sufficient condition for assessing the hyperbolicity of a system of PDEs) and distinct when  $c \neq 0$ , i.e. on wet bed.

The existence of three real eigenvalues defines three distinct families of characteristic curves in the  $x - t$  plane, which describe the propagation of distinct signals, simply known as *waves*. The "outer" waves, corresponding to the eigenvalues  $\lambda_1 = u - c$  and  $\lambda_3 = u + c$ , are genuinely non-linear and can be either *shock waves* or *rarefaction waves*. A rarefaction wave is a flow region that creates a smooth transition between two adjacent states; on the other hand, a shock wave is a transition layer across which flow quantities change very rapidly. The wave corresponding to the eigenvalue  $\lambda_2 = u$ , finally, is always linearly degenerate and is called *contact discontinuity*. A comprehensive description of all the aforementioned wave structures can be found in [62]. The three wave families divide the  $x - t$  space into four regions of constant states and hence define completely the structure of the solution of the Riemann problem (2.18).

In Figure 2.5 a sketch of the solution structure for the Riemann problem (2.18) is presented. As it can be seen, the piecewise initial conditions of the Riemann problem,  $\mathbf{U}_L$  and  $\mathbf{U}_R$ , evolve in time generating two internal zones of states  $\mathbf{U}_L^*$  and  $\mathbf{U}_R^*$ , whose values are unknown. According to the WAF

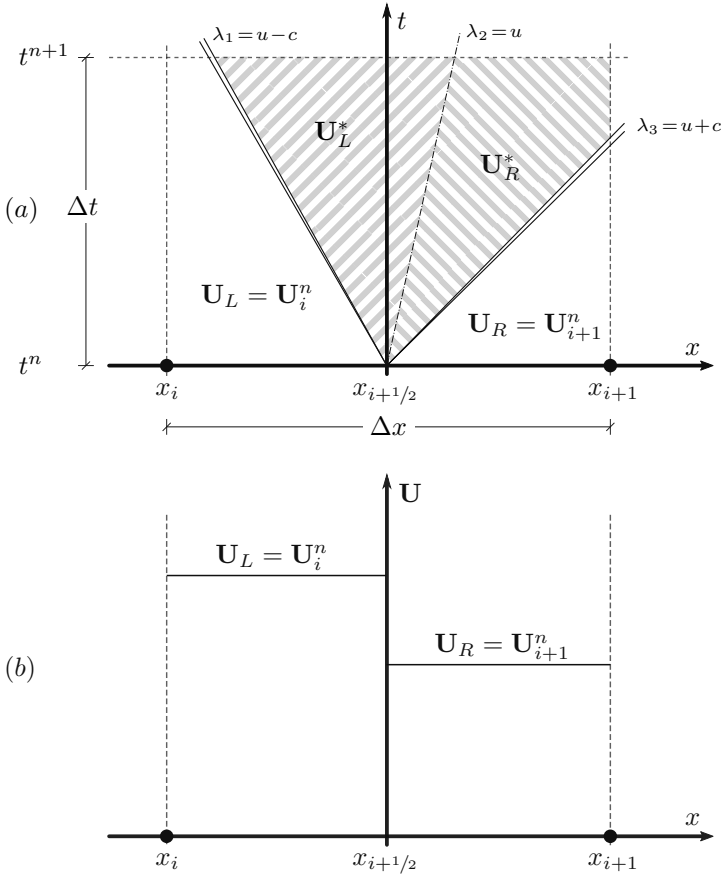


Figure 2.5: Solution of the Riemann problem (2.18). (a): complete structure of the solution in the  $x-t$  plane. Two unknown states  $\mathbf{U}_L^*$  and  $\mathbf{U}_R^*$  arise in the shaded areas. (b): piecewise constant initial condition of the problem, defined between the cells  $i$  and  $i+1$ .

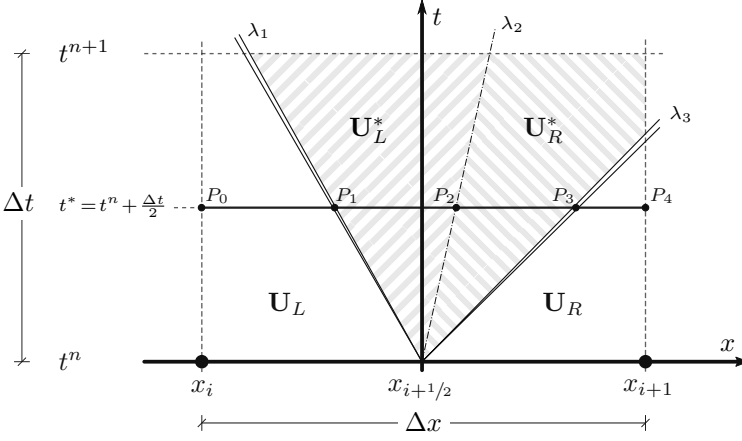


Figure 2.6: Structure of the solution of the Riemann problem (2.18). The flux is computed from all the constant  $\mathbf{U}$  states originating from the solution of the Riemann problem, and evaluated along the segment  $P_0P_4$ .

method, the values of the intercell flux  $\bar{\mathbf{F}}_{i+1/2}$  can be completely computed once the piecewise constant structure of the solution  $\mathbf{U}$  is known over the entire cell width  $\Delta x = x_{i+1} - x_i$  at half the time step,  $\frac{\Delta t}{2}$ :

$$\bar{\mathbf{F}}_{i+1/2} = \bar{\mathbf{F}}\left(\mathbf{U}_{i+1/2}^{n+1/2}\right).$$

Recalling the definition of flux given in (2.6)–(2.7), it is immediately clear that, since the variables  $\mathbf{U}$  are piecewise constant, also the flux  $\mathbf{F} = \mathbf{F}(\mathbf{U})$  will be piecewise constant too: this assessment allows us to drop the overbar signs even for fluxes. In summary, the structures of variables and fluxes for the Riemann problem are as follows:

$$\mathbf{U}_{i+1/2}^{n+1/2} = \begin{cases} \mathbf{U}_L = \mathbf{U}_i^n & \text{for } t = t^{n+1/2} \text{ and } P_0 < x < P_1 \\ \mathbf{U}_L^* & \text{for } t = t^{n+1/2} \text{ and } P_1 < x < P_2 \\ \mathbf{U}_R^* & \text{for } t = t^{n+1/2} \text{ and } P_2 < x < P_3 \\ \mathbf{U}_R = \mathbf{U}_{i+1}^n & \text{for } t = t^{n+1/2} \text{ and } P_3 < x < P_4 \end{cases} \quad (2.21)$$

$$\mathbf{F}_{i+1/2} = \begin{cases} \mathbf{F}_L = \mathbf{F}(\mathbf{U}_i^n) & \text{for } t = t^{n+1/2} \text{ and } P_0 < x < P_1 \\ \mathbf{F}(\mathbf{U}_L^*) & \text{for } t = t^{n+1/2} \text{ and } P_1 < x < P_2 \\ \mathbf{F}(\mathbf{U}_R^*) & \text{for } t = t^{n+1/2} \text{ and } P_2 < x < P_3 \\ \mathbf{F}_R = \mathbf{F}(\mathbf{U}_{i+1}^n) & \text{for } t = t^{n+1/2} \text{ and } P_3 < x < P_4 \end{cases} \quad (2.22)$$

The final operative value of the intercell flux to be used in (2.17) is obtained

with a weighted average of the fluxes appearing in (2.22), evaluated at time  $t^* = t^n + \frac{\Delta t}{2}$ :

$$\mathbf{F}_{i+1/2} = \omega_1 \mathbf{F}(\mathbf{U}_i^n) + \omega_2 \mathbf{F}(\mathbf{U}_L^*) + \omega_3 \mathbf{F}(\mathbf{U}_R^*) + \omega_4 \mathbf{F}(\mathbf{U}_{i+1}^n), \quad (2.23)$$

where the weights  $\omega_k$  are the lengths of the segments  $\overline{P_{k-1}P_k}$  over which the single fluxes are defined, normalized to the whole cell width  $\Delta x$ . Applying simple geometric reasonings on the Riemann problem structure illustrated in Figure 2.6 the segment lengths and relative weights are:

$$\overline{P_0P_1} = \frac{\Delta x}{2} + \lambda_1 \frac{\Delta t}{2}, \quad \overline{P_1P_2} = \lambda_2 \frac{\Delta t}{2} - \lambda_1 \frac{\Delta t}{2}, \quad (2.24)$$

$$\overline{P_2P_3} = \lambda_3 \frac{\Delta t}{2} - \lambda_2 \frac{\Delta t}{2}, \quad \overline{P_3P_4} = \frac{\Delta x}{2} - \lambda_3 \frac{\Delta t}{2}, \quad (2.25)$$

$$\omega_1 = \frac{\overline{P_0P_1}}{\Delta x} = \frac{1}{2} \left[ 1 + \lambda_1 \frac{\Delta t}{\Delta x} \right], \quad \omega_2 = \frac{\overline{P_1P_2}}{\Delta x} = \frac{1}{2} \frac{\Delta t}{\Delta x} [\lambda_2 - \lambda_1], \quad (2.26)$$

$$\omega_3 = \frac{\overline{P_2P_3}}{\Delta x} = \frac{1}{2} \frac{\Delta t}{\Delta x} [\lambda_3 - \lambda_2], \quad \omega_4 = \frac{\overline{P_3P_4}}{\Delta x} = \frac{1}{2} \left[ 1 - \lambda_3 \frac{\Delta t}{\Delta x} \right]. \quad (2.27)$$

It is readily seen that the weights (2.26)–(2.27) sum up to one. Plugging the weights into (2.23) and a bit of manipulation give a compact formula for the WAF flux at the interface between cells:

$$\mathbf{F}_{i+1/2} = \frac{1}{2} [\mathbf{F}(\mathbf{U}_i^n) + \mathbf{F}(\mathbf{U}_{i+1}^n)] - \frac{1}{2} \sum_{k=1}^3 c_k \Delta \mathbf{F}^{(k)} \quad (2.28)$$

where  $\Delta \mathbf{F}^{(k)}$  represents the flux jump across the  $k^{\text{th}}$  wave and  $c_k = \lambda_k \frac{\Delta t}{\Delta x}$  is the Courant number of the  $k^{\text{th}}$  wave.

It is worthwhile to observe that the WAF method described above solves for the flow variables of the shallow water equations on the hypothesis of a horizontal, plain bottom profile. In the basic version of the method, therefore, the source terms related to the spatial bottom gradients  $z_{b,x}$  and  $z_{b,y}$  appearing in (2.8) are not contemplated. In order to consider the effect of a variable beach profile on water flow, the WAF method is reformulated in such a way that the source terms accounting for the bottom slopes are incorporated into the local Riemann problem, yet preserving the second-order accuracy of the method [88].

### Flux limiter

The WAF flux expressed in (2.28) can't be used in practice because, as a consequence of Godunov's theorem [62, 86, 92], any second-order accurate scheme with constant coefficients (like the Lax-Wendroff method, for which the WAF

method is an extension to nonlinear systems) is bound to generate spurious oscillations wherever the solution shows high gradients, like in the presence of shock waves, bores and other discontinuities. A way to prevent this undesired phenomenon is to resort to total variation diminishing (TVD) schemes which, as their name reveals, make the total variation of the solution a decreasing (or at least non-increasing) function of computational time. This constraint ensures that no unwanted local extrema may be created in the evolving solution and that an existing local minimum (maximum) may not decrease (increase) [93].

A TVD version of the WAF method is achieved by slightly modifying the expression for the WAF flux (2.28) with a *flux limiter*. The purpose of introducing a flux limiter is to keep the numerical flux jumps that figure in the formulation of the WAF method (2.28) into reasonable ranges, to limit as much as possible the generation and evolution of spurious oscillations in proximity of shocks and discontinuities of the flow. From a numerical viewpoint, this is made by amplifying empirically the wave speeds in the solution of the Riemann problem (2.18) in order to alter the flux weights (2.26)–(2.27) while keeping the solution structure unaltered [85]. The modified version of the WAF flux is:

$$\mathbf{F}_{i\pm 1/2} = \frac{1}{2}[\mathbf{F}(\mathbf{U}_i^n) + \mathbf{F}(\mathbf{U}_{i\pm 1}^n)] - \frac{1}{2} \sum_{k=1}^3 \text{sgn}(c_k) f^{(k)} \Delta \mathbf{F}^{(k)} \quad (2.29)$$

where the newly introduced component  $f^{(k)}$  is the flux limiter function to be applied to the  $k^{\text{th}}$  wave and is a function of the flow features. The flux limiter used in the present solver is the SUPERA.

The intercell WAF fluxes  $\mathbf{F}_{i-1/2}$  and  $\mathbf{F}_{i+1/2}$  are now fully determined by expression (2.29) and can be plugged into the explicit formula (2.17) to advance the solution (the variables vector  $\mathbf{U}_i^n$ ) from time level  $n$  to time level  $n + 1$ .

The reader is referred to [94] for a comprehensive review of several flux limiter functions developed by scientists in the last decades, and [62] for a selection of the most used ones.

### The shoreline boundary conditions

It is of crucial importance for a shallow water hydrodynamic solver for coastal engineering to properly reproduce the oscillatory motion of the shoreline, i.e. the boundary line between the wet and dry domains, continuously pushed back and forward by the incoming waves. Establishing an appropriate representation of this boundary, however, carries many difficulties, since its oscillatory motion is determined by the incoming waves and hence is part of the solution itself. Only in recent years some effort has been spent in investigating and dealing with the issues that arise when nearshore circulation models are implemented with shoreline models.

In the present solver Brocchini et al. [1] aimed at defining an accurate and efficient discrete version of the boundary conditions for a moving shoreline:

$$\frac{dx_s}{dt} = u_s, \quad d_s = 0, \quad (2.30)$$

which, in simple words, state that  $u_s$  is the velocity of motion of the instantaneous shoreline position  $x_s$ , and the water depth at the shoreline  $d_s$  must be zero. The issue is tackled by characterizing and solving a physically correct wet-dry Riemann problem located right at the interface between the last "wet cell" and the first "dry cell" of the computational grid. By pursuing this approach, there is no need for a special treatment of the shoreline, since it is resolved by using the same numerical technique used in any other location in the computational domain, i.e. the WAF method based on the solution of a local Riemann problem. This approach is particularly effective when applied on solvers that work on a fixed grid and it has been seen to give satisfying results in predicting shoreline motions. For a discussion of advantages and drawbacks of this methodology in comparison with a different approach for moving grids see [95].

Still focusing our attention on the  $x$ -direction homogeneous problem (2.14) (since the same process can be applied to the  $y$ -direction problem), the wet-dry Riemann problem at the base of the shoreline treatment is defined as follows:

$$RP : \begin{cases} \mathbf{U}_{,t} + \mathbf{F}(\mathbf{U})_{,x} = \mathbf{U}_{,t} + \mathbf{A}\mathbf{U}_{,x} = 0 \\ \mathbf{U}(x, t = 0) = \begin{cases} \mathbf{U}_L = (u_L, d_L) & \text{if } x < x_{i+1/2} \\ \mathbf{U}_R = \mathbf{0} & \text{if } x > x_{i+1/2} \end{cases} \end{cases} \quad (2.31)$$

where  $\mathbf{U}_L$  is the state of the last wet cell and  $\mathbf{U}_R$  is the state of the first dry cell, which is obviously equal to zero since no fluid is present in the dry portion of the domain. The solution of problem (2.31) consists of a single rarefaction wave, and a contact wave that corresponds to the tail of such rarefaction wave. The contact discontinuity can be identified as the *wet-dry front*, i.e. the shoreline; hence, the speed of the contact wave is the speed of the shoreline  $u_s$ . The solution of the wet-dry problem (2.31) leads directly to an expression for the unknown shoreline velocity:

$$\frac{dx_s}{dt} = u_s = u_L + 2c_L \text{ with } c_L = \sqrt{gd_L} \quad (2.32)$$

where  $d_L$  and  $u_L$  is the (known) depth and velocity state at the left of the interface, i.e. at the last wet cell.

Exactly as it has been determined in the case of a totally wet Riemann problem (2.18), the structure of the solution of the wet-dry problem depicted in

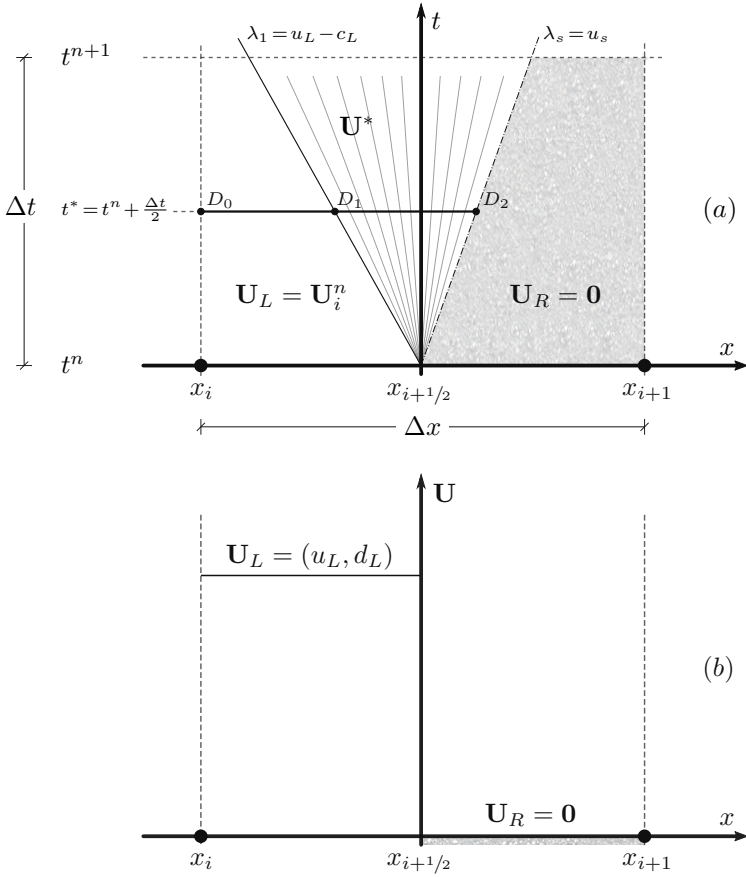


Figure 2.7: Structure of the solution of the wet-dry Riemann problem (2.31). The WAF flux at the shoreline is computed from the  $\mathbf{U}$  states along the segment  $D_0D_2$ .

Figure 2.7 can be exploited to compute an estimate of the intercell flux  $\mathbf{F}_{i+1/2}$  to be used in the discrete formula (2.17):

$$\mathbf{F}_{i+1/2} = \frac{1}{\Delta x} \left[ \left( \lambda_1 \frac{\Delta t}{2} + \frac{\Delta x}{2} \right) \mathbf{F}(u_L, d_L) + (\lambda_s - \lambda_1) \frac{\Delta t}{2} \hat{\mathbf{F}} \right]. \quad (2.33)$$

$\lambda_1 = u_L - c_L$  is the characteristic speed associated to the rarefaction wave;  $\lambda_s = u_s$  is the speed of the contact wave.  $\hat{\mathbf{F}}$  is the contribution to the WAF flux due to the expansion fan, which has been computed adopting a trapezoidal rule of order two to give the following formula:

$$\hat{\mathbf{F}} = \frac{1}{4} \mathbf{F}(u_L, d_L) + \frac{1}{2} \mathbf{F}(\tilde{u}, \tilde{d}) + \frac{1}{4} \mathbf{F}(u_s, 0), \quad (2.34)$$

where  $\tilde{u} = \frac{u_L + u_s}{2}$  and  $\tilde{d} = \frac{d_L}{2}$  are the fluid velocity and water depth at the center of the expansion fan, respectively.

The solution of the Riemann problem at the shoreline allows to advance the flow variables for both the wet and dry cells over a single time step. However, this process must be coupled with a suitable *wetting/drying procedure* to decide whether the dry cell should be considered "wet" for the following time step (in case of a runup) or, conversely, whether a previously wet cell should be drained and labeled "dry" for the following time step (in case of a rundown). By doing so, the instantaneous boundary between the wet and dry domains can be moved to simulate the shoreline motion. In the wetting phase, the WAF method is applied to the first dry cell to compute an estimate of the inflow water volume at that cell; this value, divided by the cell depth, gives an equivalent water depth for the dry cell. If the equivalent depth is greater than a predefined threshold  $d_{min}$ , then the cell is inundated and will be assumed as the last wet cell for the subsequent time step. In the drying phase, the water depth at the last wet cell is considered; if this depth is lower than the threshold value, the cell is drained and assumed as the first dry cell for the following time step.

## 2.4.2 The morphodynamic module

The morphodynamic module (see the article by Postacchini et al. [79] for details [96]) has been conceived to be consistent with the numerical approach adopted for the resolution of the hydrodynamic module described in section 2.4.1. To this end, a finite-volume approach with application of the WAF method has been also used to discretize and integrate the Exner equation and thus update in time the bed depth  $z_b^n$  at the mesh nodes. Since our NSWEs-Exner model (2.1) is weakly coupled, during the morphodynamic step, the flow variables  $u, v$  and  $d$  are taken as constant.

Integration of the Exner equation (2.1d) over the 3-dimensional subdomain

$[x_{i-1/2}, x_{i+1/2}] \times [y_{j-1/2}, y_{j+1/2}] \times [t^n, t^{n+1}]$ , application of the Green theorem and averaging of the contributions in space and time give the following discretized form:

$$(z_b)_{i,j}^{n+1} = (z_b)_{i,j}^n - \frac{1}{\lambda} \left\{ \frac{\Delta t}{\Delta x} [(q_x)_{i+1/2,j}^{n+1/2} - (q_x)_{i-1/2,j}^{n+1/2}] + \frac{\Delta t}{\Delta y} [(q_y)_{i,j+1/2}^{n+1/2} - (q_y)_{i,j-1/2}^{n+1/2}] \right\}, \quad (2.35)$$

where  $i$  and  $j$  represent the node position in the  $x$  and  $y$  direction respectively,  $\Delta t$  is the time step,  $\Delta x$  and  $\Delta y$  are the grid sizes in the  $x$  and  $y$  direction, and  $q_x$  and  $q_y$  are averaged total sediment intercell fluxes which, again, can be evaluated using the WAF method.

Before solving the Exner equation numerically by means of (2.35), suited closure formulas for modeling the two components concurring to the total sediment transport rate  $\mathbf{q}$  — namely the bed load  $\mathbf{q}_b$  and the suspended load  $\mathbf{q}_s$  — must be chosen. Among the several bed load transport formulas available, the most favored for their acknowledged simplicity and validity are power laws like that of Grass [74]:

$$\mathbf{q}_b = A\mathbf{v}|\mathbf{v}|^n \quad (2.36)$$

and Kelly and Dodd [97]:

$$\mathbf{q}_b = Bd\mathbf{v}|\mathbf{v}|^2, \quad (2.37)$$

where  $A$  and  $B$  are constant parameters that depend on the sediment characteristics. The bed load closure formula used in the present solver, however, is the more complex formulation by Meyer-Peter and Müller [98, 99]:

$$\mathbf{q}_b = 8\sqrt{\left(\frac{\rho_s - \rho}{\rho}\right)gd_{50}^3} (|\boldsymbol{\theta} - \chi\nabla z_b| - \theta_c)^{1.5} \frac{\boldsymbol{\theta} - \chi\nabla z_b}{|\boldsymbol{\theta} - \chi\nabla z_b|}, \quad (2.38)$$

where the vector  $\boldsymbol{\theta} = |\theta_x, \theta_y|$  gathers the dimensionless Shields parameters in both spatial directions and is defined as

$$\boldsymbol{\theta} = \frac{\boldsymbol{\tau}}{(\rho_s - \rho)gd_{50}} = c_\tau \frac{\rho\mathbf{v}|\mathbf{v}|}{(\rho_s - \rho)gd_{50}}, \quad (2.39)$$

$\theta_c$  is the critical Shields parameter value for the entrainment of sediment,  $\rho$  and  $\rho_s$  are the density of water and sediment respectively,  $d_{50}$  is the median diameter of sediment, and  $\chi$  is an adimensional number accounting for the effects of seabed slope (e.g. the stabilizing effect over sediment due to strong bottom gradients). The formulation (2.38) is preferred since it encompasses

mechanisms and parameters that simpler laws usually neglect, such as the stabilizing effect of gravity, the influence of sediment granulometry and the existence of a threshold for sediment motion.

As for suspended load sediment transport formulas, the closure model adopted in this solver is the one by Camenen and Larson [100]:

$$\mathbf{q}_s = \mathbf{v} c_R \frac{\epsilon}{w_s} \left[ 1 - e^{-\frac{w_s d}{\epsilon}} \right], \quad (2.40)$$

where  $w_s$  is the sediment settling velocity,  $\epsilon$  is the sediment diffusivity and  $c_r$  is a reference concentration of sediment, defined as:

$$c_R = A_c |\boldsymbol{\theta}_T| e^{-4.5 \frac{|\boldsymbol{\theta}_M|}{\theta_c}} \quad (2.41)$$

where  $A_c$  is, again, a parameter depending on sediment characteristics and  $\boldsymbol{\theta}_T$  and  $\boldsymbol{\theta}_M$  are the mean and maximum adimensional shear stresses, respectively.

### 2.4.3 The LES model

The hydro-morphological response of shallow waters in nearshore areas is bound to be deeply influenced by turbulence. Although significant progress has been made in understanding more about the features and structures of turbulent flow, thanks to statistical theories, extensive experimental studies and advanced techniques of flow measurement and visualization, a complete analytical description of turbulence still remains a formidable problem in fluid dynamics.

A consistent help in shedding light over turbulent processes comes from numerical models that are able to resolve turbulent flow features up to various levels of detail. One of the most common numerical approaches to model turbulent flows is to resort to Reynolds' averaging of flow quantities over a time interval greater than all the temporal scales of turbulence: in this way one obtains the Reynolds-averaged Navier-Stokes (RANS), a set of equations for the evolution of the mean flow properties. In the RANS framework, the effect of turbulence due to flow fluctuations appears in the governing equations in the form of Reynolds stresses, which must be represented with one of the several closure schemes available (e.g. the  $k - \epsilon$  model [101], the mixing length model [102] and the Reynolds stress equation model) to completely define the problem. Such models, however, are required to resolve a wide range of spatial and temporal scales to be able to represent turbulence effectively and, therefore, are often characterized by a high degree of complexity.

A very straightforward and accurate representation of turbulent motions can be otherwise achieved with Direct Numerical Simulation (DNS) of the model Navier-Stokes equations. Such an approach can theoretically predict turbulence features down to the smallest dissipative scales, provided the com-

putational mesh is fine enough (the spatial resolution of the flow must therefore be smaller than the smallest turbulence scale of interest). While potentially amenable to compute any quantity of interest, DNS models are greatly expensive from a computational viewpoint and require greater mesh resolution as the Reynolds number of the flow increases [103]: their application has been thus limited to simple geometries and flows with relatively low Reynolds numbers.

A useful compromise between RANS and DNS computations is the Large Eddy Simulation (LES) model approach [104, 105, 106]. In LES only the contribution of the "large" turbulent motions, occurring at a length scale greater than a predefined filter size usually taken as the computational grid size, is resolved exactly. The effect of turbulence at sub-grid scales (SGS) is accounted for with appropriate models that connect the properties of turbulence with those of the mean flow field. The reader is referred to [104] and [105] for an exhaustive discussion of the LES technique, the most common SGS models and the numerical issues to be faced.

Turbulence models are a valuable help in investigating the dynamics of nearshore and shallow water bodies like coastal waters, rivers and estuaries, which are often characterized by the presence of large coherent vortical structures with a vertical axis, generally known as macrovortices. Large eddies can gradually form after the rearrangement of an initially random turbulence field [107] and their generation is usually correlated with the energy transfer from the largest flow structures to the smallest (dissipative) ones and viceversa, as well as other factors like breaking unevenness due to varying topography in both cross-shore and alongshore directions [108, 109]. A number of studies ascertained that macrovortices are powerful agents in phenomena like flow mixing [110, 111, 112], entrainment and distribution of sediment [113, 114] and advection of passive tracers [115]. As a natural consequence, macrovortices are crucial in defining the geomorphological response of many environments, such as barred beaches [116], riverine systems [105, 117, 118] and compound channels [119, 120].

The description and investigation of mainly 2-dimensional turbulent structures within the framework of our depth-averaged solver is performed by means of a horizontal LES model where the filtering length is assumed to be the equal to the computational mesh size; to give account of the dissipative sub-grid scales of turbulence, a SGS model based on a variable eddy viscosity formulation proposed by Grosso et al. [121] is adopted. To this end, the NSWEs equations (2.1a-c) are complemented with additional source terms  $F_x$  and  $F_y$  to the momentum balance equations, representing the dissipative body forces due to the effects of wave breaking and turbulence. They are introduced with

a typical Laplacian-type formulation as in the following:

$$F_x = \frac{(dT_{xx})_{,x} + (dT_{xy})_{,y}}{d}, \quad (2.42)$$

$$F_y = \frac{(dT_{xy})_{,x} + (dT_{yy})_{,y}}{d}. \quad (2.43)$$

$T_{xx}$ ,  $T_{yy}$  and  $T_{xy}$  are the components of the Reynolds stress tensor for turbulent flows, for which a simple closure model is considered:

$$T_{xx} = 2\nu_T u_{,x}, \quad T_{yy} = 2\nu_T v_{,y}, \quad T_{xy} = \nu_T (u_{,y} + v_{,x}), \quad (2.44)$$

where  $\nu_T$  is a depth-averaged effective eddy viscosity, defined as a function of the water depth:

$$\nu_T = \lambda g^{1/2} d^{3/2}. \quad (2.45)$$

From an operative point of view, expressions (2.42-2.43) are included among the source terms along with the bed friction terms  $B_x$  and  $B_y$ , and used to solve the "source" problem (2.11) in a discrete way. Implementing a second-order centered difference scheme to discretize problem (2.11) over the time step  $\Delta t$  the following expressions are obtained:

$$\begin{aligned} u_{i,j}^{n+1} = & u_{i,j}^n + \nu_T \Delta t [2u_{,xx} + u_{,yy} + v_{,xy} + 2d_{,x} u_{,x} + d_{,y} (v_{,x} + u_{,y})] + \\ & + \frac{\nu_T}{d} \Delta t \left[ 3d_{,x} u_{,x} + \frac{3}{2} d_{,y} u_{,y} + \frac{3}{2} d_{,y} v_{,x} \right] - \Delta t B_x, \end{aligned} \quad (2.46)$$

$$\begin{aligned} v_{i,j}^{n+1} = & v_{i,j}^n + \nu_T \Delta t [2v_{,yy} + v_{,xx} + u_{,xy} + 2d_{,y} v_{,y} + d_{,x} (u_{,y} + v_{,x})] + \\ & + \frac{\nu_T}{d} \Delta t \left[ \frac{3}{2} d_{,x} u_{,y} + \frac{3}{2} d_{,x} v_{,x} + 3d_{,y} v_{,y} \right] - \Delta t B_y. \end{aligned} \quad (2.47)$$

By means of the expressions (2.46) and (2.47) the values of the depth-averaged velocities  $u_{i,j}$  and  $v_{i,j}$  are "corrected" by the eddy viscosity contributions, to give account of the effect of sub-grid turbulence. The presence and entity of the viscosity "correction" is determined by the value of the calibration parameter  $\lambda$  figuring in the definition of the variable eddy viscosity (2.45). If  $\lambda = 0$  the turbulent sub-grid scales are not modeled and the HLES technique is deactivated: the dissipative terms (2.42-2.43) are not included in the numerical model and the corrective contribution due to viscosity in (2.46-2.47) are not present, the only corrections being those due to the effect of friction. A value of  $\lambda$  different than zero activates HLES and includes the dissipative effects into the numerical model.

In this thesis a sensitivity analysis for  $\lambda$  is performed by carrying out wave-current interaction tests with the NSWE/HLES model described above. In these tests different values of  $\lambda$  are assumed in a range from 0 to 0.1, and the differences in flow structures are investigated in section 4.2.3.

#### 2.4.4 The estuary model

The basic version of the NSWE solver described in the previous sections accepts a wave input in the form of a time series of both elevation of water surface and water depth-averaged orbital velocity. The input is applied at the grid nodes at the seaward domain edge, which therefore work as boundary nodes for the numerical resolution of the NSWE. This approach is consistent with the numerical framework, since the imposition of said quantities is equivalent to imposing the boundary values of the Riemann invariants propagating along the characteristics curves of the NSWEs. The input conditions of fluid velocity and water level act as initial values for the Riemann problems defined at the borders of the domain.

The solver as it was first conceived could only simulate processes where waves alone are involved: wave propagation, wave transformation in shallow waters, swash and shoreline motions, flow circulation in the nearshore, and their respective morphological implications. In order to make the solver able to reproduce the more complex flow configurations typical of estuarine environments, where the incoming wave forcing and the effects of tides are bound to interact with river currents, the solver had to be integrated with a suitable estuary model. In this section the main features of our simple estuary model are described.

The user can define a window of "estuary nodes" within the landward edge of the computational grid, through which the input river forcing can enter the domain. The estuary window is unambiguously defined by the  $y$ -coordinate of its center,  $y_{m,e}$  (the estuary center  $x$ -coordinate,  $x_{m,e}$ , being automatically assumed as the  $x$ -coordinate of the landward domain boundary), and its centered width  $L_e$ . The spatial limits of the estuary window are therefore

$$y_{min,e} = y_{m,e} - \frac{L_e}{2}, \quad y_{max,e} = y_{m,e} + \frac{L_e}{2}. \quad (2.48)$$

The mesh nodes at the landward domain boundary falling between  $y_{min,e}$  and  $y_{max,e}$  are ultimately labeled as "estuary nodes". At these nodes, in a similar way to how a wave input is imposed at the seaward edge, a time history of current velocity and/or water level elevation is prescribed to simulate the entrance of river discharges into the basin at variable angles of incidence with respect to the  $x$ -direction. The numerical procedure adopted to attain this is briefly explained in the following.

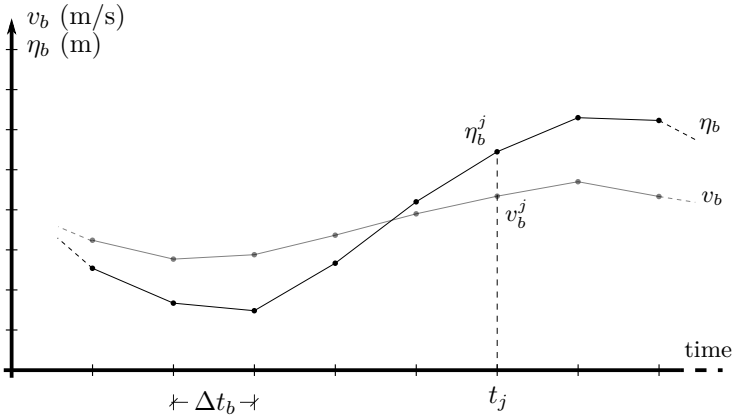


Figure 2.8: Example of a generic time history for the values of fluid velocity  $v_b$  and water elevation  $\eta_b$ . At the time instant  $t_j$  correspond prescribed values  $v_b^j$  and  $\eta_b^j$  to be imposed at the boundary nodes.

As stated earlier, the estuarine input is furnished as a time history for the fluid velocity  $v_b$  and water elevation  $\eta_b$ . An example of such a time history is presented in Figure 2.8. The values composing the time history are equally spaced in time by a constant interval  $\Delta t_b$ , which need not be equal to the time step determined by the solver as the computation goes on (which, besides, cannot be known beforehand since it is automatically evaluated to satisfy the CFL stability condition and, in principle, varies at each step). To encompass different real situations, the estuarine input is allowed to enter at different angles with respect to the basin: if this is the case, the oblique propagation front involves the boundary nodes at different times. To allow for the propagation of the estuary input at a variable angle of incidence, a simple numerical procedure has been developed, which will be briefly explained in the following section.

Whenever an estuarine input is considered, two distinct cases may occur: the input may enter the domain perpendicularly to the boundary edge (i.e. at an angle of incidence  $\theta = 0$  with respect to the outer-pointing normal to the edge), or may enter the domain obliquely (i.e. at an angle of incidence  $\theta \neq 0$ ). Albeit the numerical treatment for the first scenario can be assumed as a special case of the procedure adopted for the second scenario, we will treat the two cases separately for the sake of clarity.

**Case I: estuary input perpendicular to the border ( $\theta = 0$ ).** In this case, the estuary input described by the time history enters the domain in a perpendicular fashion through the estuary window. As a consequence of this, all the nodes falling into the estuary window "read" the same boundary conditions from the time history simultaneously since are "touched" by the input signal at

the same time.

As said previously, the estuarine boundary conditions (in terms of imposed fluid velocity  $v_b$  and water elevation  $\eta_b$ ) are sampled at a constant interval  $\Delta t_b$  that *a priori* is not the same as the solver-defined, variable time interval  $\Delta t$ ; therefore, it is highly likely that the current solution time level  $t_i$  falls between two consecutive time instants  $t_k$  and  $t_{k+1}$  in the estuary input time series, so that  $t_k \leq t_i \leq t_{k+1}$ . Then the exact values of fluid elevation  $\eta_b^i$  and velocity  $v_b^i$  to impose at the estuary nodes are obtained through linear interpolation between the boundary condition values at times  $t_k$  and  $t_{k+1}$ . For the two quantities separately, this reads:

$$\eta_b^i = \eta_b^k + (\eta_b^{k+1} - \eta_b^k) \frac{t_i - t_k}{t_{k+1} - t_k} \quad (2.49)$$

and

$$v_b^i = v_b^k + (v_b^{k+1} - v_b^k) \frac{t_i - t_k}{t_{k+1} - t_k}, \quad (2.50)$$

where  $\eta_b^k$  and  $v_b^k$  are the prescribed boundary values for fluid elevation and velocity for time  $t_k$ , and  $\eta_b^{k+1}$  and  $v_b^{k+1}$  are the same boundary values for time  $t_{k+1}$ . The extrapolated values  $\eta_b^i$  and  $v_b^i$ , finally, are imposed at all the estuary nodes by adding them to the existing values of water depth and velocity. Since the estuary input is perpendicular to the normal to the domain edge, the estuary input velocity  $v_b$  is already oriented in the  $x$ -direction and has no  $y$ -component. So only the water depth and the  $x$ -component of the fluid velocity are modified by the same amounts for all the estuary nodes and carried on to the next solution step,  $t_{i+1} = t_i + \Delta t$ . Hence, for the generic estuary node,

$$d^{i+1} = d^i + \eta_b^i \quad \text{and} \quad u^{i+1} = u^i + v_b^i. \quad (2.51)$$

**Case II:** *estuary input oblique with respect to the border* ( $\theta \neq 0$ ). In this case, since the input estuary front are propagating obliquely, the estuary nodes are "touched" by a single boundary condition value at different times according to the signal propagation velocity. In other terms, at a fixed solution time  $t_i$ , different estuary nodes "read" different boundary values from the input time history. Moreover, the input fluid velocity  $v_b$  (whose name will be hereinafter changed into  $w_b$  in order to avoid confusion with the  $y$ -directed fluid velocity  $v$ ) is now oriented at an angle with respect to the  $x$ -direction, and thus can be decomposed into an  $x$ -component and an  $y$ -component. Each of the two components will alter the corresponding nodal velocities as effect of the estuarine boundary condition. The case of an oblique estuary input is exemplified by the scheme in Figure 2.9.

Since each estuary node "reads" different boundary values of water eleva-

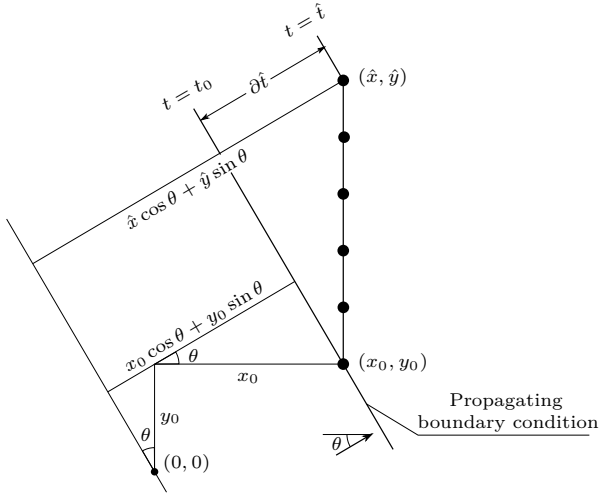


Figure 2.9: Geometrical scheme for the case of an estuary boundary condition entering the domain at an angle  $\theta$ . A single boundary condition is read by node  $(x_0, y_0)$  at time  $t_0$ , and reaches node  $(\hat{x}, \hat{y})$  at time  $\hat{t} = t_0 + \partial\hat{t}$

tion  $\eta_b$  and velocity  $w_b$  at the same solution time, a key problem that must be addressed now is to understand which boundary values each node "read", and how to compute them from the input time history. This is done by assuming that the estuarine input propagates (as every signal in shallow waters does) according to the characteristic propagation speed or celerity, defined as  $\sqrt{gd}$ , where  $d$  is the water depth. To have a grasp of this concept, let  $(x_0, y_0)$  be the coordinates of the first estuary node interested by the estuary input (the "first contact" node hereinafter), and  $(x, y)$  the coordinates of another estuary node different from the first. At the very start of the numerical simulation (solution time level  $t_i = 0$ ), the estuary input will interest only the "first contact" node  $(x_0, y_0)$ ; at subsequent times (solution time level  $t_{i+1} = t_i + \Delta t > 0$ ), the very same conditions that only interested the "first contact" node will have traveled into the domain (along the direction defined by the angle  $\theta$ ) and perhaps interested other nodes  $(x, y)$  within the estuary window. We can approximately evaluate the time  $\partial\hat{t}$  that a boundary condition value would take to travel from the "first contact" node  $(x_0, y_0)$  to any other estuary node  $(\hat{x}, \hat{y})$  with the following formula:

$$\partial\hat{t}(\hat{x}, \hat{y}) = \frac{(\hat{x} \cos \theta + \hat{y} \sin \theta) - (x_0 \cos \theta + y_0 \sin \theta)}{\sqrt{gd_0}}. \quad (2.52)$$

The quantity appearing at the numerator in (2.52) represents the linear

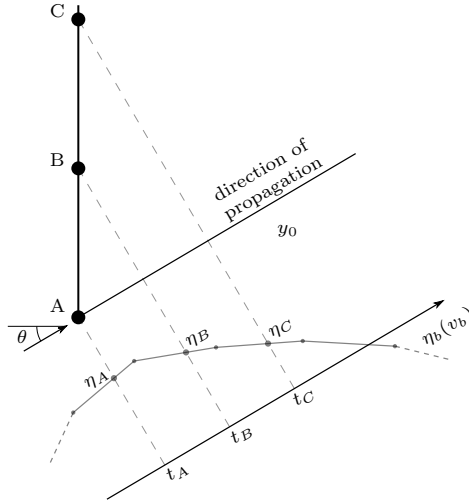


Figure 2.10: Scheme for the evaluation of the boundary conditions at each estuary node.

distance between the generic estuary node  $(\hat{x}, \hat{y})$  and the "first contact" node  $(x_0, y_0)$ , evaluated along the direction defined by  $\theta$ , i.e. the direction of propagation of the estuary input; this is, in fact, the "space" covered by the traveling boundary condition. The denominator in (2.52) expresses the celerity of the estuary input signal, approximately evaluated using  $d_0$ , the water depth at the "first contact" node.

We are now able to find out, for a specific solution time level, which boundary conditions  $\eta_b$  and  $w_b$  each estuary node "reads" from the time history and carries on to the next computational step. Reference to Figure 2.10 will be made in the next explanation. At a generic solution time  $t_i > 0$ , the "first contact" node  $A$  reads the boundary condition for the water elevation  $\eta_A$  (and, similarly, the boundary condition for the fluid velocity  $w_A$  not reported in the figure). At the very same time  $t_i$ , node  $B$ , which is temporally ahead of  $A$  by a time  $\partial t_{AB}$  which is evaluated by means of equation (2.52) with  $(\hat{x}, \hat{y}) = (x_A, y_A)$ , reads boundary condition  $\eta_B$ . In the same way, node  $C$  is temporally ahead of  $A$  by a time  $\partial t_{AC}$  and reads boundary condition  $\eta_C$ .

So, if  $t_A$  is the time instant at which the boundary conditions for node  $A$  are evaluated from the input time history, the evaluation times  $t_B$  and  $t_C$  for nodes  $B$  and  $C$  respectively are readily computed as:

$$\begin{aligned} t_B &= t_A - \partial t_{AB} \\ &= t_A - \frac{(x_B \cos \theta + y_B \sin \theta) - (x_A \cos \theta + y_A \sin \theta)}{\sqrt{gd_0}}, \end{aligned} \quad (2.53)$$

$$\begin{aligned} t_C &= t_A - \partial t_{AC} \\ &= t_A - \frac{(x_C \cos \theta + y_C \sin \theta) - (x_A \cos \theta + y_A \sin \theta)}{\sqrt{gd_0}}. \end{aligned} \quad (2.54)$$

The minus sign appearing in relations (2.53-2.54) is due to the fact that, in the boundary condition time history graphically represented in Figure 2.8, the direction of increasing time values is leftward: the boundary values at the right side of the picture are defined for earlier times, whereas the values at the left side are attributed to the boundary nodes at later times. With reference to Figure 2.10, this implies that  $t_C < t_B < t_A$ , in absolute value. On intuitive grounds, we can say that a specific estuary node "scans" the entire time history from the earlier times to the later times: at the solution time in which node  $A$  reads  $\eta_A$ , node  $B$  reads a condition  $\eta_B$  that has been already reached and trespassed the position of node  $A$ ; thus, condition  $\eta_B$  is referred to a earlier time than  $\eta_A$ . The same stands for node  $C$ , which reads a condition  $\eta_C$  that has already trespassed nodes  $A$  and  $B$ .

As it has been done for Case I, since the evaluation times  $t_A$ ,  $t_B$ , and  $t_C$  most likely fall between two consecutive user-defined time levels in the time history (see Figure 2.10), the exact values to be imposed at each node can be obtained by linear interpolation between the two adjacent boundary condition values, by use of relations (2.49-2.50). Once each estuary node has read the proper (interpolated) boundary conditions for both water level  $\eta_b^i$  and fluid velocity  $w_b^i$ , these values alter the water depth,  $x$ -velocity and  $y$ -velocity for the estuary nodes, and the altered values are carried on to the next solution step:

$$\begin{aligned} d^{i+1} &= d^i + \eta_b^i, \\ u^{i+1} &= u^i + w_b^i \cos \theta, \\ v^{i+1} &= v^i + w_b^i \sin \theta, \end{aligned} \quad (2.55)$$

where  $d^i$ ,  $u^i$  and  $v^i$  are the water depth, the  $x$ -directed and the  $y$ -directed components of the depth-averaged fluid velocity of the specific estuary node at solution time level  $i$ , respectively.

It can be easily seen that Case II is, in fact, a generalization of Case I for estuary inputs entering the computational domain at angles different than  $\theta = 0$ . As a matter of fact, since  $\theta = 0$  means that  $\cos \theta = 1$  and  $\sin \theta = 0$ , relation (2.52) in the case of a perpendicular input reduces to

$$\partial \hat{t}(\hat{x}, \hat{y}) = \frac{\hat{x} - x_0}{\sqrt{gd_0}}. \quad (2.56)$$

Considering that, within the estuary window, all estuary nodes  $(\hat{x}, \hat{y})$  share the same  $x$ -coordinate with the "first contact" node  $(x_0, y_0)$  (this coordinate being, precisely, the  $x$ -coordinate of the landward edge of the computational domain),  $\hat{x} = x_0$  and, therefore,  $\partial \hat{t} = 0$  for all estuary nodes. This means that there are no "delay times" among estuary nodes due to an oblique direction of propagation, and each node sample the exact same boundary condition at the same solution time. The numerical procedure above explained for Case II can, thus, be also applied to Case I without any loss of generality.

### 2.4.5 Mesh generation

In the original version of the NSW solver, the creation of the computational meshes that serve as the numerical support for the simulations is down to an *ad hoc* mesh generator (or mesher hereinafter) called MESH2D. The input of MESH2D is a formatted text file containing the cartesian description of a number of bathymetry transects in the cross-shore direction, as well as other data like the domain dimensions and grid sizes in both coordinate directions,  $x$  and  $y$ . The result of the mesh generator, thus, is a numerical structured grid of equally-spaced nodes. If increased resolution of the numerical solution is needed, one can also impose a mesh refinement landward of a prescribed cross-shore coordinate. MESH2D is then able to generate a bathymetry over the whole domain by performing a simple linear interpolation of the input transects in the  $y$ -direction and gives as output an unformatted mesh descriptor, which in turn serves as input for the numerical solver. Notwithstanding its simplicity and robustness, since the generation process is based on the definition of cross-shore transects, MESH2D can produce only meshes with very simple bathymetries and limited variations in the longshore direction.

In view of dealing with flows over more complex morphology in real case scenarios, such as in the tests for the Misa River mouth described in section 4.3, the necessity of representing the bathymetry and planar configuration of a real estuary and the surrounding nearshore areas with a sufficient degree of accuracy has thus arisen. The aforementioned limitations has been answered with the development of a new mesher, which is capable of generating accurate structured meshes with rectangular grids for use in 2-dimensional numerical solvers. This section is dedicated to a brief description of the mesh construction process implemented in the new mesher.

The starting point is a scattered dataset given as a list of possibly georeferenced  $(x, y, z)$  coordinates of points derived from a bathymetric survey: these points, in essence, form a data cloud that represent the bottom surface of the zone of interest. The point cloud can be either equally spaced or random, and is allowed to have "holes", i.e. regions where no bathymetric points are defined,

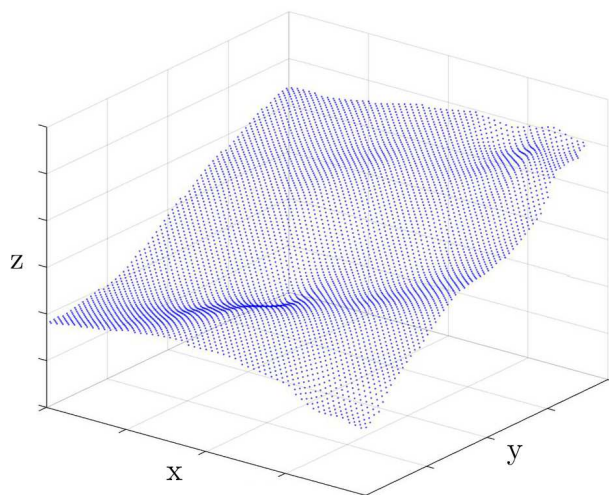


Figure 2.11: Example of a data cloud serving as a base for the mesh generation. Each blue dot represents a point of the surveyed bathymetry in a cartesian georeferenced system of coordinates.

like emerged zones and coastal manufacts not included in the survey. An example of point cloud is given in Figure 2.11, where a limited set of data points from a topographic survey of the nearshore zone at the Misa River estuary in Senigallia, Italy is presented.

The first step undertaken by the mesher is a rigid rotation of the point cloud, so that the underlying bathymetry is oriented according to the needs of the intended simulation. In the case of a simulation including both marine and estuarine forcings, for example, one may need to rotate the data cloud in a way that the marine boundary is placed at the left side of the region (looking at the bathymetry from above), whereas the estuary mouth is placed at the opposite side. This is simply accomplished by rotating the cloud by a user-defined angle with respect to an axis parallel to the  $z$  direction. Afterwards, the user is called to define the coordinates of the four borders of the rectangular domain in which the computation will take place: namely,  $x_{min}$ ,  $x_{max}$ ,  $y_{min}$  and  $y_{max}$ . The original dataset is then "trimmed" to extract only the points that fall within the desired domain limits: this is made to rule out unnecessary points and hence lower the computational costs of the upcoming processes. wevre

Up to this point, the data cloud has been reduced to a limited number of points covering the rectangular area of interest, like in the example provided in Figure 2.11. Our objective is to interpolate these points into a 3-dimensional surface, which will represent the numerical bathymetry to be used in the simu-

lations. The interpolating surface will be defined over a 2-dimensional regular support grid of points  $(x_g, y_g)$ . To any single point of the support grid, a value of  $z_g$  will be given so that the resulting surface will resemble the topographic structure of the surveyed bathymetry in the best way possible. The resulting 3-dimensional mesh will be therefore composed of points  $(x_g, y_g, z_g)$  equally spaced in both the  $x$ - and  $y$ -directions, with spatial resolutions  $\Delta x$  and  $\Delta y$  definable by the user. Clearly, since the data cloud from the bathymetric survey is allowed to be randomic — although in common practice hydrographic survey are usually performed along lines orthogonal to the beach and therefore have a somewhat regular structure themselves — and, moreover, is preliminarily rotated by an arbitrary angle, the nodes of the support grid  $(x_g, y_g)$  are not likely to have the exact same  $(x, y)$  coordinates of any survey point. In such a case, the elevation value  $z_g$  at the grid point  $(x_g, y_g)$  will be evaluated through interpolation between the elevation values of the closest survey points.

A necessary base for the interpolation of the scattered survey data sample over the support grid is guaranteed by first creating a planar Delaunay tessellation of the survey data [122]. In a Delaunay tessellation the survey points are projected onto the  $(x, y)$ -plane and connected to subdivide the plane into triangles. There are obviously many ways to connect random points in a triangular mesh: the Delaunay tessellation, though, is notable in that, in the resulting triangulation, the minimum angles of all the triangles is maximized, and all the triangles are close to be equilateral. This hinders the generation of undesirable sliver triangles, i.e. excessively thin and ill-formed triangles that may cause several inaccuracies in the upcoming interpolating process.

After the preliminary triangulation, the interpolating process can be finally performed. In the new mesher the natural neighbor interpolating method [123, 124] is incorporated: this method has been chosen since it provides a smoother representation of the underlying surveyed bathymetry. A surface interpolated by means of the natural neighbor method, in fact, is at least of class  $C^1$  (i.e. it is differentiable anywhere with continuous derivatives) at any point, except at the sample nodes, in which the derivatives are discontinuous [125]. In the surface interpolated by this method, the change in bottom elevation between consecutive support grid points, i.e. the bathymetry bottom gradient, is the most gentle possible: so, abrupt changes in bathymetry are limited to the minimum. The so-created mesh, thus, has the best features for the specific needs of our numerical solver, which is sensible to sharp bottom gradients. In addition, should the smoothness achieved in the standard interpolation not be enough, a further smoothing filter is implemented: for this purpose, a Savitzky-Golay low-pass filter [126, 127] with a moving window whose width is freely user-defined has been implemented. This filter is usually successful in removing high-frequency components in signals whose range in frequency is large, i.e. can

be decomposed into signals with a wide range of frequencies. In the context of a surface representing a real bathymetry, this means that the filter is capable of suppressing the high-frequency noise (mainly due to the numerical generation of the mesh) whilst maintaining the low as well as the high frequency features of the bathymetry intact.

Up to this point we have a smooth surface interpolating the survey point cloud into the desired computational planar domain. This surface, built over a support grid  $(x_g, y_g)$ , represents in the best way the existing bathymetric topography of the nearshore area of interest for the intended simulations. However, it may occur that the real study domain includes impermeable structures or emerged coastal artefacts that have been excluded from the bathymetric survey campaign. These physical regions appear as "holes" in the point cloud and no computation should be performed there; nevertheless the mesher may generate a fictitious bathymetry also within the holes if they are placed in the interior of the data cloud convex hull. The portions of the bathymetry (i.e. of the interpolated mesh) falling into the holes must thus be appropriately ruled out from the "active" mesh where the actual computations will take place. To identify which points to exclude from the interpolated mesh, a simple procedure based on geometric reasonings has been devised. In summary, the exclusion process takes out from the active mesh all the points  $\mathbf{p}_g = (x_g, y_g, z_g)$  whose 3-dimensional Euclidean distance from the closest cloud point  $\mathbf{p} = (x, y, z)$  is lower than a predefined threshold  $\hat{d}$ :

$$d(\mathbf{p}_g, \mathbf{p}) = \sqrt{(x_g - x)^2 + (y_g - y)^2 + (z_g - z)^2} < \hat{d} \quad (2.57)$$

Particular care must be put into the definition of the exclusion threshold,  $\hat{d}$ . One may be tempted to adopt extremely low threshold values in order to obtain a refined mesh with borders that are true to reality. However, too low threshold values would also eliminate mesh points that are completely surrounded by points from the data cloud, and therefore are part of the active mesh. This happens in particular when a relatively sparse point cloud is being interpolated by a mesh with a much finer resolution. In the light of this shortcoming, generating meshes at a resolution much lower than the resolution of the bathymetric survey is not advisable since further work on the matter is needed. For the meshes employed in the simulations whose results are discussed in this thesis, the best performance has been achieved by setting the threshold  $\hat{d}$  equal to the diagonal of the mesh cell,  $\sqrt{(\Delta x)^2 + (\Delta y)^2}$ , or slightly less than this value.

Once all the extraneous mesh points have been identified, their exclusion is not performed by straightforwardly deleting it, for example by substituting them with a NaN structure, since our numerical solver does not tolerate meshes

with ill-defined points. The mesh node is instead retained, but labelled as "inactive", so that no effective computation will be made on it when the solver is run.

Before formatting it in a form suitable for the numerical solver, the generated mesh must be completed with other significant parameters. Each mesh point, defined by its cartesian coordinates  $(x_g, y_g, z_g)$ , will be then equipped with other significant parameters, such as the depth of the fixed bed for use in morphodynamic simulations, the prescribed Chezy coefficient, the height of the initial water column, and in case they are needed to model particular conditions, also starting values for the horizontal depth-averaged velocities  $(u, v)$  and the water surface elevation  $\eta$ .



# Chapter 3

## Numerical tests

In estuarine environments, where a river stream coming from the inland connects to the open sea, or near tidal inlets, where the wave action is modulated by the ebb and flood tidal phases, the complex interplay that is bound to occur between gravity waves and opposing currents certainly have a relevant role in shaping the nearshore. Likewise, both outflowing currents and approaching waves are affected by the bathymetry which, for example, may force breaking and dissipation of wave energy in specific areas, determining the morphological evolution of the seabed in the medium and long term. Numerical models that are able to consider and resolve the complicated hydro-morphodynamic features resulting from these scenarios, therefore, can be effectively exploited to predict the flow structure in estuaries, river mouths, and other inlets.

To evaluate the performance of our NSW solver, enhanced with the modifications described in sections 2.4.4 and 2.4.5 in order to take account of the processes induced by a discharging current as well as the increased morphological complexity of real-case estuarine regions, two distinct campaigns of numerical simulations have been performed. First, a series of numerical hydro-morphodynamic trials in a simplified inlet configuration has been run. These tests, made in similarity with those described by Olabarrieta et al. [2], aim at investigating the wave-current interaction flows taking place in an idealized inlet of varied morphology. Our observations focused on the flow and sedimentary patterns emerging from waves and currents of various energy, as well as on the generation and evolution of vortical structures.

Afterwards, our solver has been used in an attempt to reproduce the sediment dynamics occurring at the mouth of the Misa River, located in the microtidal coast of Senigallia, Italy. The results will be compared to the main findings of a number of recent works focused on the morphological evolution of the coastal areas nearby the Misa River mouth.

A brief description of model setups and methodologies adopted for both numerical campaigns is presented in this chapter.

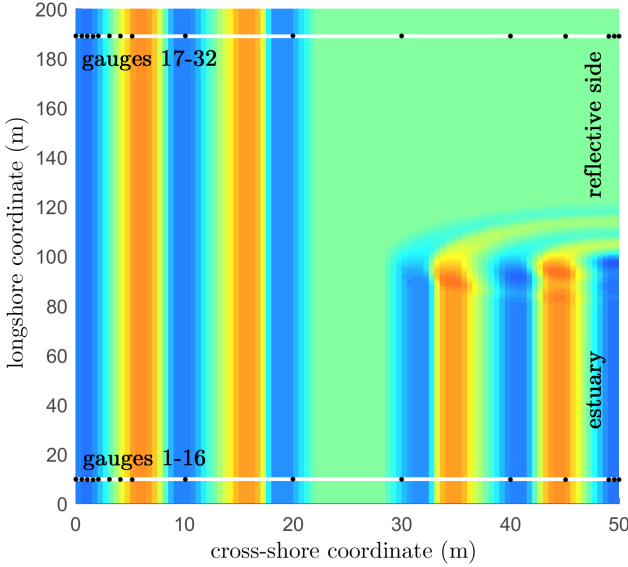


Figure 3.1: Plain view of the basin for the preliminary test. The figure shows both the seaward waves (entering from the left side) and the landward waves (entering from the estuary window on the right side). The black dots represent the gauges locations.

### 3.1 A simple wave propagation test

Before proceeding with the actual tests, a preliminary numerical simulation has been run to check the performance of the newly-developed estuary model against a simple test case.

In this simulation, two wave trains enter from the opposite sides of a rectangular basin 50 m long and 200 m wide, with a constant water depth of 1 m. The seaward (left) side of the domain is completely permeable to the incoming waves; on the other hand, the landward (right) boundary is divided into two portions: an estuary window through which waves enter the domain ( $y = 0 - 100$  m), and a reflective side at which waves are totally reflected ( $y = 100 - 200$  m). The estuarine window has been created by means of the procedure described in section 2.4.4, with  $y_{m,e} = 50$  m and  $L_e = 100$  m. Both the seaward and the landward wave trains have the same characteristics: a height  $H = 0.1$  m, and a period  $T = 3$  s.

To observe the variations of the free surface, two groups of wave gauges have been deployed throughout the computational domain, along two longitudinal axes. The gauges from 1 to 16 are placed at  $y = 10$  m. They are labelled "estuary side" gauges and are meant to observe the interactions of the seaward and the landward waves in the part of the basin that is characterized by the

presence of the estuary window. The gauges from 17 to 32 (the "reflective side" gauges), conversely, are placed at  $y = 190$  m in order to check the reflective properties of the closed landward boundary.

A plain view of the rectangular basin and the gauges locations is shown in Figure 3.1.

## 3.2 Wave-current interaction on a simplified inlet

The wave-current interaction tests presented in the work by Olabarrieta et al. [2] aimed at assessing the physical processes involved in the interaction between currents, gravity waves, and bathymetry in inlets. The flow structures resulting from this configuration can be representative of ebb-tidal currents interacting with gravity waves at barrier tidal inlets in meso-macrotidal coastlines, as well as riverine discharges in microtidal coasts. The study took into consideration the presence or absence of a well formed ebb shoal (a feature commonly found in most natural inlet systems) and analyzed its influence on the global hydrodynamics. The morphology selected for the simulations is a simplified representation of the New River inlet (North Carolina), whose real bathymetry features a clearly identifiable ebb shoal region that changes its shape and volume in time.

The simple shoal configuration we adopted for our simulations has been made in strict resemblance with the one conceived by Olabarrieta et al. (top panel of Figure 3.2). The inlet area is characterized by a main channel about 300 m wide and 5 m deep at the central axis, which opens to a semicircular, symmetric ebb shoal zone of minimum depth 2 m, that extends 1 km offshore of the inlet mouth. The main channel also crosses the shoal and connects the inlet to the offshore area. The beach exhibits a Dean equilibrium profile given by the expression:

$$d = Ax^{2/3} \quad (3.1)$$

where  $d$  is the water depth,  $x$  is the cross-shore distance, measured offshore from the mouth, and the profile scale factor  $A$  is set equal to 0.05 in agreement with the numerical setup by Olabarrieta et al. The computational domain for our simulations is 3 km long in both cross-shore and alongshore directions, and has been discretized into a computational mesh with node spacings  $\Delta x = 10$  m and  $\Delta y = 20$  m in the  $x$  and  $y$  direction respectively. The resulting mesh has been generated via the novel mesher described in section 2.4.5 and can be seen in the bottom panel of Figure 3.2.

The bed friction coefficient  $c_r$  assigned to each mesh node is computed as a function of the initial water depth, using the formulation proposed by van

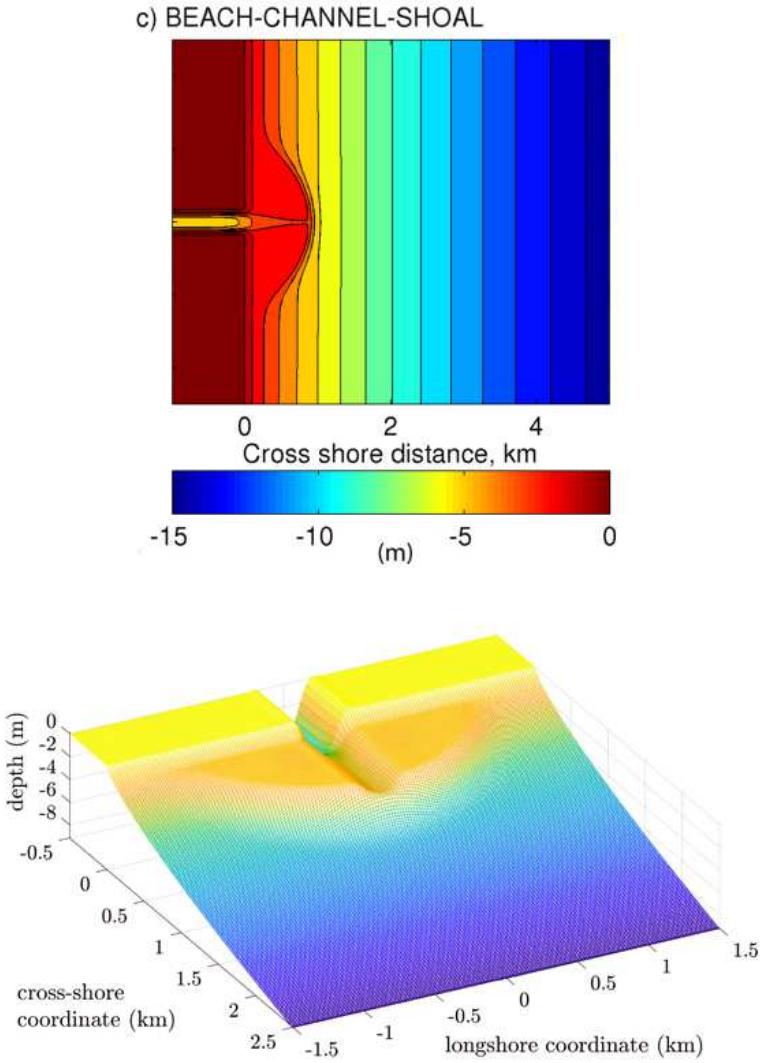


Figure 3.2: Sketches of a shoal bathymetry. *Top panel*: plan view of the idealized configuration of an inlet mouth with shoal used in the tests by Olabarrieta et al., 2014. The colorbar refers to the depth with respect to the still water level. *Bottom panel*: 3-dimensional view of the shoal bathymetry used in our simulations.

### 3.2 Wave-current interaction on a simplified inlet

Rijn [128] in case of a hydraulically rough flow:

$$c_\tau = \frac{g}{\left(18 \log \frac{12d}{k_s}\right)^2} \quad (3.2)$$

where the bed roughness  $k_s$ , in agreement with Olabarrieta et al., is set equal to  $2 \cdot 10^{-4}$  m. For all tests the increase in apparent bed roughness and friction coefficient due to waves has not been considered.

A suite of simulations with variable wave conditions and outflowing current speeds, relative to different outflow rates, has been performed over the shoal bathymetry shown in Figure 3.2 in order to explore the full spectrum of wave-current interactions and investigate the hydrodynamic and morphological features of the resulting flows. In particular, three wave conditions (no waves, weak wave regime, and strong wave regime) and three current velocities ( $u_c = 0.6, 1.1,$  and  $1.6$  m/s, roughly resulting in outflow rates of 325, 750, and 1500  $\text{m}^3/\text{s}$  respectively) have been considered, giving a total of nine different test setups. In each test, a riverine input and a wave input are free to propagate over the shoal bathymetry. The river input enters the domain from the inlet mouth, at a cross-shore coordinate  $x = -0.5$  km, whereas the wave input comes from the seaward boundary of the domain, at a cross-shore coordinate  $x = 2.5$  km.

The three wave conditions imposed at the seaward boundary of the domain have been randomly generated from a simplified version of the single peak JONSWAP spectrum, firstly proposed by Hasselmann et al. [129]. In its original form, the parameters of the spectrum were coupled with various data like the wind speed and the length of the fetch, making its forecasting capability trustworthy albeit very complex; nonetheless, for simplicity's sake the spectrum can be rewritten in an approximate form where the only parameters involved are the significant wave height  $H_s$  (traditionally defined as the mean wave height of the highest third of the waves in a given sea state) and the peak wave period  $T_p$ . The approximate form of the JONSWAP spectrum reads [130]:

$$S(f) = \beta \frac{H_s^2}{T_p^4 f^5} \exp\left[-\frac{5}{4} \frac{1}{T_p f}\right] \gamma^{\exp\left[-\frac{(T_p f - 1)^2}{2\sigma^2}\right]} \quad (3.3)$$

where

$$\beta = \frac{0.0624 [1.094 - 0.01915 \ln \gamma]}{0.23 + 0.0336\gamma - 0.185 (1.9 + \gamma)^{-1}} \quad \text{and} \quad \sigma = \begin{cases} 0.07 & \text{if } f \leq f_p, \\ 0.09 & \text{if } f > f_p. \end{cases}$$

The peak enhancement factor  $\gamma$ , which usually ranges between 1 and 7, has been assigned a value of 3.3, the standard mean value determined for the

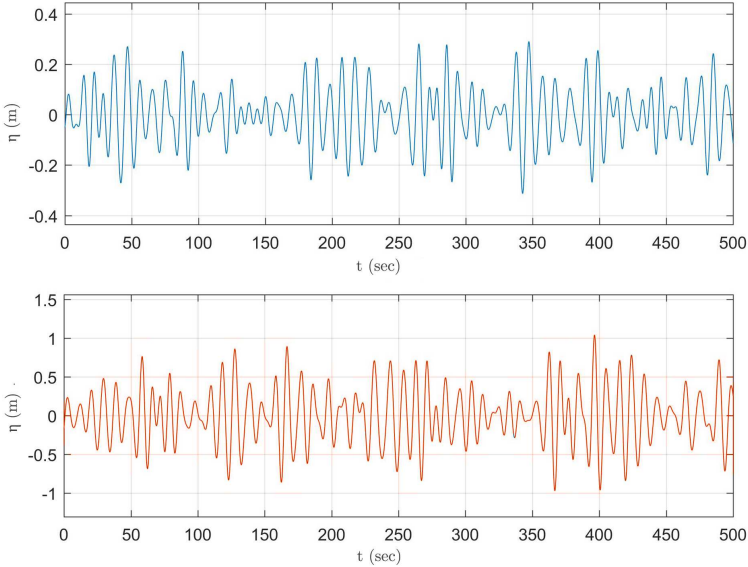


Figure 3.3: Samples of the wave series generated through the single peak JON-SWAP spectrum (3.3) for the wave-current interaction tests. *Top panel*: weak wave condition ( $H_s = 0.5$  m,  $T_p = 10$  seconds). *Bottom panel*: strong wave condition ( $H_s = 1.5$  m,  $T_p = 10$  seconds).

North Sea.  $f$ , the independent variable of the spectrum, is the wave frequency in Hz;  $f_p$  is the frequency at the peak of the spectrum, related to the peak period  $T_p$  by the relationship  $f_p = T_p^{-1}$ .

Besides the obvious condition of no waves ( $H_s = 0$  m), two different wave states have been defined for use in the wave-current interaction simulations: the weak wave regime and the strong wave regime. The weak wave regime is characterized by a significant wave height  $H_s = 0.5$  m, whereas the strong wave regime is characterized by  $H_s = 1.5$  m. For both wave regimes, the spectral peak period  $T_p$  is set to 10 seconds. Samples of the wave input generated by means of the JONSWAP spectrum for both wave conditions are presented in Figure 3.3.

The river current velocities have been imposed at the landward edge of the computational domain, where the inlet mouth is located, by means of the estuarine model input described in section 2.4.4. Absorbent boundary conditions are prescribed at the lateral edges of the domain to simulate transparent borders.

A summary of the wave and current conditions and the relative test names is presented in Table 3.1.

### 3.3 Estuarine morphodynamics at the Misa River mouth

Our solver has been also applied to simulate the circulation and morphodynamic patterns emerging at the mouth of the canalized Misa River and the nearshore area in front of the estuary.

The Misa River originates in the eastern side of the "Appennino umbromarchigiano" in Central Italy and runs for around 48 km before joining the Adriatic Sea in the municipality of Senigallia, Marche. The most downstream part of the river, crossing the city of Senigallia, is heavily engineered, the final reach being channeled by cement walls and jetties. From an hydrological viewpoint, the coastal regime of the Misa River mouth can be classified as microtidal. Moreover, the Misa River estuary is a characteristic example of a salt wedge estuary, where the river stream expands seaward with a layer of fresh water over salt water. This occurs when the river discharge is enough to keep a strong gradient between freshwater and seawater, winning the mixing forces of waves and tides [30, 131]. These conditions makes it an excellent environment to assess the interaction between the river outflow and the nearshore hydrodynamics and the resulting morphological evolution.

The bathymetry used for the numerical simulations has been generated with the novel mesher described in section 2.4.5, starting from a dataset of georeferenced points describing the actual riverbed configuration of the Misa River estuary and the nearby regions. The mesh is presented in Figure 3.4: the top panel shows a plan view of the area surrounding the river mouth, while the bottom panel presents a 3-dimensional view. The bathymetry covers only the areas where actual numerical computation will take place. Emerged zones like the "Banchina di ponente" and "Banchina di levante" (the jetties delimiting the most downstream part of the river), as well as the port docks originally located at the bottom right corner of the mesh in plan view (see the top panel in Figure 3.4) have been ruled out of the computational mesh and labelled as no flow areas. The area of investigation spans 500 m in the cross-shore

Table 3.1: Summary of the wave-current interaction tests.

Wave condition ( $T_p = 10$ s)	Velocity (m/s)		
	0.6	1.1	1.6
No wave	T1	T2	T3
Weak ( $H_s = 0.5$ m)	T4	T5	T6
Strong ( $H_s = 1.5$ m)	T7	T8	T9

direction (from roughly 150 m offshore from the estuary mouth to the emerged beaches near the "Banchina di levante") and 400 m in the longshore direction. In both panels of Figure 3.4 is clearly visible the mesh strip representing the most downstream reach of the Misa River, through which the estuary outflow reaches the open sea. The estuary input is applied at the estuarine boundary nodes located at the landward side of the domain (the right edge in the top panel of Figure 3.4), between 250 and 300 m in the longshore direction.

In the Misa River mouth test, a wave train and a river current are free to propagate into the domain and interact. The wave input enters perpendicularly to the seaward domain boundary (the left edge in the top panel of Figure 3.4) and is generated through the JONSWAP spectrum of equation (3.3). In order to simulate a moderately intense sea state, and to allow for a significant amount of the wave energy to reach the region close to the shoreline, a significant wave height  $H_s = 1.5$  m and peak period  $T_p = 20$  seconds have been chosen as input parameters for the spectrum.

The grid spacings are  $\Delta x = 2$  m and  $\Delta y = 4$  m. Bed friction values depending on the starting water depth have been given to each mesh node following the formulation (3.2). The mean size of the sediment that constitutes the bottom surface is  $d_{50} = 0.5$  mm, corresponding to medium-to-coarse sand.

### 3.3 Estuarine morphodynamics at the Misa River mouth

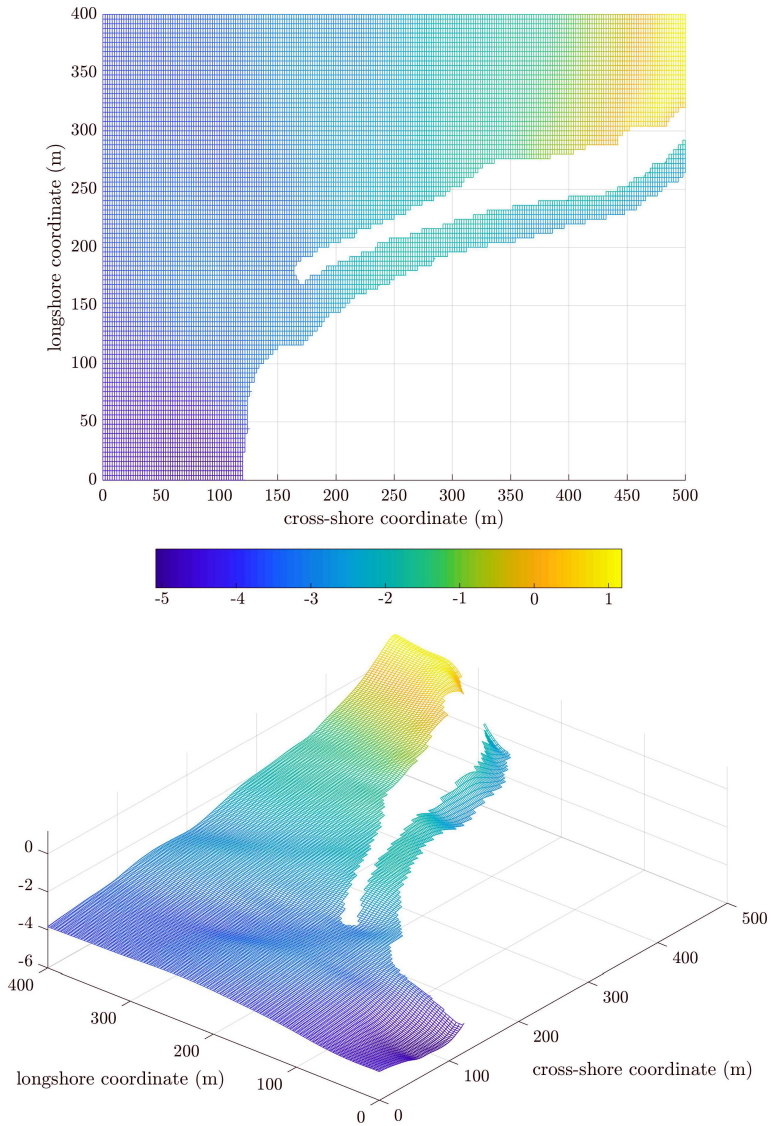


Figure 3.4: Sketches of the mesh employed for the morphodynamics tests at the Misa River mouth. *Top panel:* plan view. *Bottom panel:* 3-dimensional view.



# Chapter 4

## Results and discussion

This chapter is devoted to analyze and discuss the results of the numerical tests described in Chapter 3 and carried out with the aid of the solver for shallow waters described in Chapter 2. Beforehand, the salient results of the simple wave propagation test described in section 3.1 are discussed.

### 4.1 A simple wave propagation test

Figure 4.1 shows time series of the water level for three gauges located at the estuary side of the basin, between  $y = 0$  m and  $y = 100$  m. Gauge 1 ( $x = 0$  m) is located exactly at the seaward boundary of the domain and detects the incoming wave train. Gauges 11 and 12, at  $x = 30$  m and  $x = 40$  m, respectively, are located in the interior part of the estuary side, where the waves from both the sea and the estuary window interact.

The time series from gauge 12 ( $x = 40$  m; blue line in Figure 4.1) shows all the main features of the wave propagation and interaction within the analyzed basin. Since this gauge is closer to the estuary window than to the seaward boundary, the wave train from the estuary is detected first (see the blue line, at  $t > 3$  s), with the sea wave train reaching the gauge location three wave periods after the estuary waves, at around  $t = 12$  s. After this time, the elevation time series detected by the gauge shows that the two wave trains are superimposed. This is revealed by the fact that the maximum amplitude of the water level signal after  $t = 12$  s is roughly twice the wave height of the single wave.

The same occurs at gauge 11 ( $x = 30$  m; red line in Figure 4.1), which is still within the basin, but closer than gauge 12 to the seaward boundary. At the location of gauge 11 only a single wave cycle from the estuary wave train is detected (see the red line between 6 and 10 seconds). After that time, the location is reached also by the sea wave train, and the wave signals from both sea and estuary are superimposed, giving birth to a signal whose amplitude is twice the amplitude of the single wave. Furthermore, the time series is regular in its periodicity, both before and after the mutual interaction of the two wave trains. This shows that the wave train from the seaward boundary is allowed

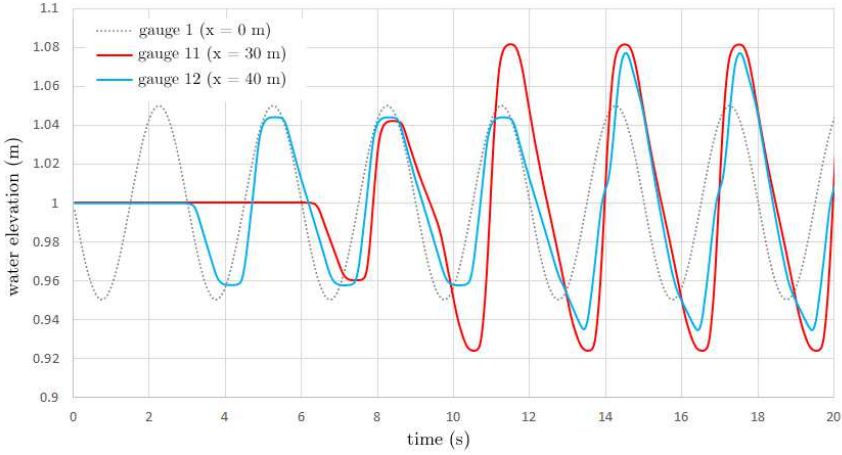


Figure 4.1: Time series of water level for gauges 1 ( $x = 0$  m; dotted line), 11 ( $x = 30$  m; red line), and 12 ( $x = 40$  m; blue line), located in the estuary side of the basin.

to exit the domain once it reaches the estuary window, and no reflection is generated.

As for the capabilities of the landward boundary (i.e. the portion between  $y = 100$  and  $y = 200$  m) to properly reflect incident waves, Figure 4.2 shows the time series for two significant gauges. Gauge 29, at  $x = 45$  m, is located 5 m seaward of the reflective boundary, where gauge 32 is placed. Figure 4.2 shows the period of time in which the gauges are affected by the sea wave train only (between 10 and 30 seconds), so that the interference by the refracted estuary wave train does not affect the signals.

Comparison between the time signals from the two gauges reveals that at the reflective boundary a near-perfect reflection of the sea wave train takes place. Let  $H_{29}$  be the wave height detected at gauge 29 *before* the wave train has impacted the reflective boundary, evaluated as the total oscillation of the first wave cycle from the time series at gauge 29 (light blue line). Let  $H_{32}$  be the wave height of the time signal at the boundary, evaluated as the total oscillation of the water level from the time series at gauge 32 (yellow line). The two heights, and their ratio, are (see the water levels in Figure 4.2):

$$H_{29} = 1.034 - 0.968 = 0.066 \text{ m}; \quad H_{32} = 1.065 - 0.940 = 0.125 \text{ m}; \quad (4.1)$$

$$\frac{H_{32}}{H_{29}} = \frac{0.125 \text{ m}}{0.066 \text{ m}} = 1.89. \quad (4.2)$$

The waves impacting the boundary are then amplified by a factor of 1.89

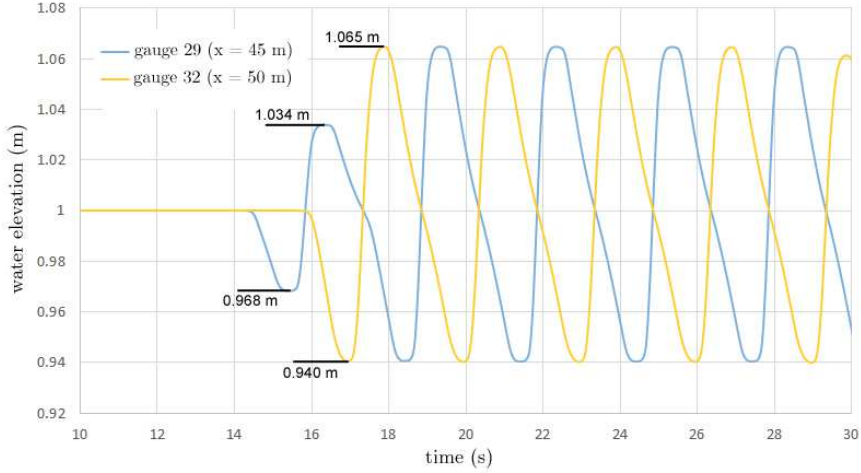


Figure 4.2: Time series of water level for gauges 29 ( $x = 45$  m; light blue line), and 32 ( $x = 50$  m; yellow line), located in the reflective side of the basin.

upon reflection.

In conclusion, this test has shown that the solver is globally able to correctly represent the basic dynamics of wave propagation, interaction and reflection when two opposing sources are considered.

## 4.2 Wave-current interaction on a simplified inlet

Following the study of Olabarrieta et al. [2], a suite of numerical simulations has been performed to inspect the nearshore circulation generated by interacting waves and currents around an idealized inlet configuration. In the following sections a few aspects of the inlet hydromorphodynamics are considered, such as the role of the morphologic elements on the flow fields, the effects of combined waves and jet actions, the arising patterns of sediment redistribution and the generation of vorticity. Whereas possible, similarities and differences with the main findings of Olabarrieta et al. are also addressed.

### 4.2.1 Interaction of waves, currents, and morphology

Our numerical campaign produced results that are partially different than those highlighted by Olabarrieta et al. [2] regarding the relevant flow features of interacting waves and currents around the inlet region.

Figures 4.3, 4.4 and 4.5 show typical velocity fields for the wave-current interaction tests with weak outflow, medium outflow and strong outflow respec-

tively. In each figure, the considered outflow condition interacts with (from top to bottom) absent waves, weak waves and strong waves. All the flow fields reproduced in the figures are averaged over ten wave periods.

The tests featuring a weak outflow current (T1, T4, T7,  $u_c \approx 0.6$  m/s: see Figure 4.3) show a considerable jet instability, regardless of the opposing wave conditions. In all three tests the jet splits itself into two or three branches as soon as it exits the channel mouth, and produces a notable along-shore spreading. It can be argued that the bed friction plays a critical role in this behaviour: in fact, the current may be too weak to win the resisting action of bed friction in the shallowest waters of the shoal, where the frictional forces are the most intense, and hence the jet loses its momentum and consistency. Jet instability also occur for the tests featuring medium (T2, T5, T8:  $u_c \approx 1.1$  m/s: see Figure 4.4) and strong outflows (T3, T6, T9:  $u_c \approx 1.6$  m/s: see Figure 4.5) although to a minor degree, the meandering effect typical of lateral instability being visible only in the most seaward reaches of the jets. This assumption is corroborated by adoption of a stability parameter for jets in shallow waters [132]:

$$S = \frac{c_{\tau,m} B_m}{2d_m} \quad (4.3)$$

where  $c_{\tau}$ ,  $B_m$  and  $d_m$  are, respectively, the Chezy coefficient, the width of the inlet mouth and the water depth at the mouth. The parameter aims at considering the influence of bed friction and width-to-depth ratio on jet stability. Following this formulation, jets are considered unstable if their stability parameter is below a critical value  $S^*$  ranging from 0.06 to 0.6 [133, 134, 135]. In our specific case, being the inlet mouth width  $B_m = 300$  m, the depth at the mouth  $d_m = 3.5$  m and the average Chezy coefficient in the mouth zone  $c_{\tau} = 0.001$ , the jet stability parameter  $S$  is equal to 0.043, which ensures an unconditional time-growing instability of all the jets examined.

In all tests with medium-to-strong outflows, nonetheless, the typical features of a shallow jet extending seawards over a shoal topography are clearly detectable (Figures 4.4 and 4.5). The jets slows down due to the predominant effect of bed friction and spread over the shoal in a conical fashion, making the most offshoreward extent of the ebb shoal visible even by inspection of the velocity contour fields. Within the shoal, the fluid velocity is higher in the main channel than in the lateral plains, where the shallowest waters are located. Finally, all jets extend themselves seawards of the shoal, while gradually reducing their lateral width. Notably, in the wave-current simulations with the most intense wave action in Olabarrieta et al. ( $H_s = 1.5$  m, corresponding to tests T7, T8, T9) the offshore extent of the jet is greatly reduced, if not disrupted, by the strength of the opposing waves.

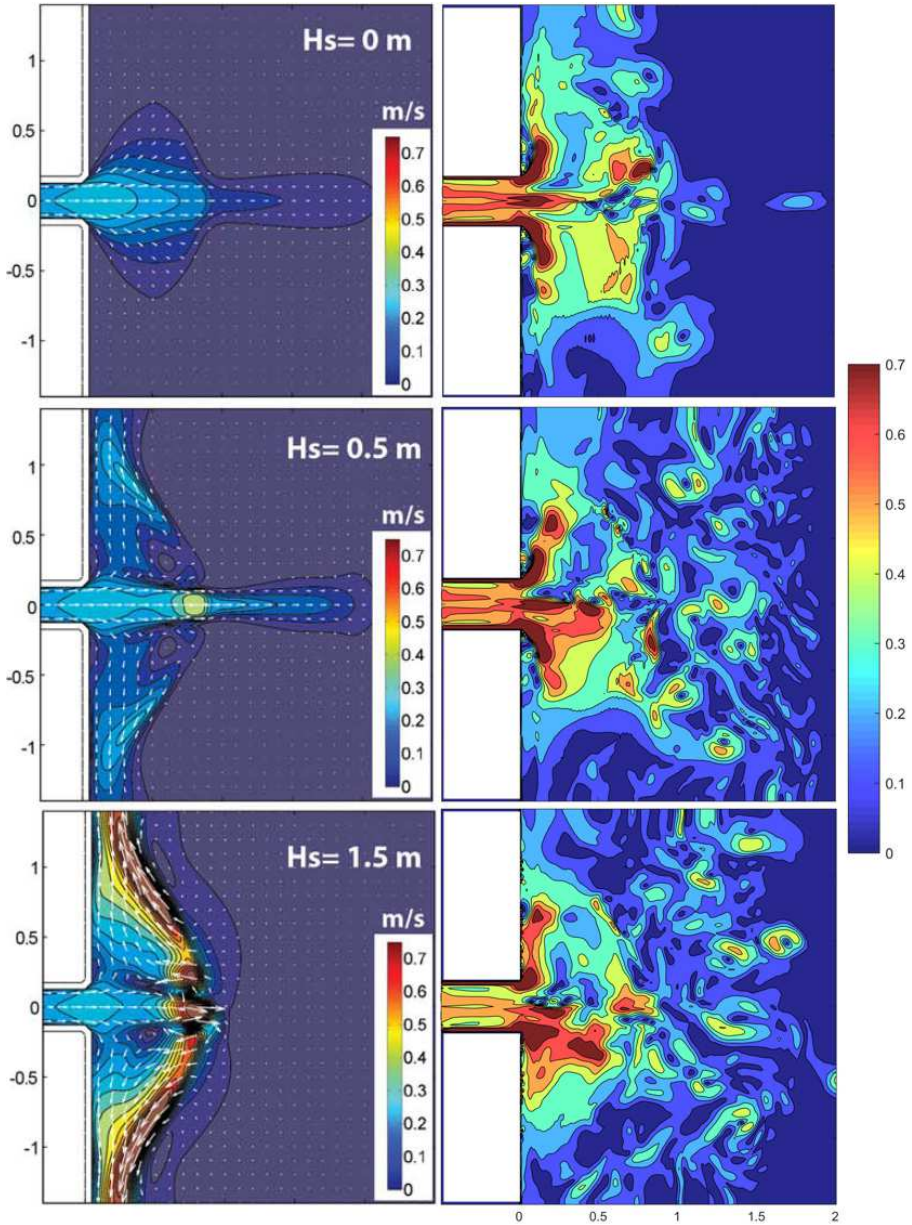


Figure 4.3: Velocity contour fields for wave-current interaction tests with weak outflow ( $u \approx 0.6$  m/s). *From top to bottom*: T1 (no waves,  $H_s = 0$  m); T4 (weak wave regime,  $H_s = 0.5$  m); T7 (strong wave regime,  $H_s = 1.5$  m). The tests by Olabarrieta et al. (adapted with permission) are shown in the left column; our NSWE simulations are shown in the right column.

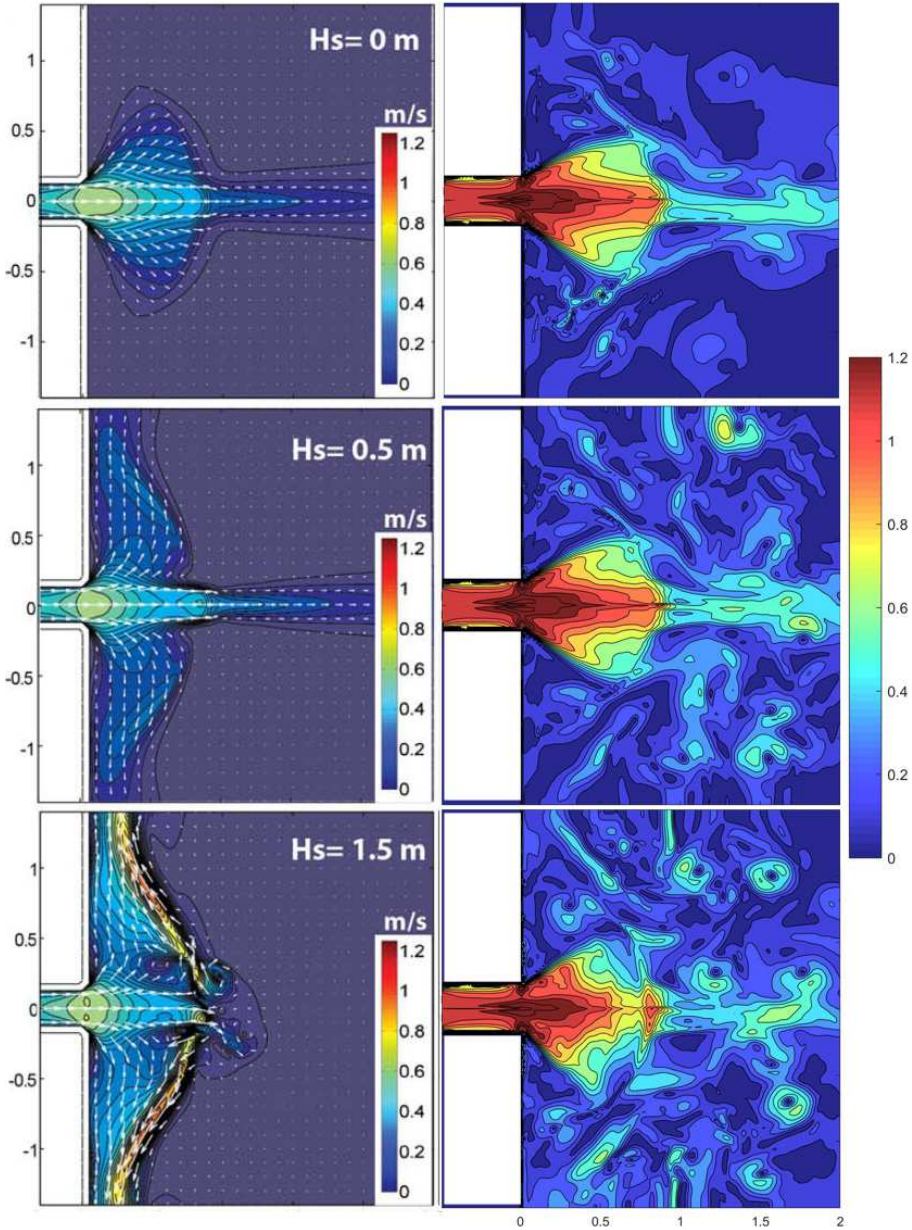


Figure 4.4: Velocity contour fields for wave-current interaction tests with medium outflow ( $u \approx 1.1$  m/s). From top to bottom: T2 (no waves,  $H_s = 0$  m); T5 (weak wave regime,  $H_s = 0.5$  m); T8 (strong wave regime,  $H_s = 1.5$  m). The tests by Olabarrieta et al. (adapted with permission) are shown in the left column; our NSWE simulations are shown in the right column.

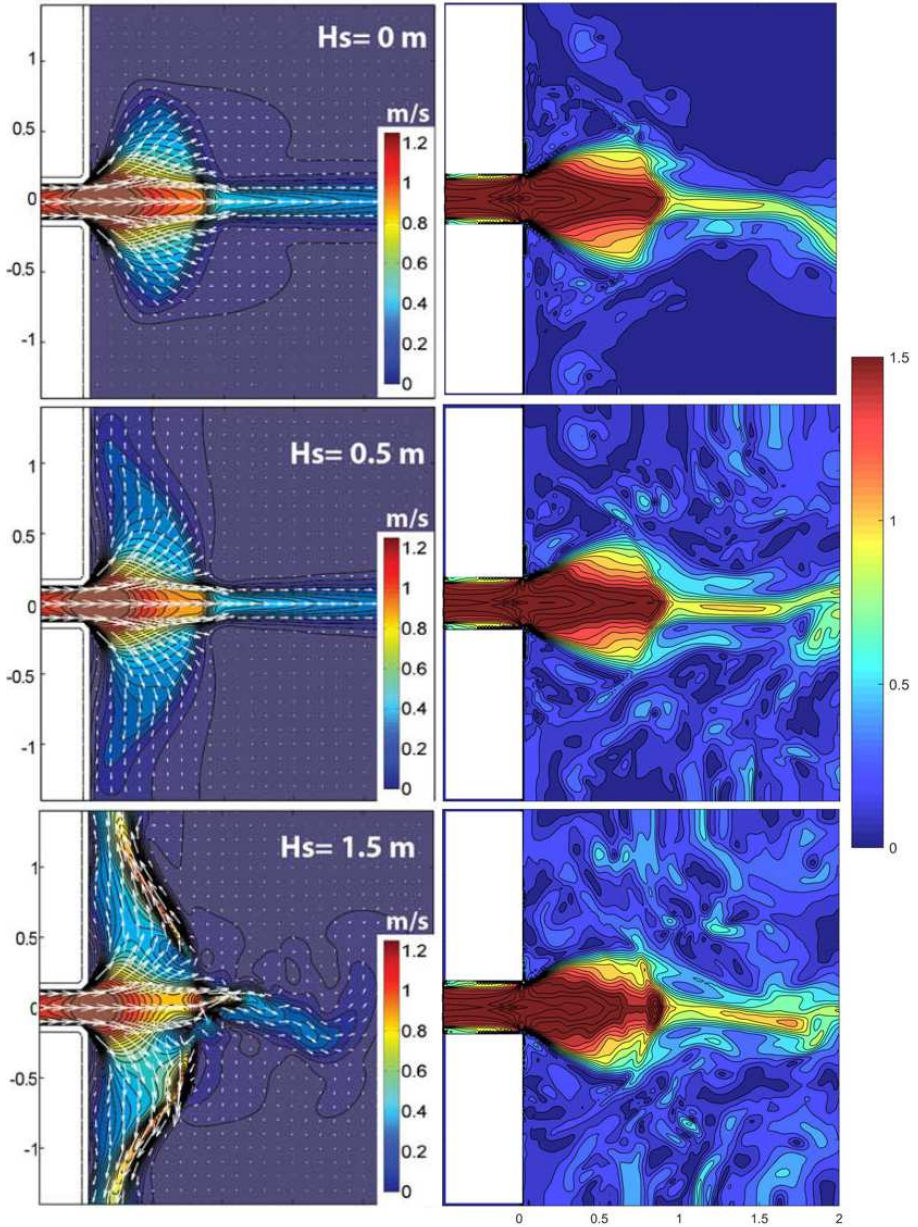


Figure 4.5: Velocity contour fields for wave-current interaction tests with strong outflow ( $u \approx 1.6$  m/s). *From top to bottom*: T3 (no waves,  $H_s = 0$  m); T6 (weak wave regime,  $H_s = 0.5$  m); T9 (strong wave regime,  $H_s = 1.5$  m). The tests by Olabarrieta et al. (adapted with permission) are shown in the left column; our NSWE simulations are shown in the right column.

The study of Olabarrieta et al. clearly acknowledged the presence of landward currents arising along the edge of the shoal. Such currents are recognized at variable intensities in the tests with the most intense wave action, and are credited to an alongshore pressure gradient due to different wave breaking and setup conditions between the ebb shoal (where waves break) and the regions north and south of it (where there is no wave breaking and hence the wave setup is reduced). Our simulations, on the contrary, show only little landward currents at the shoal edge as well as within the shoal. The tests where such currents are the most intense are those in which the wave forcing interacts with a medium outflow (T5 and T8, Figure 4.4): here the landward currents reach values up to 0.4 m/s. This suggests that, in our tests, the wave breaking conditions are roughly similar within and outside of the shoal: the waves approaching the northern and southern parts of the coast — where the shoal morphology is less evident and the beach is more similar to a regular Dean profile — reach a breaking state by feeling the gradual reduction of the water depth, as much as the waves that reach the shoal break by feeling the abrupt change in bathymetry. Hence the resulting gradients in alongshore pressure and wave setup are not as apparent as in the tests of Olabarrieta et al.

In Figure 4.6 the flow velocities along the axis of the main channel, for medium outflow (top panel) and strong outflow (bottom panel) respectively, are presented as a function of the opposing wave regime. Both current outflows show the same global behaviour. The currents speed increases just outside the inlet mouth due to a gradual reduction of the water depth ( $x = 0 - 0.2$  km), then decreases over the shoal mainly because of momentum loss and the action of bottom friction ( $x = 0.2 - 0.9$  km), and finally has a sharp decay at the transition between the ebb shoal and the beach profile ( $x = 0.9 - 1$  km). The increase in jet velocity at the inlet mouth is in the order of 0.2 m/s for the cases with medium outflow, and in the order of 0.4 m/s for the cases with strong outflow: these increments are gradually dissipated as the jets spread over the shoal, with the jet velocities roughly reverting to their initial values as soon as they reach the offshore end of the shoal. The decay rates of the jet velocities outside of the shoal are approximately the same for both medium and strong current outflows.

The effect of the incoming waves on jet flows is clearly visible in the shoal only for the most intense wave regime (T8 and T9,  $H_s = 1.5$  m), where the shoreward-directed accelerations due to wave breaking oppose the jet flow and slow it down even further on the shoal. This dampening effect of breaking waves is visible with a global velocity loss of 0.5 m/s from the inner parts to the outer parts of the shoal (see the red lines in both panels of Figure 4.6, between 0.2 m and 0.7 m). The most energetic wave conditions ( $H_s = 1.5$  m) also generate a distinguishable peak in the fluid velocity right at the tip of the shoal ( $x = 0.9$

## 4.2 Wave-current interaction on a simplified inlet

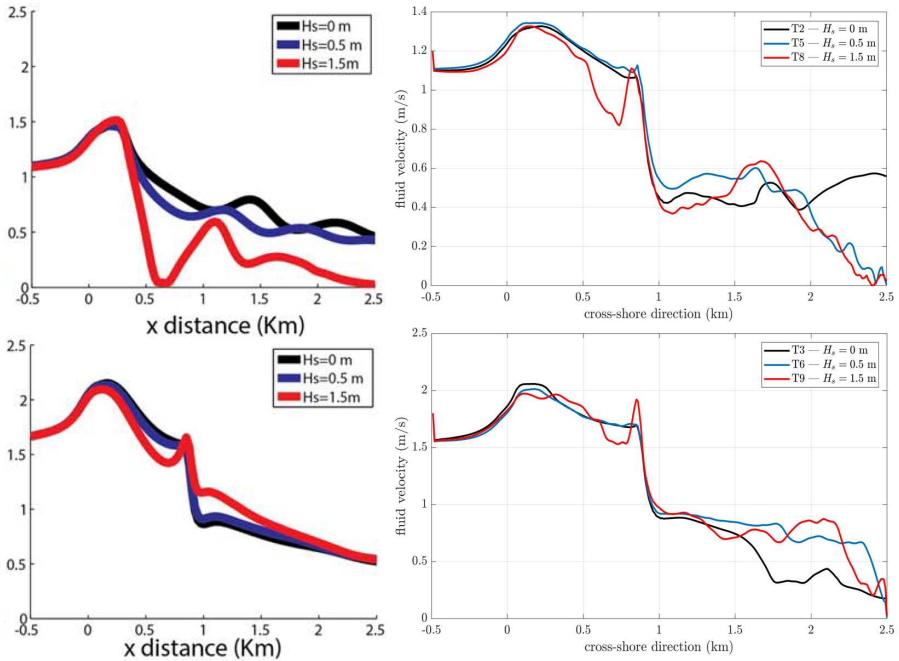


Figure 4.6: Fluid velocity along the main channel central axis as a function of the significant wave height of the opposing waves. *Top panel:* tests with medium outflow (T2, T5, and T8). *Bottom panel:* tests with strong outflow (T3, T6, and T9). The tests by Olabarrieta et al. (adapted with permission) are shown in the left column; our NSWWE simulations are shown in the right column.

m), with the peak intensity being higher with the medium outflow (T8) than with the strong outflow (T9). This phenomenon, in line with the findings of Olabarrieta et al., can be connected with the offshore-directed "return currents" caused by flow convergence and energy concentration toward the main channel due to shoaling and refraction; said concentration consequently reinforces the existing current flow centered in the main channel.

## 4.2.2 Morphodynamic patterns

Wave-current interaction tests T5 and T8, which feature a medium outflow ( $u_c \approx 1.1$  m/s) opposed to weak ( $H_s = 0.5$  m) and strong ( $H_s = 1.5$  m) wave conditions, have been carried out with the aid of our morphodynamic solver described in Section 2.4.2 in order to shed light on the qualitative processes of sediment transport and deposition connected with the flow around the inlet, and the influence of waves on the morphological evolution.

Figure 4.7 presents the morphological deposition-erosion pattern from tests T5 (medium outflow, weak waves) and T8 (medium outflow, strong waves) respectively. Yellow areas represent deposition whereas blue show erosive regions. The colormap representation in the figure has been enhanced to better highlight the morphodynamic features and their differences. Common to both tests is the development of a conical deposition area spanning over the shoal. This region is formed when the jet current slows down as a consequence of shoal spreading and deposits the sediments previously picked up at the inlet mouth and the final reach of the channel, where the jet intensity is high. The conical deposition zone is delimited by a couple of erosion (blue) lines which develop at the boundary between the conical spreading jet and the relatively quiet waters at the sides of the inlet mouth. The erosion lines are much more evident when the jet current is faced with weak waves (top panel of Figure 4.7), and faded when the current is opposed by energetic waves which promote lateral mixing between the spreading jet and the quiet longshore water (bottom panel of Figure 4.7). In both tests, the development of a curved depositional zone following the outward edge of the shoal can also be detected. This is due to the jets abruptly slowing down when reaching the deep water outside the shoal, which, coupled with the shoreward action of the wave breaking-induces accelerations further inducing current slowdown, promotes sediment deposition at the farthest reaches of the shoal.

The effects of a more energetic wave condition on the depositional patterns are mainly visible in the seaward limits of the shoal. The loss in jet momentum and speed, due to wave-breaking induced onshore accelerations, reduce the amount of sediment entrained by the current, as well as the cross-shore extent of the conical deposition zone. Strong wave conditions also cause a moderate

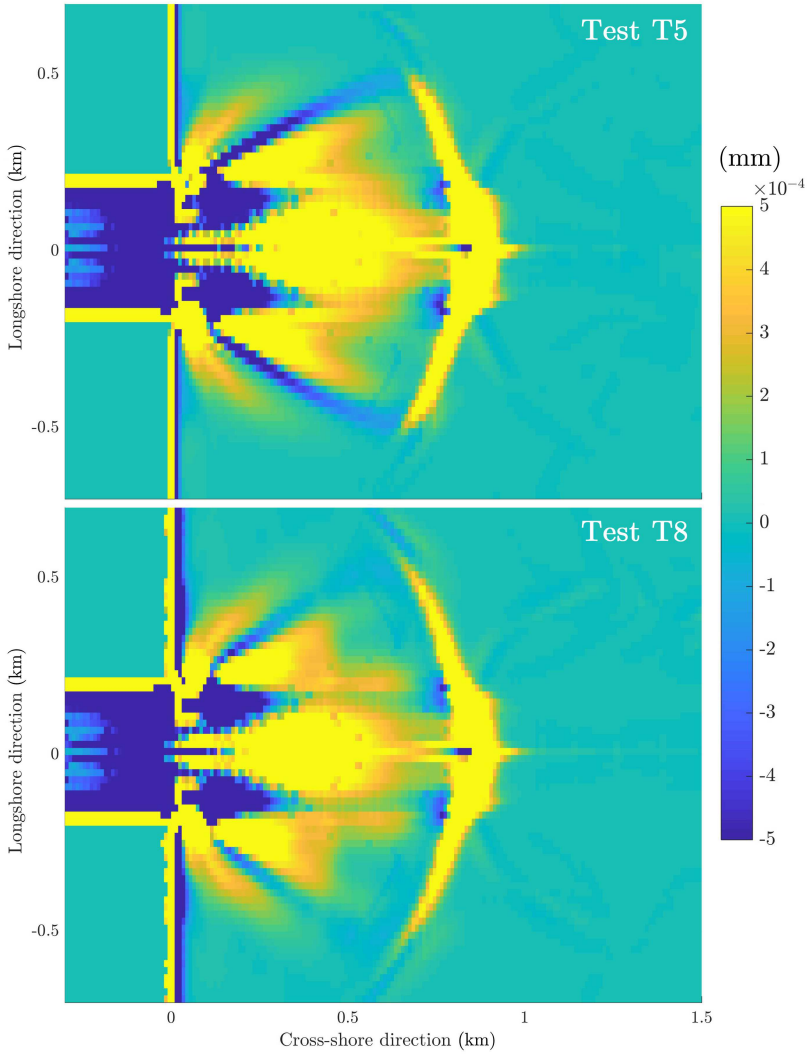


Figure 4.7: Sediment distribution patterns for two wave-current interaction tests with medium outflow. *Top panel*: test T5 (weak wave regime). *Bottom panel*: test T8 (strong wave regime).

lateral expansion of the spreading fan and a lateral widening of the arch-shaped bar.

### 4.2.3 Vorticity

Nearshore dynamics are strongly influenced by large-scale coherent vortical structures similar to those of 2-dimensional turbulence, commonly known as macrovortices. The main mechanism behind the generation of such vortexes often lies in a spatially non-uniform breaking of incoming waves, primarily caused by a non-uniform topography, and a complex interplay between flows happening with different directions and intensities.

Tests T5, T6, T8 and T9, featuring medium-to-strong river currents opposed by both weak and energetic wave states, have been used to investigate the processes behind the generation and dissipation of vortical structures. In this instance the LES model described in section 2.4.3 has been activated to define the role of viscous contributions in vorticity dissipation. Each of the tests has been repeated four times and in each iteration a different value of the viscous model calibration parameter  $\lambda$  has been adopted (namely: 0, 0.1, 0.01, and 0.001). In this way a total of sixteen vorticity tests have been performed.

To identify and characterize in a simple way the structure of vorticity, use is made of the Okubo-Weiss (*OW*) parameter for 2-dimensional turbulent flows [136, 137], defined as follows:

$$OW = s_n^2 + s_s^2 - \omega^2 \quad (4.4)$$

where  $s_n$  and  $s_s$  are the longitudinal and shear fluid strains, respectively, and  $\omega$  is the only non-zero component of the vorticity vector since the flow is 2-dimensional:

$$s_n = \frac{\partial u}{\partial x} - \frac{\partial v}{\partial y}, \quad s_s = \frac{\partial v}{\partial x} + \frac{\partial u}{\partial y} \quad \text{and} \quad \omega = \frac{\partial v}{\partial x} - \frac{\partial u}{\partial y}. \quad (4.5)$$

The *OW* parameter can be seen as a compact index useful to assess the balance between deformative and rotational actions in a turbulent fluid. According to the *OW* criterion the turbulent flow can be roughly divided into two types of regions. Where  $OW > 0$ ,  $s_n^2 + s_s^2 > \omega^2$  and the flow is dominated by fluid straining more than vorticity. Conversely, where  $OW < 0$ ,  $s_n^2 + s_s^2 < \omega^2$  and the rotational effects dominate over deformation [115]. Figure 4.8 presents typical maps of the *OW* parameter for the wave-current interaction tests, extracted at a simulated time  $t = 700$  seconds. In the results shown in Figure 4.8 the calibration parameter is  $\lambda = 0.001$ . The regions darker than grey are dominated by vortical motions, while the areas lighter than grey are dominated by fluid shear deformation.

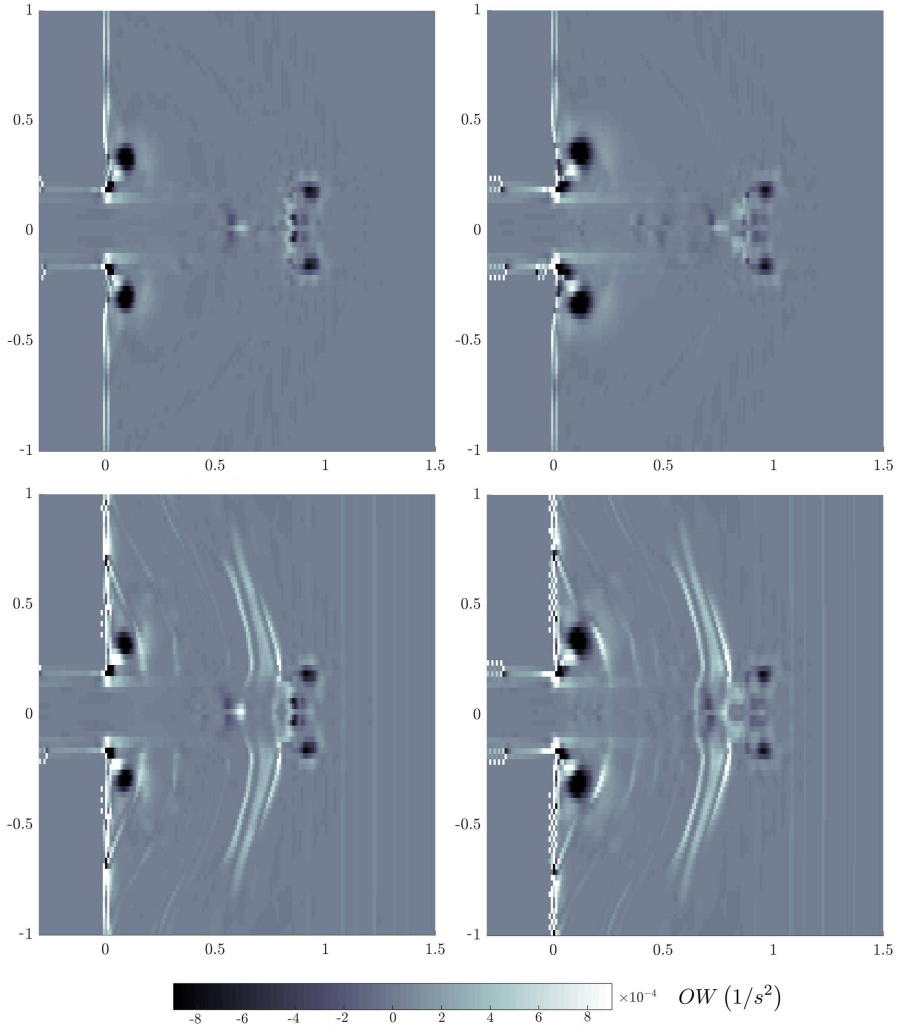


Figure 4.8: Maps for the Okubo-Weiss parameter in the vorticity tests with  $\lambda = 0.001$  at  $t = 700$  seconds.

As Figure 4.8 shows, all the tests highlight a generation of organized vorticity in two regions of the investigated area: (i) at the tip of the shoal, located at  $x = 0.8 - 0.9$  km from the inlet mouth, and (ii) at the corners of the inlet mouth.

The shoal tip is a crucial point for the generation of vorticity. It is the portion of the nearshore where the sharpest variations in bathymetry occur in both cross-shore and alongshore directions, and thus is where the most of wave steepening and breaking is concentrated. Moreover, due to the curved shape of the shoal border, the central parts of a single wave front steepen and break abruptly as it immediately "feels" the reduced water depths; the lateral portions of the wave front, on the contrary, steepen more gradually or nothing at all thanks to gentler beach slopes. This topological factor causes breaking conditions to vary greatly in the alongshore direction, even within the same propagating wave front. According to Peregrine [138], in fact, the injection of potential vorticity  $\Omega = \omega/d$  due to breaking waves can be modelled as

$$\Delta\Omega = \left[ \frac{2d_2}{gd_1(d_1 + d_2)} \right]^{0.5} \frac{\partial E_d}{\partial y} \quad (4.6)$$

where  $\partial E_d/\partial y$  is the cross-flow variation of the specific bore energy dissipation rate:

$$E_d = \frac{g(d_2 - d_1)^3}{4d_1d_2}. \quad (4.7)$$

In the above equations  $d_1$  and  $d_2$  are the water heights at points laying immediately upstream and downstream of the moving bore, respectively. The injected vorticity is therefore higher wherever there is a sensible variation of  $E_d$  in the alongshore direction, i.e. where a great cross-flow difference in the bore height  $d_2 - d_1$  occurs. This is the case of waves locally breaking at an abrupt bathymetry discontinuity such as the offshore reach of the shoal. This mechanism is possibly enhanced by the action of the opposing current, which further steepens the breaking wave at the shoal tip by effects of wave blocking and enhances the difference in bore height between breaking and partially breaking/non-breaking portions of the same wave front.

The vorticity generated at the shoal tip by the concurrent actions of wave breaking and opposing outflow organizes itself into a couple of macrovortices, pictured as the two dark circular regions at  $x = 0.9 - 1$  km in the maps of Figure 4.8. The shoal tip coherent vortical structures gradually move in opposite directions longshore-wise, sustained by the spreading inlet current over the shoal, but are almost held in place by the opposing wave action while they gradually dissipate. This dissipation is to be attributed to viscosity, since the dampening effect of bed friction is relatively negligible outside of the shoal,

where the water depths are larger than inside the shoal itself. A temporal evolution of shoal macrovortices is presented in Figure 4.9, in which the gradual vortex dissipation is expressed by the dark colours turning into lighter shades (this means that the  $OW$  parameter is gradually reducing to zero).

The other location of notable vorticity generation is at the corners of the inlet mouth. Here the discharging current suddenly expands after being confined in the channel and strongly interacts with the fluid located at both sides of the mouth. The jet spreading, therefore, promotes a strong recirculation of the shallow water, which results in a couple of coherent vortices (see Figure 4.8 at  $x = 0 - 0.1$  km). This turbulent mechanism is relatable to a momentum exchange between the current flow spreading over the shoal and the fluid at rest. In a similar way flow momentum is exchanged between the main channel and the adjacent floodplains in a compound channel (see [120]). The vorticity generation in this region is also characterized by a peculiar vorticity-straining-vorticity alternating pattern radiating from the inlet corners; this phenomenon is clearly visible in all the panels in Figure 4.8. The intensity and size of the mouth macrovortices, as well as the extension of the alternate pattern of vorticity and deformation, are proportional to the current intensity and inversely proportional to the strength of opposing waves, the vortexes being slightly larger for tests T6 and T9 (strong outflow) than for tests T5 and T8 (medium outflow). Waves within the shoal act mainly by squashing the mouth vortexes along the shoreline.

The intervention of the LES into the modelling of vorticity structures leads to an overall reduction of the intensity of all eddies as the calibration parameter value goes up. Looking at equation (2.45) it is readily seen that increasing the parameter  $\lambda$  leads to an increment in the numerical eddy viscosity of the fluid. A higher eddy viscosity, in turn, increases the spatial scale at which the effect of viscous dissipation is deemed important; this is reflected in the increment of the so-called dissipation range, i.e. the range, within the energy spectrum of 2-dimensional forced turbulence, in which the vorticity-injected enstrophy (rotational energy) is dissipated by viscous forces within the fluid after an inertial energy transfer from the greater scales (macrovortices) to the smaller scales (sub-grid turbulent motions) according to the energy cascade concept. In short, as the calibration parameter goes up, the resulting viscosity is able to dissipate turbulent energy up to greater length scales, by gradually "extracting" it from the energy-containing eddies.

Whereas the tests performed with the lowest values of the calibration parameter,  $\lambda = 0$  and  $0.001$ , clearly represent the structure of eddies in the earlier times of computation, when  $\lambda = 0.01$  fewer vortices are modelled, and the ones that are resolved are less intense and dissipate quicker. The LES model with the highest calibration value,  $\lambda = 0.1$ , notably suppresses the generation of

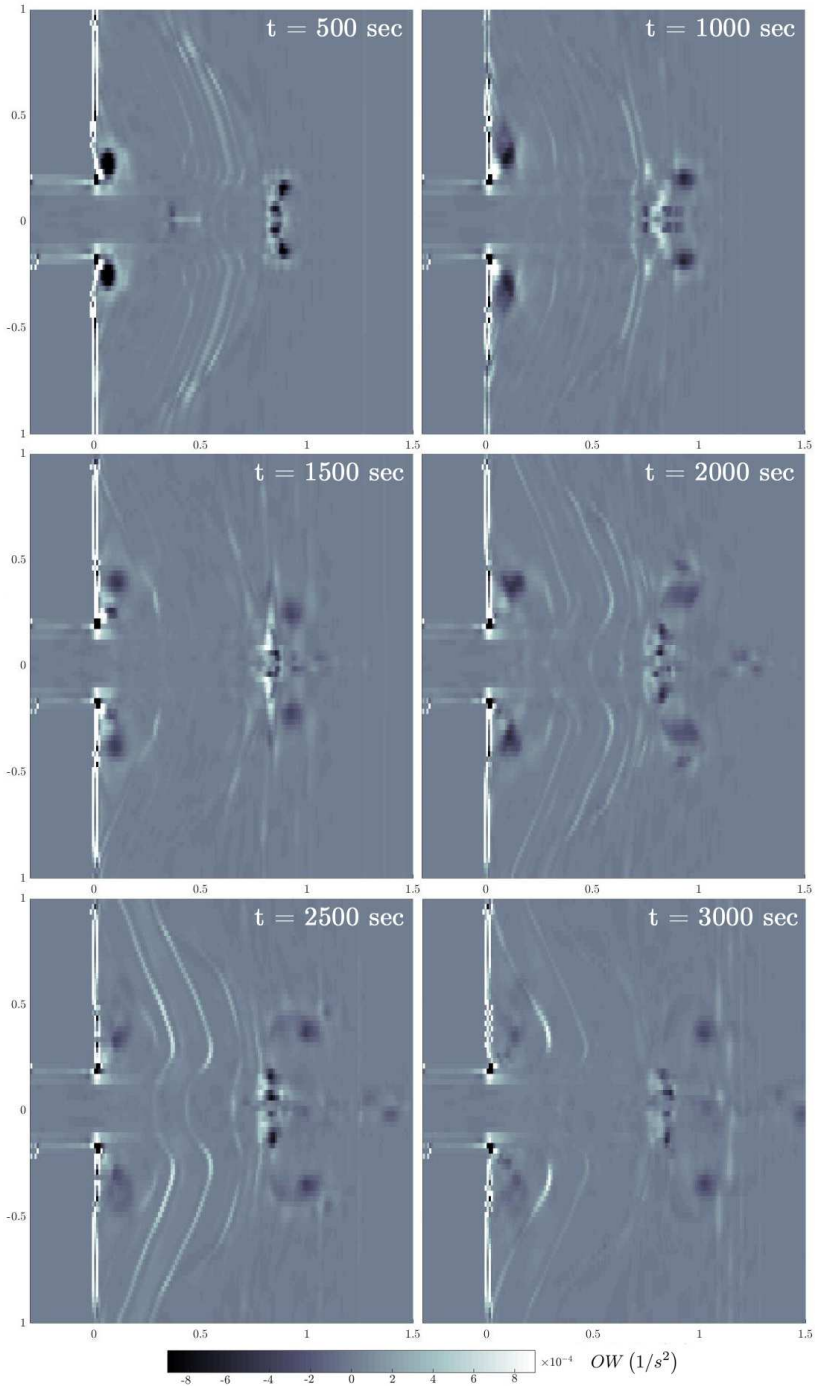


Figure 4.9: Temporal evolution of macrovortices for test T8 (medium outflow, strong wave regime) with  $\lambda = 0.001$  at simulated times between 500 and 3000 seconds.

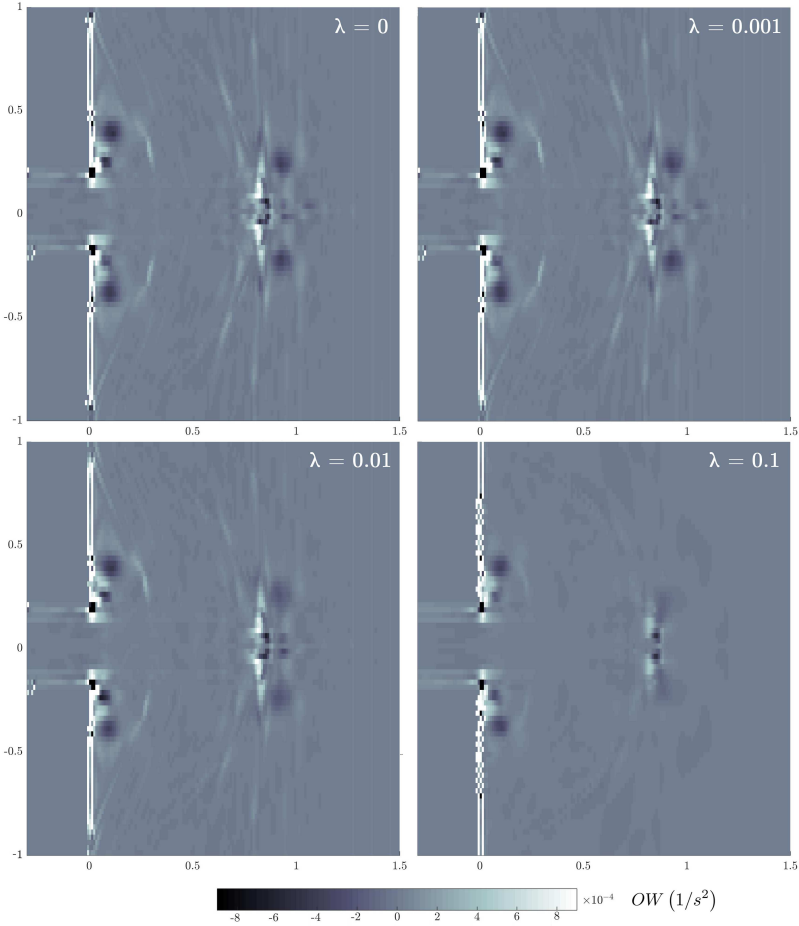


Figure 4.10: Maps for the Okubo-Weiss parameter for test T8 (medium outflow, strong wave regime) at  $t = 1000$  seconds with different values of the LES calibration parameter.

shoal tip vortexes altogether and dampens the development of the inlet mouth vortexes. In the light of this, it may be inferred that the effect of viscosity into the dissipation of enstrophy from turbulent motions is greater for the shoal tip vortexes than for the mouth vortexes. For the latter type of eddies the gradual dissipation through bed friction is deemed more relevant, since within the shoal the lower water depths may intensify the dissipative influence of bottom friction over viscosity (see Figure 4.10).

An index of the global amount of turbulent energy has been defined by integrating only the negative (vorticity-related) values of the  $OW$  parameter over the investigated domain for each test and value of the calibration parameter  $\lambda$ . The integral  $OW$  index has been then plotted against simulated time.

The results are shown in Figure 4.11 for the tests with medium outflow (T5 and T8), and Figure 4.12 for the tests with strong outflow (T6 and T9). All tests present a sharp increase of turbulent energy in the first 500 seconds of simulated time, due to the injection of potential vorticity by the propagating river current front and the initial development of coherent eddies at the shoal tip and at the inlet mouth. This increment is more sensible when  $\lambda$  is low. After reaching a maximum located at around 500 seconds, the turbulent energy decays, meaning that the amount of vorticity stirred by the initial fluid motion into the coherent structures described above is gradually transferring from the largest to the smallest scales and is finally dissipated.

How the turbulent energy decays is highly dependent on the specific value of the eddy viscosity. For very low values of  $\lambda$ , corresponding to low eddy viscosity  $\nu_T$ , the global energy trend shows a moderate reduction and then settles to a stationary value. This is particularly evident in the tests with a weak wave regime (black and red lines in the top panels of Figures 4.11 and 4.12: the energy decay is present between 500 and 1500 seconds). As  $\lambda$  and  $\nu_T$  go up, however, the drop in turbulent energy after the peak is higher and generally does not settle to a value (blue and green lines in the top panels of Figures 4.11 and 4.12). By comparing the top and bottom panels in Figures 4.11 and 4.12 one can see that the energy peak is more or less the same for the two tests with medium outflow (at around 25 for tests T5 and T8, Figure 4.11), and for the two tests with strong outflow (at around 35 for tests T6 and T9, Figure 4.12). This highlights, for our tests, a limited effect of waves on the overall trend of turbulent energy, which is mainly determined by the river current. Waves are, conversely, effective in injecting turbulent energy locally: this is seen through the oscillations of the integral OW parameter, more intense as the wave energy increases. The limited power of waves in stirring potential vorticity may be ascribed to our solver being highly dissipative, therefore estimating the breaking of waves rather offshore. This may cause both weak and strong wave trains to reach the shoal zone with about the same residual energy, making the differences between their behaviour less recognizable.

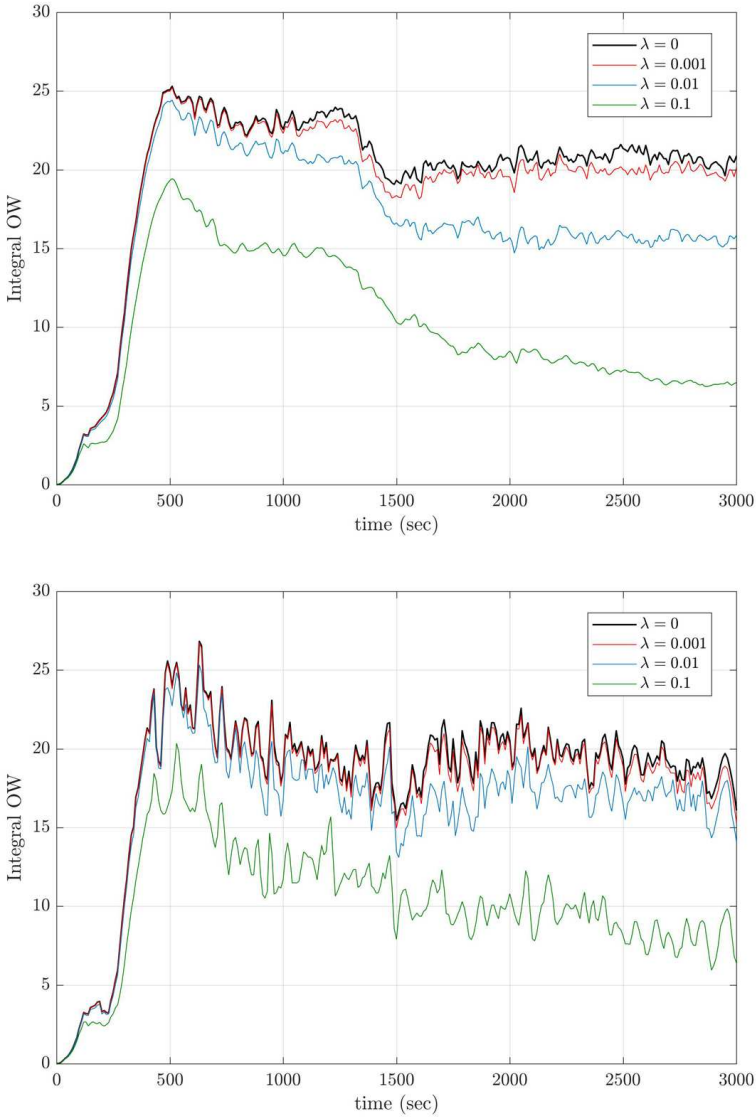


Figure 4.11: Time series of the integral Okubo-Weiss parameter for the tests with medium outflow as a function of the calibration parameter  $\lambda$ . *Top panel*: test T5 (weak wave regime,  $H_s = 0.5$  m). *Bottom panel*: test T8 (strong wave regime,  $H_s = 1.5$  m)

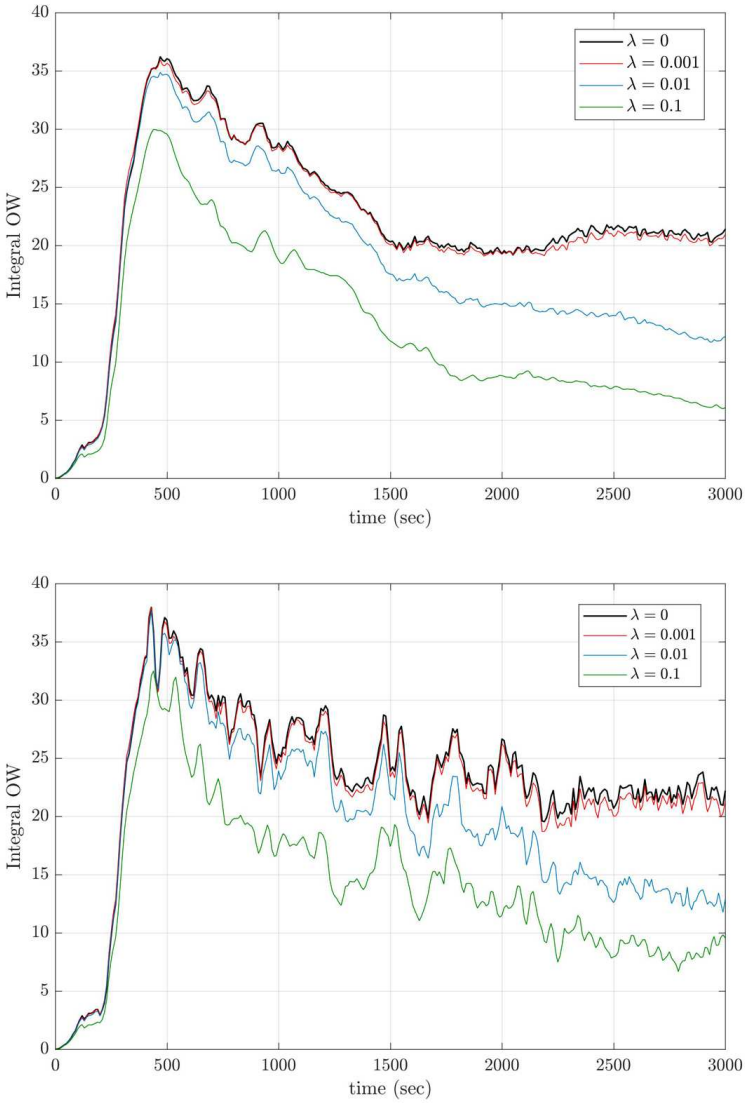


Figure 4.12: Time series of the integral Okubo-Weiss parameter for the tests with strong outflow as a function of the calibration parameter  $\lambda$ . *Top panel:* test T6 (weak wave regime,  $H_s = 0.5$  m). *Bottom panel:* test T9 (strong wave regime,  $H_s = 1.5$  m)

## 4.3 Estuarine morphodynamics at the Misa River mouth

The global morphological evolution at the mouth of the Misa River has been the object of several studies focused on the global evolution of Adriatic Sea beaches and the contrast between summertime and wintertime dynamics in the estuarine system [139, 140, 141, 142]. These studies highlighted a strong interaction of waves, tide and river flows at the estuary and within the final reach of the river during the summer season, and a dominance of river forcing over waves during the high-flow conditions typical of the wintertime. The intense wave-river interaction promotes localized sedimentation of mud and fine sediments in close proximity to the river mouth.

Preliminary hydro-morphological tests on a model bathymetry describing the area around the Misa River mouth have been performed to evaluate the capability of our model to properly catch all the relevant morphodynamic features that may arise in such a microtidal, wave-influenced estuary. The general changes in bathymetry from the numerical simulation has been then compared with seasonal bathymetric variations observed during a field sampling campaign undertaken between 2013 and 2014 [141]. The numerical trials have been carried out for a simulated time of a few hours: since appreciable morphodynamic changes in a nearshore area typically occur in the space of weeks or months, the following erosion-deposition data are to be taken in a qualitative sense, in order to give an overall view on the main sedimentary patterns arising on a seasonal scale.

Figure 4.13 displays the bed variation occurred after five and a half hours (more that 19 000 seconds) of simultaneous action of a river current and a random wave train representing storm conditions. Blue tones represent depositional areas, whereas yellow and red tones represent erosion. Comparison is made with Figure 4.14, which shows the bathymetric variations happened at the final reach of the Misa River and the nearshore in a period between September 2013 and January 2014, with energetic wave condition.

It can be seen that the numerical simulation (Figure 4.13) predicts most of the morphodynamic changes within the final reach of the river and in the region right in front of the mouth, where the interaction between the out-flowing current and the attacking wave state is the most intense. The river channel is dominated by an overall intense erosion at the central axis, with elongated depositional banks occurring at the channel sides where water is shallower and therefore induces a slowdown of the current. A distinctive tripartite deposition-erosion-deposition transversal pattern is detectable also at the river mouth ( $x = 150 - 190$  m,  $y = 120 - 160$  m in Figure 4.13) suggesting that the entity and influence of the river current in a wintertime period are still

sensible in this region. The actual bed variation within the river channel and mouth in Figure 4.14 is mainly dominated by up to 1 m of erosion at the most landward reach of the channel and switches to an alternate erosion-depositional transversal trend before the mouth, thus showing a partial agreement with the numerical results at the lowest portion of the channel. Just outside of the Misa River mouth, in front of the "Banchina di levante" the real-case morphological variation is characterized by a considerable erosive trend with up to 1.5 m of sediment removal, backed by the formation of a slanted bar (red and blue adjacent regions in the right part of Figure 4.14); such an observation suggests the formation of a bar system, sustained by the consistent sediment motion entrained by the energetic wintertime wave regime. This behaviour is recognizable, albeit with less intensity mainly due to the limited runtime, in the numerical result of Figure 4.13, with an extensive (light blue) region of incipient deposition surrounded by an arch-shaped (yellow to light red) erosion zone ( $x = 50 - 150$  m,  $y = 150 - 300$  m in Figure 4.13).

The field campaign also identified a large zone of up to 1.5 m of sediment deposition in front of the ending part of the "Banchina di ponente", represented by the dark blue region in the upper part of Figure 4.14. A zone of similar nature is predicted by the numerical approach, with a considerable depositional

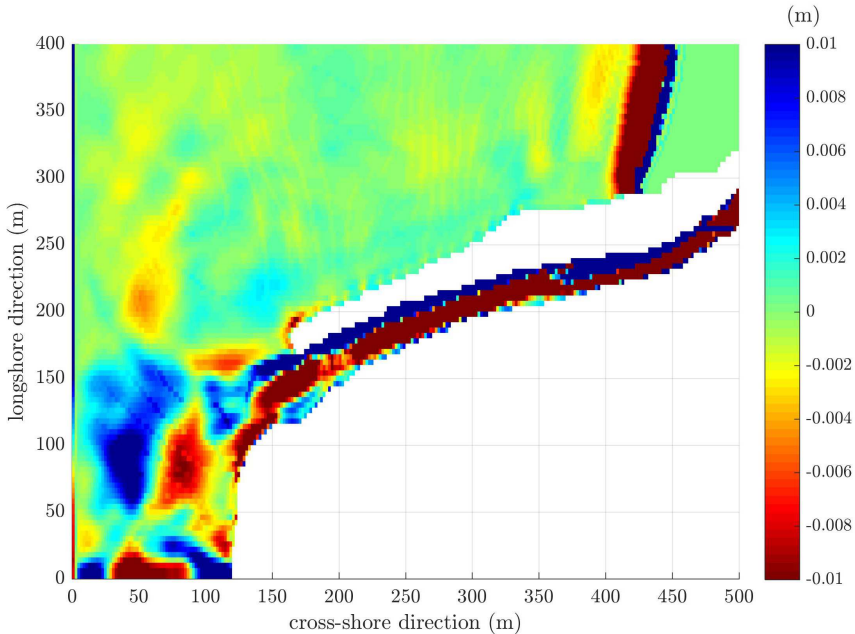


Figure 4.13: Qualitative sedimentary patterns around the mouth of the Misa River after about 5.5 hours of simulated time. Blue regions represent deposition, whereas yellow/red areas represent erosion.



strip extending 100 m in the longshore direction (wide blue spot at  $x = 10 - 70$  m in Figure 4.13). The numerical model also predict an erosion region landward of the abovementioned depositional zone, which is conversely not contemplated by the observed bathymetry.

The bottom profile in the beach area adjacent to the "Banchina di levante", not reviewed by the field campaign, is interested by comparatively less variation than the river and mouth regions of the estuarine setting. The morphodynamic description of this region presents a general incipient accretive behaviour, suggested by the greenish shades of the bathymetry in the surf region between 150 and 350 m cross-shore. A pattern of erosion-deposition is more evident as the bottom depth decreases and the breaking waves have a deeper influence on the morphodynamics. The energetic wave regime, in fact, promotes a noticeable suspension of sediment followed by a marked deposition berm at the numerical shoreline ( $x = 400 - 450$  m,  $y = 300 - 400$  m in Figure 4.13).

In conclusion, our numerical solver has been moderately successful in giving a hint of the main morphological changes due to a typical wintertime storm event at the Misa River nearshore, although some discrepancies have been detected mainly in the sedimentary evolution of the main channel and the region closest to the "Banchina di ponente", where further refinement of our model's predictive capabilities is advisable.

# Chapter 5

## In progress: a bottom boundary layer model

One of the key aspects to be addressed to increase knowledge of the dynamics of shallow water flows — as also suggested in the 1<sup>st</sup> and 2<sup>nd</sup> International Workshops on Swash Zone Processes, held in 2004 and 2014 respectively [143, 144] — deals with the characterization of the bottom boundary layer (BBL hereinafter). In particular the bed shear stress, connected with the development of said layer, is crucial for sediment entrainment, which is the main factor of the beach face evolution induced by wave motion.

Many researchers have successfully attempted to use nearshore circulation models to also predict the beach face evolution by coupling it with adequate morphodynamics models. The most common of such models is based on the Exner equation, which expresses a mass balance between the amount of sediment entrained and laid down during water flows (the morphological model incorporated in our NSWE solver and described in section 2.4.2 can be ascribed to this category). Within these hydro-morphodynamic frameworks, the effect of bottom shear stress, appearing as a source term for the governing equations, is commonly introduced following a Chezy approach, using a constant friction coefficient. This assumption has been derived for steady flows: this is clearly not the case for typical swash flows, which are strongly non stationary and often turbulent; moreover, some recent works observed that the friction coefficient is variable during a single swash cycle [145, 146]. It is therefore needed to adopt more suitable formulations for the description of bed shear stress in shallow flow models.

In recent times, simple approaches for the implementation of a boundary layer model based on the momentum integral method by Fredsøe and Deigaard [72] have been employed in conjunction with NSWE hydrodynamic models to evaluate the evolution of the bottom boundary layer and provide an estimate of the bed shear stress. In the work of Briganti et al. [147] such an approach is applied to a one-dimensional NSWE model to not only compute the frictional term, but also to attempt an analytical description of horizontal

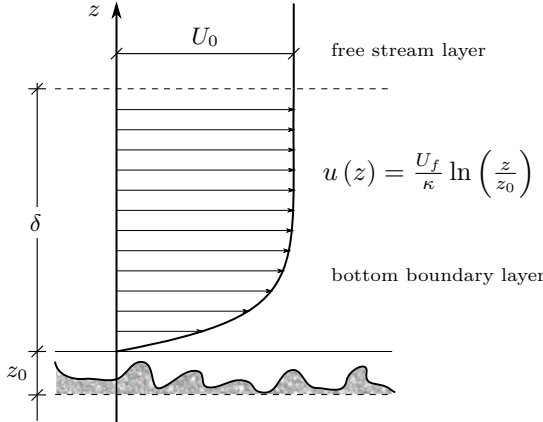


Figure 5.1: Sketch of the bottom boundary layer and the relative velocity log profile

velocity profiles during the events of uprush and backwash in the swash zone.

We here present the generalities of a novel approach for the implementation of the bottom boundary layer in our hydro-morphodynamic solver. The BBL model explained hereafter is implemented within the "source" solving scheme (2.11), whose purpose is to update the depth-averaged velocities  $\mathbf{v} = |u^n, v^n|^T$  to their "advanced" values  $S(\mathbf{v}) = |u^{n+1}, v^{n+1}|^T$  due to the effect of the friction-related source terms appearing at the right hand sides of system (2.3a-c) (all throughout the "source" step the water depth  $d^n$  is kept unaltered). In line with the dimensional splitting operation performed for the NSWE solver, the friction-related velocity correction will be applied separately for the  $x$ -direction and the  $y$ -direction. The BBL model is under development and therefore it has not been activated for the simulations carried out in our study; the outline of the numerical procedure is nevertheless introduced in the present thesis for the sake of presentation.

As a starting point we recall that the horizontal velocity profile within the bottom boundary layer can be approximated by means of a logarithmic law as in the following:

$$u(z) = \frac{U_f}{\kappa} \ln \left( \frac{z}{z_0} \right) \quad (5.1)$$

where  $U_f = \sqrt{|\tau_b|/\rho}$  is the friction velocity,  $\kappa$  is von Karman's constant and  $z_0$  is the zero-velocity level above the beach bed.  $z_0$  is correlated with the bed roughness  $K_n$  through the relationship  $z_0 = K_n/30$  according to Nikuradse. Equation (5.1) defines the horizontal velocity of the fluid inside the boundary layer (of local thickness  $\delta$ ) as a function of the distance from the bed. At the interface between the BBL and the free flow region above it (i.e. at  $z = \delta + z_0$ )

the horizontal velocity  $u$  reaches the free flow velocity  $U_0$ :

$$u(z = \delta + z_0) = U_0 = \frac{U_f}{\kappa} \ln \left( \frac{\delta + z_0}{z_0} \right). \quad (5.2)$$

An adimensional parameter  $Z$  can be then defined as

$$Z = \frac{U_0}{U_f} \kappa = \ln \left( \frac{\delta + z_0}{z_0} \right). \quad (5.3)$$

The parameter  $Z$  can be envisaged as both a velocity-related parameter (a ratio between free stream velocity  $U_0$  and friction velocity  $U_f$ ) and a geometric parameter, varying with the BBL thickness  $\delta$ .

The evolution of  $Z$ , and subsequently  $\delta$ , in time can be evaluated by means of the  $x$ -directed momentum integral equation, which relates the time variation of the boundary layer velocity profile with respect to the free stream velocity, to the  $z$ -variation of the shear stress  $\tau$  within the BBL, both integrated across the boundary layer thickness  $\delta$ . This momentum equation reads:

$$\rho \int_{z_0}^{z_0+\delta} \frac{\partial}{\partial t} [U_0 - u(z)] dz = - \int_{z_0}^{z_0+\delta} \frac{\partial \tau}{\partial z} dz = \tau_b. \quad (5.4)$$

The minus sign clearly indicates that the effect of shear stress acts in contrast with the growth of velocity within the BBL. Plugging expression (5.1) into (5.4), recalling the expression for  $Z$  (5.3) and after some algebraic manipulation (the reader is referred to Chapter 2 in [72] for more details), equation (5.4) can be cast in the form of an ordinary differential equation:

$$\frac{dZ}{dt} = \frac{\frac{\kappa^2 U_0}{z_0} - Z (e^Z - Z - 1) \frac{1}{U_0} \frac{dU_0}{dt}}{e^Z (Z - 1) + 1}. \quad (5.5)$$

Equation (5.5), of unknown  $Z$ , can be solved numerically once adequate values for  $U_0$  and its time derivative  $\frac{dU_0}{dt}$  are known, and thus can be used to time-advance the parameter  $Z$  (thus  $\delta$ ) over a single time step  $\Delta t$ . To this end, the free stream velocities  $U_0^n$  and  $U_0^{n+1}$ , for the present and preceding time level respectively, are computed starting from knowledge of the corresponding depth-averaged velocities, via the formulas proposed by Clarke et al. [148]:

$$U_0 = u \frac{(d - z_0) \ln \left( \frac{\delta + z_0}{z_0} \right)}{d \ln \left( \frac{\delta + z_0}{z_0} \right) - \delta} \quad \text{when} \quad \delta + z_0 < d \quad (5.6a)$$

$$U_0 = u \frac{(d - z_0) \ln \left( \frac{d}{z_0} \right)}{d \ln \left( \frac{d}{z_0} \right) - (d - z_0)} \quad \text{when} \quad \delta + z_0 > d \quad (5.6b)$$

The time derivative  $dU_0/dt$  is then approximated as  $\frac{U_0^n - U_0^{n-1}}{\Delta t}$ . Once approximate values for both  $U_0$  and  $dU_0/dt$  are defined for time level  $n$ , the numerical integration of equation (5.5) — to advance the initial value  $Z^n$  to  $Z^{n+1}$  over the whole time step  $\Delta t$  — is performed by means of an explicit fourth order Runge-Kutta scheme with Cash-Karp coefficients [149, 150], the application of which will be briefly summarized in the following. The ordinary differential equation (5.5) can be seen as

$$\frac{dZ}{dt} = \mathcal{F}(Z), \quad (5.7)$$

where the right hand side of the equation has been labeled  $\mathcal{F}$  and is assumed as a function of the parameter  $Z$  only. Considering a time interval  $h$  over which to solve (5.5) (which need not be equal to the whole time step  $\Delta t$ ), the formula for the explicit Runge-Kutta method that advances the solution  $Z$  from  $t^n$  to  $t^{n+1} \equiv t^n + h$  is

$$\begin{aligned} Z^{n+1} &= Z^n + h \sum_{i=1}^6 c_i k_i, \\ &= Z^n + h [c_1 k_1 + c_2 k_2 + c_3 k_3 + c_4 k_4 + c_5 k_5 + c_6 k_6]. \end{aligned} \quad (5.8)$$

$k_i$ , with  $i = 1 \dots 6$ , are six consecutive evaluations of the function  $\mathcal{F}$  performed at six different locations within the time increment  $h$ : namely,

$$\begin{aligned} k_1 &= \mathcal{F}[Z^n], \\ k_2 &= \mathcal{F}[Z^n + h b_{21} k_1], \\ k_3 &= \mathcal{F}[Z^n + h (b_{31} k_1 + b_{32} k_2)], \\ k_4 &= \mathcal{F}[Z^n + h (b_{41} k_1 + b_{42} k_2 + b_{43} k_3)], \\ k_5 &= \mathcal{F}[Z^n + h (b_{51} k_1 + b_{52} k_2 + b_{53} k_3 + b_{54} k_4)], \\ k_6 &= \mathcal{F}[Z^n + h (b_{61} k_1 + b_{62} k_2 + b_{63} k_3 + b_{64} k_4 + b_{65} k_5)]. \end{aligned} \quad (5.9)$$

The coefficient  $c_i$  and  $b_{ij}$ , along with the node values  $a_i$  which are not used in this implementation, can be suitably arranged in the following Butcher

tableau for the Cash-Karp method:

0							0							
$a_2$	$b_{21}$						$\frac{1}{5}$	$\frac{1}{5}$						
$a_3$	$b_{31}$	$b_{32}$					$\frac{3}{10}$	$\frac{3}{40}$	$\frac{9}{40}$					
$a_4$	$b_{41}$	$b_{42}$	$b_{43}$				$\frac{3}{5}$	$\frac{3}{10}$	$-\frac{9}{10}$	$\frac{6}{5}$				
$a_5$	$b_{51}$	$b_{52}$	$b_{53}$	$b_{54}$			1	$-\frac{11}{54}$	$\frac{5}{2}$	$-\frac{70}{27}$	$\frac{35}{27}$			
$a_6$	$b_{61}$	$b_{62}$	$b_{63}$	$b_{64}$	$b_{65}$			$\frac{7}{8}$	$\frac{1631}{55296}$	$\frac{175}{512}$	$\frac{575}{13824}$	$\frac{44275}{110592}$	$\frac{253}{4096}$	
$5^{\text{th}}$	$c_1$	$c_2$	$c_3$	$c_4$	$c_5$	$c_6$	$5^{\text{th}}$	$\frac{37}{378}$	0	$\frac{250}{621}$	$\frac{125}{594}$	0	$\frac{512}{1771}$	
$4^{\text{th}}$	$c_1$	$c_2$	$c_3$	$c_4$	$c_5$	$c_6$	$4^{\text{th}}$	$\frac{2825}{27648}$	0	$\frac{18575}{48384}$	$\frac{277}{14336}$	0	$\frac{1}{4}$	

Note that two distinct sets of values for the coefficient  $c_i$  are available. When the first set of values is used for the advancing step in equation (5.8), the obtained solution for  $Z^{n+1}$  is fifth-order accurate; conversely, the adoption of the second set of values gives a fourth-order accurate solution for  $Z^{n+1}$ . The explicit method described above is indeed particularly convenient for the inclusion of an adaptive stepsize technique, since the difference between fifth- and fourth-order solutions can be taken as the truncation error of the fourth-order solution: if said error is greater than a prescribed accuracy, then the stepping interval  $h$  initially assumed for the Runge-Kutta step is too large and must be reduced accordingly. On the other hand, if the error is much smaller than the desired accuracy, the interval  $h$  adopted for the current step is too stringent and can be safely increased a bit for the next step. These considerations are efficiently summarized by a comprehensive condition for the step adjustment [150]. If step  $h_1$  produced an error  $\Delta_1$ , then the step  $h_0$  that would have given our desired accuracy  $\Delta_0$  is easily estimated as

$$h_0 = \begin{cases} Sh_1 \left| \frac{\Delta_0}{\Delta_1} \right|^{0.20} & \text{if } \Delta_0 \geq \Delta_1, \\ Sh_1 \left| \frac{\Delta_0}{\Delta_1} \right|^{0.25} & \text{if } \Delta_0 < \Delta_1. \end{cases} \quad (5.10)$$

$S$  is a safety coefficient equal to 0.9, introduced to absorb the uncertainties related to the non-exactness of error estimates. Once the stepping procedure is completed, the advanced value  $Z^{n+1}$  is used as the new initial value for the next Runge-Kutta step. As said before, it is not necessary for the interval  $h$  to be equal to the solver-defined time step  $\Delta t$ ; as a matter of fact, it is neither desirable, since most often the time steps needed to satisfy the stability condition of the NSWE solver are too large to guarantee a sufficient accuracy in a single Runge-Kutta step, and the adaptive stepsize control would shrink it altogether. Hence the decision of adopting a different time step for equation (5.8) than the one coming from the NSWE solver. As the first tentative value for  $h$ ,

we assumed half the present time step; as the numerical integration goes on,  $h$  will be adapted accordingly and the single Runge-Kutta steps will accumulate to cover the whole  $\Delta t$ .

Once the new value  $Z^{n+1}$ , an estimate of the BBL layer thickness  $\delta^{n+1}$  is evaluated by inverting equation (5.3):

$$\delta^{n+1} = z_0 \left( e^{Z^{n+1}} - 1 \right). \quad (5.11)$$

The friction velocity  $U_f^{n+1}$  is now estimated by inverting equation (5.2). Since  $U_0^{n+1}$  is unknown because the corresponding depth-averaged velocity  $u^{n+1}$  is, the value  $U_0^n$  will be used instead:

$$U_f^{n+1} = \frac{U_0^n}{Z^{n+1}} \kappa. \quad (5.12)$$

An estimate of the bottom friction  $\tau_{\text{BBL}}^{n+1}$  is achieved by inverting the expression for the friction velocity:

$$\tau_{\text{BBL}}^{n+1} = \rho U_f^{n+1}. \quad (5.13)$$

Finally, the depth-averaged velocity entering the "source" scheme is altered by the friction-induced velocity loss:

$$u^{n+1} = u^n - \frac{\tau_{\text{BBL}}^{n+1}}{\rho d^n} \Delta t. \quad (5.14)$$

# Chapter 6

## Conclusions

In this thesis, a numerical approach to the analysis of the wave influence on the morphology and hydrodynamic response of estuaries and inlet mouths has been proposed.

The available numerical solver for shallow waters by Brocchini et al. [1], based on a finite-volume resolution scheme for the NSW-Exner equation system, has been integrated with a simple estuary model to extend its operability to cases where both marine and fluvial inputs are present. The new estuary model allow for a current and water elevation time history to enter the computational domain at a certain angle.

The so-modified solver has been then used to carry out two numerical campaigns. The first set of tests aim at recreating the complex wave-current interaction on an idealized inlet configuration; such tests are inspired by a previous study on the circulation of the New River inlet, North Carolina, by Olabarrieta et al. [2]. The second group of tests focuses on evaluating the novel solver's capabilities in describing the morphodynamic evolution of a real estuarine environment: the microtidal estuary of the Misa River in Senigallia, Italy. The outcome of these tests has been compared with the main results of a field sampling campaign conducted at the mouth of the Misa River between September 2013 and January 2014 [141] to check the goodness of the solver's predictions.

The wave-current interaction tests have given encouraging results, with the novel estuarine solver being able to globally represent the dynamics of a shallow jet opposed by waves of different intensities. The tests have shown that the effect of incident waves on the global hydrodynamics of outflowing jets are dependent on both wave and jet intensity. The low-intensity jet has shown a strong instability with a considerable alongshore spreading; the medium and strong currents have conversely shown a consistent behavior over the shoal zone and further offshore. The influence of wave action on jet hydrodynamics is more evident as the wave regime energy increases, with a moderate decrement of the outflowing current velocity within the shoal and a reduction in jet width and intensity once the current has left the shoal. For medium outflow conditions

and strong wave regime, the wave steepening and breaking at the edge of the shoal produce intense shore-directed accelerations, which eventually lead to a slight lateral expansion of the current spreading fan. For both medium and strong jet conditions, the strong wave regime is successful in reducing the velocity of the spreading jet within the shoal. In addition, the most energetic waves cause a distinguishable peak of the centerline jet velocity at the tip of the shoal; it is arguable that this phenomenon, in line with the results obtained by Olabarrieta et al., may be caused by the return currents generated by flow and energy concentration of the refracting waves towards the main channel.

As for the morphodynamics of inlet mouths, two tests with a moderate jet outflow and medium-to-intense wave regime have given rise to the same qualitative patterns of erosion-deposition: in both tests the areas where the bulk of the sediment motion takes place are the ebb shoal and the terminal reach of the channel. Common features of the morphological patterns are a conical depositional area determined by the jet currents slowing down over the shoal, a massive erosion of sediment from the ending part of the inlet channel and the inner portion of the shoal, and the generation of an arch-shaped bar along the offshore edge of the ebb shoal. The action of waves intervene through a slight transversal expansion and cross-shore extension of the deposition fan, and in an increase of the length of the arch-shaped bar in the longshore direction.

Vorticity tests has revealed the generation of a couple of macrovortical structures at the tip of the shoal, mainly due to local wave steepening and the subsequent generation of a breaker front which, in conjunction with adjacent non-breaking wave fronts, contribute to the injection of potential vorticity in the water column. The vorticity generation is enhanced by the opposing jet currents which favours wave steepening and breaking. Analysis of the same vorticity in a NSWE-LES framework has shown that, in line with the concept of energy cascade for freely decaying 2-dimensional turbulence, an increasing eddy viscosity increases reduces the dissipation wavenumber (i.e. increases the dissipation scale under which the dissipating action of viscosity is deemed important), and also reduces the inertial range in which enstrophy is transferred to vorticity at smaller scales without any energy dissipation. This results in dampened and shorter-lived macrovortices.

The morphodynamic test aimed at describing the bathymetric evolution of the Misa River mouth, although showing room for improvement, has been moderately successful in predicting some of the salient features of the bed variation, such as the development of a large depositional area offshore of the river mouth and the global depositional-erosive trend at the final reach of the river.

As for future developments, the definition and implementation of a robust model for the bottom boundary layer in shallow waters may lead to a more

accurate representation of bottom stresses and hence improve the numerical description of the hydrodynamics and sediment distribution mechanisms in the nearshore.



# Bibliography

- [1] M. Brocchini, R. Bernetti, A. Mancinelli, and G. Albertini, “An efficient solver for nearshore flows based on the WAF method,” *Coastal Engineering*, vol. 43, no. 2, pp. 105–129, 2001. [https://doi.org/10.1016/s0378-3839\(01\)00009-6](https://doi.org/10.1016/s0378-3839(01)00009-6)
- [2] M. Olabarrieta, W. R. Geyer, and N. Kumar, “The role of morphology and wave-current interaction at tidal inlets: An idealized modeling analysis,” *Journal of Geophysical Research: Oceans*, vol. 119, no. 12, pp. 8818–8837, 2014. <https://doi.org/10.1002/2014jc010191>
- [3] D. A. Ross, *Introduction to Oceanography*. HarperCollins, 1995.
- [4] G. M. Perillo, “Definitions and geomorphologic classifications of estuaries,” in *Developments in Sedimentology*. Elsevier, 1995, pp. 17–47. [https://doi.org/10.1016/s0070-4571\(05\)80022-6](https://doi.org/10.1016/s0070-4571(05)80022-6)
- [5] W. M. Cameron and D. W. Pritchard, “Estuaries,” in *The Sea*, M. N. Hill, Ed. John Wiley & Sons, 1963, vol. 2, pp. 306–324.
- [6] D. W. Pritchard, “What is an estuary: physical viewpoint,” in *Estuaries*, G. H. Lauff, Ed. American Association for the Advancement of Science, 1967, vol. 83, pp. 3–5.
- [7] R. W. Fairbridge, “The estuary: its definition and geodynamic cycle,” in *Chemistry and biochemistry of estuaries*, E. Olausson and I. Cato, Eds. John Wiley & Sons, 1980, pp. 1–35.
- [8] H. E. Clifton, “Estuarine deposits,” in *Sandstone Depositional Environments*, P. A. Scholle and D. Spearing, Eds. American Association of Petroleum Geologists, 1982, pp. 179–189. <http://geoscienceworld.org/content/sandstone-depositional-environments>
- [9] C. T. Lewis and C. Short, *A new Latin Dictionary*. Oxford University Press, 1879, pp. 62–63.
- [10] D. Rochford, “Studies in Australian estuarine hydrology. I: Introductory and comparative features,” *Marine and Freshwater Research*, vol. 2, no. 2, pp. 1–116, 1951.

## Bibliography

- [11] M. M. Nichols and R. B. Biggs, “Estuaries,” in *Coastal Sedimentary Environments*, R. A. Davis, Ed. Springer, 1985.
- [12] R. W. Dalrymple, B. A. Zaitlin, and R. Boyd, “Estuarine facies models: conceptual basis and stratigraphic implications,” *Journal of Sedimentary Petrology*, vol. 62, no. 6, pp. 1130–1146, 1992. <https://doi.org/10.1306/d4267a69-2b26-11d7-8648000102c1865d>
- [13] R. H. Meade, “Sources, sinks, and storage of river sediment in the Atlantic drainage of the United States,” *The Journal of Geology*, vol. 90, no. 3, pp. 235–252, 1982. <https://doi.org/10.1086/628677>
- [14] A. Valle-Levinson, Ed., *Contemporary Issues in Estuarine Physics*. Cambridge University Press, 2010. <https://doi.org/10.1017/CBO9780511676567>
- [15] K. R. Dyer, *Estuaries: a Physical Introduction*. John Wiley & Sons, 1997. <http://eu.wiley.com/WileyCDA/WileyTitle/productCd-0471974714.html>
- [16] A. Valle-Levinson, “Classification of estuarine circulation,” in *Treatise on Estuarine and Coastal Science*. Elsevier, 2011, pp. 75–86. <https://doi.org/10.1016/b978-0-12-374711-2.00106-6>
- [17] J. Davies, “A morphogenic approach to world shorelines,” *Zeitschrift fur Geomorphologie*, vol. 8, pp. 127–142, 1964.
- [18] M. O. Hayes, “Morphology of sand accumulation in estuaries: An introduction to the symposium,” in *Geology and Engineering*. Elsevier, 1975, pp. 3–22.
- [19] M. O. Hayes, “Barrier island morphology as a function of tidal and wave regime,” *Barrier Islands – from the Gulf of St. Lawrence to the Gulf of Mexico*, pp. 1–27, 1979.
- [20] M. O. Hayes, “General morphology and sediment patterns in tidal inlets,” *Sedimentary Geology*, vol. 26, pp. 139–156, 1980. [https://doi.org/10.1016/0037-0738\(80\)90009-3](https://doi.org/10.1016/0037-0738(80)90009-3)
- [21] J. Schubel, “Size distributions of the suspended particles of the Chesapeake Bay turbidity maximum,” *Netherlands Journal of Sea Research*, vol. 4, no. 3, pp. 283–309, 1969.
- [22] R. Biggs, “Sources and distribution of suspended sediment in northern Chesapeake Bay,” *Marine Geology*, vol. 9, no. 3, pp. 187–201, 1970. [https://doi.org/10.1016/0025-3227\(70\)90014-9](https://doi.org/10.1016/0025-3227(70)90014-9)

- [23] J. Schubel, “Tidal variation of the size distribution of suspended sediment at a station in the Chesapeake Bay turbidity maximum,” *Netherlands Journal of Sea Research*, vol. 5, no. 2, pp. 252–266, 1971. [https://doi.org/10.1016/0077-7579\(71\)90012-3](https://doi.org/10.1016/0077-7579(71)90012-3)
- [24] C. H. Hobbs III, J. P. Halka, R. T. Kerhin, and M. J. Carron, “Chesapeake Bay sediment budget,” *Journal of Coastal Research*, pp. 292–300, 1992.
- [25] R. A. Davis and P. Barnard, “Morphodynamics of the barrier-inlet system, west-central Florida,” *Marine Geology*, vol. 200, no. 1-4, pp. 77–101, 2003. [https://doi.org/10.1016/s0025-3227\(03\)00178-6](https://doi.org/10.1016/s0025-3227(03)00178-6)
- [26] R. W. Frey and P. B. Basan, “Coastal salt marshes,” in *Coastal Sedimentary Environments*, R. A. Davis, Ed. Springer, 1985.
- [27] K. Dyer, M. Christie, and E. Wright, “The classification of intertidal mudflats,” *Continental Shelf Research*, vol. 20, pp. 1039–1060, 2000. [https://doi.org/10.1016/s0278-4343\(00\)00011-x](https://doi.org/10.1016/s0278-4343(00)00011-x)
- [28] D. Pritchard, “Estuarine circulation patterns,” in *Proceedings of the American Society of Civil Engineers*, vol. 81, no. 6. ASCE, 1955, pp. 1–11.
- [29] J. Schijf and J. Schönflöd, “Theoretical considerations on the motion of salt and fresh water,” in *Proceedings of the Minnesota International Hydraulic Convention*. IAHR, 1953, pp. 321–333. <https://repository.tudelft.nl/islandora/object/uuid%3A5d1c2eb0-d51c-4b3c-ad77-a77513941c6c>
- [30] W. R. Geyer and D. M. Farmer, “Tide-induced variation of the dynamics of a salt wedge estuary,” *Journal of Physical Oceanography*, vol. 19, no. 8, pp. 1060–1072, 1989. [https://doi.org/10.1175/1520-0485\(1989\)019<1060:tivotd>2.0.co;2](https://doi.org/10.1175/1520-0485(1989)019<1060:tivotd>2.0.co;2)
- [31] B. A. Zaitlin and B. C. Shultz, “Wave-influenced estuarine sand body, Senlac Heavy Oil Pool, Saskatchewan, Canada,” in *Sandstone Petroleum Reservoirs*. Springer, 1990, pp. 363–387. [https://doi.org/10.1007/978-1-4613-8988-0\\_16](https://doi.org/10.1007/978-1-4613-8988-0_16)
- [32] R. A. Davis and M. O. Hayes, “What is a wave-dominated coast?” *Marine Geology*, vol. 60, no. 1-4, pp. 313–329, 1984. [https://doi.org/10.1016/0025-3227\(84\)90155-5](https://doi.org/10.1016/0025-3227(84)90155-5)

## Bibliography

- [33] P. S. Roy, “New South Wales estuaries: Their origin and evolution,” in *Coastal Geomorphology in Australia*, B. G. Thom, Ed. Academic Press, 1984, pp. 99–121.
- [34] P. Roy, P. Cowell, M. Ferland, and B. Thom, “Wave-dominated coasts,” in *Coastal evolution: Late Quaternary shoreline morphodynamics*, R. W. G. Carter and W. C. D., Eds. Cambridge University Press, 1994, pp. 121–186.
- [35] J. L. Davies, *Geographical Variation in Coastal Development*. Longman, 1972.
- [36] R. W. Dalrymple and K. Choi, “Morphologic and facies trends through the fluvial–marine transition in tide-dominated depositional systems: A schematic framework for environmental and sequence-stratigraphic interpretation,” *Earth-Science Reviews*, vol. 81, no. 3–4, pp. 135–174, apr 2007. <https://doi.org/10.1016/j.earscirev.2006.10.002>
- [37] D. B. Duane, M. E. Field, E. P. Meisburger, D. J. Swift, and S. J. Williams, “Linear shoals on the Atlantic inner continental shelf, Florida to Long Island,” in *Shelf Sediment Transport: Process and Pattern*, D. J. Swift, D. B. Duane, and O. H. Pilkey, Eds. Dowden, Hutchinson & Ross, 1972, pp. 447–498.
- [38] D. Calvete, M. Walgreen, H. E. de Swart, and A. Falqués, “A model for sand ridges on the shelf: Effect of tidal and steady currents,” *Journal of Geophysical Research: Oceans*, vol. 106, no. C5, pp. 9311–9325, 2001. <https://doi.org/10.1029/2001jc900001>
- [39] G. Masselink, M. Hughes, and J. Knight, *Introduction to Coastal Processes and Geomorphology*. Routledge, 2014.
- [40] R. Boyd, R. Dalrymple, and B. Zaitlin, “Classification of clastic coastal depositional environments,” *Sedimentary Geology*, vol. 80, no. 3–4, pp. 139–150, 1992.
- [41] W. E. Galloway, “Process framework for describing the morphologic and stratigraphic evolution of deltaic depositional systems,” in *Deltas: Models for Exploration*, M. L. Broussard, Ed. Houston Geological Society, 1975, pp. 87–98.
- [42] H. Johnson and C. Baldwin, “Shallow siliciclastic seas,” in *Sedimentary Environments and Facies*, H. Reading, Ed. Blackwell, 1986, pp. 229–282.

- [43] M. Olabarrieta, J. C. Warner, and N. Kumar, “Wave-current interaction in Willapa Bay,” *Journal of Geophysical Research*, vol. 116, no. C12, 2011. <https://doi.org/10.1029/2011jc007387>
- [44] G. Dodet, X. Bertin, N. Bruneau, A. B. Fortunato, A. Nahon, and A. Roland, “Wave-current interactions in a wave-dominated tidal inlet,” *Journal of Geophysical Research: Oceans*, vol. 118, no. 3, pp. 1587–1605, 2013. <https://doi.org/10.1002/jgrc.20146>
- [45] F. Sabatier, O. Samat, A. Ullmann, and S. Suanez, “Connecting large-scale coastal behaviour with coastal management of the rhône delta,” *Geomorphology*, vol. 107, no. 1-2, pp. 79–89, 2009. <https://doi.org/10.1016/j.geomorph.2006.09.026>
- [46] D. A. Edmonds and R. L. Slingerland, “Mechanics of river mouth bar formation: Implications for the morphodynamics of delta distributary networks,” *Journal of Geophysical Research*, vol. 112, no. F2, 2007. <https://doi.org/10.1029/2006jf000574>
- [47] W. Nardin and S. Fagherazzi, “The effect of wind waves on the development of river mouth bars,” *Geophysical Research Letters*, vol. 39, no. 12, 2012. <https://doi.org/10.1029/2012gl051788>
- [48] W. Nardin, G. Mariotti, D. A. Edmonds, R. Guercio, and S. Fagherazzi, “Growth of river mouth bars in sheltered bays in the presence of frontal waves,” *Journal of Geophysical Research: Earth Surface*, vol. 118, no. 2, pp. 872–886, 2013. <https://doi.org/10.1002/jgrf.20057>
- [49] E. J. Anthony, “Wave influence in the construction, shaping and destruction of river deltas: A review,” *Marine Geology*, vol. 361, pp. 53–78, 2015. <http://dx.doi.org/10.1016/j.margeo.2014.12.004>
- [50] S.-K. Liu and J. J. Leendertse, “Multidimensional numerical modeling of estuaries and coastal seas,” in *Advances in Hydroscience*. Elsevier, 1978, pp. 95–164. <https://doi.org/10.1016/B978-0-12-021811-0.50007-3>
- [51] B. H. Johnson, “Numerical modeling of estuarine hydrodynamics on a boundary-fitted coordinate system,” *Applied Mathematics and Computation*, vol. 10-11, pp. 409–436, 1982. [http://dx.doi.org/10.1016/0096-3003\(82\)90200-4](http://dx.doi.org/10.1016/0096-3003(82)90200-4)
- [52] Y. P. Sheng, “On modeling three-dimensional estuarine and marine hydrodynamics,” in *Three-Dimensional Models of Marine and Estuarine Dynamics*. Elsevier, 1987, pp. 35–54. [https://doi.org/10.1016/S0422-9894\(08\)70441-0](https://doi.org/10.1016/S0422-9894(08)70441-0)

## Bibliography

- [53] K. Haas, I. Svendsen, and M. Haller, “Numerical modeling of nearshore circulation on a barred beach with rip channels,” in *Coastal Engineering 1998*. American Society of Civil Engineers, 1999. <https://doi.org/10.1061/9780784404119.059>
- [54] R. A. Falconer, “Numerical modeling of tidal circulation in harbors,” *Journal of the Waterway, Port, Coastal and Ocean Division*, vol. 106, no. 1, pp. 31–48, 1980.
- [55] C.-H. Pan, B.-Y. Lin, and X.-Z. Mao, “Case study: Numerical modeling of the tidal bore on the Qiantang River, China,” *Journal of Hydraulic Engineering*, vol. 133, no. 2, pp. 130–138, 2007. [https://doi.org/10.1061/\(ASCE\)0733-9429\(2007\)133:2\(130\)](https://doi.org/10.1061/(ASCE)0733-9429(2007)133:2(130))
- [56] Z. Defne, K. A. Haas, and H. M. Fritz, “Numerical modeling of tidal currents and the effects of power extraction on estuarine hydrodynamics along the Georgia coast, USA,” *Renewable Energy*, vol. 36, no. 12, pp. 3461–3471, 2011. <https://doi.org/10.1016/j.renene.2011.05.027>
- [57] R. Ranasinghe, C. Pattiaratchi, and G. Masselink, “A morphodynamic model to simulate the seasonal closure of tidal inlets,” *Coastal Engineering*, vol. 37, no. 1, pp. 1–36, 1999. [https://doi.org/10.1016/S0378-3839\(99\)00008-3](https://doi.org/10.1016/S0378-3839(99)00008-3)
- [58] H. T. Özkan Haller and Y. Li, “Effects of wave-current interaction on shear instabilities of longshore currents,” *Journal of Geophysical Research*, vol. 108, no. C5, 2003. <https://doi.org/10.1029/2001jc001287>
- [59] X. Bertin, A. B. Fortunato, and A. Oliveira, “A modeling-based analysis of processes driving wave-dominated inlets,” *Continental Shelf Research*, vol. 29, no. 5-6, pp. 819–834, 2009. <https://doi.org/10.1016/j.csr.2008.12.019>
- [60] J. J. Stoker, *Water Waves: The Mathematical Theory with Applications*, Wiley-Interscience, Ed. John Wiley & Sons, 1992. <https://doi.org/10.1002/9781118033159>
- [61] G. B. Whitham, *Linear and Nonlinear Waves*. John Wiley & Sons, 1999. <http://eu.wiley.com/WileyCDA/WileyTitle/productCd-0471359424.html>
- [62] E. F. Toro, *Riemann Solvers and Numerical Methods for Fluid Dynamics*. Springer-Verlag GmbH, 2009. <http://www.springer.com/in/book/9783540252023>

- [63] M. E. Vázquez-Cendón, “Improved treatment of source terms in upwind schemes for the shallow water equations in channels with irregular geometry,” *Journal of Computational Physics*, vol. 148, no. 2, pp. 497–526, 1999. <https://doi.org/10.1006/jcph.1998.6127>
- [64] P. Garcia-Navarro and M. Vazquez-Cendon, “On numerical treatment of the source terms in the shallow water equations,” *Computers & Fluids*, vol. 29, no. 8, pp. 951–979, 2000. [https://doi.org/10.1016/s0045-7930\(99\)00038-9](https://doi.org/10.1016/s0045-7930(99)00038-9)
- [65] J. Zhou, D. Causon, C. Mingham, and D. Ingram, “The surface gradient method for the treatment of source terms in the shallow-water equations,” *Journal of Computational Physics*, vol. 168, no. 1, pp. 1–25, 2001. <https://doi.org/10.1006/jcph.2000.6670>
- [66] J. Murillo and P. García-Navarro, “Weak solutions for partial differential equations with source terms: Application to the shallow water equations,” *Journal of Computational Physics*, vol. 229, no. 11, pp. 4327–4368, 2010. <https://doi.org/10.1016/j.jcp.2010.02.016>
- [67] M. S. Longuet-Higgins, “Longshore currents generated by obliquely incident sea waves: 1,” *Journal of Geophysical Research*, vol. 75, no. 33, pp. 6778–6789, 1970. <https://doi.org/10.1029/jc075i033p06778>
- [68] G. Watson, T. Barnes, and D. Peregrine, “The generation of low-frequency waves by a single wave group incident on a beach,” in *Coastal Engineering 1994*. American Society of Civil Engineers, 1995. <https://doi.org/10.1061/9780784400890.058>
- [69] F. M. Exner, *Zur physik der dünen*. Hölder, 1920.
- [70] F. M. Exner, “Über die wechselwirkung zwischen wasser und geschiebe in flussen,” *Akad. Wiss. Wien Math. Naturwiss. Klasse*, vol. 134, no. 2a, pp. 165–204, 1925.
- [71] S. Leliavsky, *An Introduction to Fluvial Hydraulics*. Constable, 1955. <https://books.google.com/books?id=-yQISWEACAAJ>
- [72] J. Fredsøe and R. Deigaard, *Mechanics Of Coastal Sediment Transport*, ser. Advanced Series on Ocean Engineering. World Scientific, 1992, vol. 3. <http://www.worldscientific.com/worldscibooks/10.1142/1546>
- [73] J. Fredsøe, “Modelling of non-cohesive sediment transport processes in the marine environment,” *Coastal Engineering*, vol. 21, no. 1-3, pp. 71–103, 1993. [https://doi.org/10.1016/0378-3839\(93\)90046-b](https://doi.org/10.1016/0378-3839(93)90046-b)

- [74] A. Grass, *Sediment Transport by Waves and Currents*. University College, London, Dept. of Civil Engineering, 1981. <https://books.google.it/books?id=YU0QAQAIAAJ>
- [75] L. C. van Rijn, “Sediment transport, part i: bed load transport,” *J Hydraul Eng-ASCE*, vol. 110, no. 10, pp. 1431–1456, 1984. [https://doi.org/10.1061/\(ASCE\)0733-9429\(1984\)110:10\(1431\)](https://doi.org/10.1061/(ASCE)0733-9429(1984)110:10(1431))
- [76] L. C. van Rijn, “Sediment transport, part ii: suspended load transport,” *J Hydraul Eng-ASCE*, vol. 110, no. 11, pp. 1613–1641, 1984. [https://doi.org/10.1061/\(ASCE\)0733-9429\(1984\)110:11\(1613\)](https://doi.org/10.1061/(ASCE)0733-9429(1984)110:11(1613))
- [77] B. Camenen and P. Larroudé, “Comparison of sediment transport formulae for the coastal environment,” *Coastal Engineering*, vol. 48, no. 2, pp. 111–132, 2003. [https://doi.org/10.1016/s0378-3839\(03\)00002-4](https://doi.org/10.1016/s0378-3839(03)00002-4)
- [78] D. Pritchard and A. J. Hogg, “On the transport of suspended sediment by a swash event on a plane beach,” *Coastal Engineering*, vol. 52, no. 1, pp. 1–23, 2005. <https://doi.org/10.1016/j.coastaleng.2004.08.002>
- [79] M. Postacchini, M. Brocchini, A. Mancinelli, and M. Landon, “A multi-purpose, intra-wave, shallow water hydro-morphodynamic solver,” *Advances in Water Resources*, vol. 38, pp. 13–26, 2012. <https://doi.org/10.1016/j.advwatres.2011.12.003>
- [80] T. Y. Hou and P. G. LeFloch, “Why nonconservative schemes converge to wrong solutions: error analysis,” *Mathematics of Computation*, vol. 62, no. 206, pp. 497–497, 1994. <https://doi.org/10.1090/s0025-5718-1994-1201068-0>
- [81] L. Fraccarollo and H. Capart, “Riemann wave description of erosional dam-break flows,” *Journal of Fluid Mechanics*, vol. 461, 2002. <https://doi.org/10.1017/s0022112002008455>
- [82] C. Savary and Y. Zech, “Boundary conditions in a two-layer geomorphological model. application to a hydraulic jump over a mobile bed,” *Journal of Hydraulic Research*, vol. 45, no. 3, pp. 316–332, 2007. <https://doi.org/10.1080/00221686.2007.9521766>
- [83] X. Liu, B. Landry, and M. García, “Two-dimensional scour simulations based on coupled model of shallow water equations and sediment transport on unstructured meshes,” *Coastal Engineering*, vol. 55, no. 10, pp. 800–810, 2008. <https://doi.org/10.1016/j.coastaleng.2008.02.012>
- [84] M. Postacchini, I. K. Othman, M. Brocchini, and T. E. Baldock, “Sediment transport and morphodynamics generated by a dam-break swash

- uprush: Coupled vs uncoupled modeling,” *Coastal Engineering*, vol. 89, pp. 99–105, 2014. <https://doi.org/10.1016/j.coastaleng.2014.04.003>
- [85] E. F. Toro, “Riemann problems and the WAF method for solving the two-dimensional shallow water equations,” *Philosophical Transactions of the Royal Society A: Mathematical, Physical and Engineering Sciences*, vol. 338, no. 1649, pp. 43–68, 1992. <https://doi.org/10.1098/rsta.1992.0002>
- [86] E. F. Toro, *Shock-Capturing Methods for Free-Surface Flows*. John Wiley & Sons, 2001. <http://eu.wiley.com/WileyCDA/WileyTitle/productCd-0471987662,subjectCd-MA20.html>
- [87] E. F. Toro, “A weighted average flux method for hyperbolic conservation laws,” *Proceedings of the Royal Society A: Mathematical, Physical and Engineering Sciences*, vol. 423, no. 1865, pp. 401–418, 1989. <https://doi.org/10.1098/rspa.1989.0062>
- [88] G. Watson, D. Peregrine, and E. Toro, “Numerical solution of the shallow-water equations on a beach using the weighted average flux method,” *Computational Fluid Dynamics '92*, 1992.
- [89] L. Fraccarollo and E. F. Toro, “Experimental and numerical assessment of the shallow water model for two-dimensional dam-break type problems,” *Journal of Hydraulic Research*, vol. 33, no. 6, pp. 843–864, 1995. <https://doi.org/10.1080/00221689509498555>
- [90] E. Toro, “The riemann problem in computational science,” in *Numerical Methods for Hyperbolic Equations*. CRC Press, 2012, pp. 87–103. <https://doi.org/10.1201/b14172-10>
- [91] R. Courant and D. Hilbert, *Methods of Mathematical Physics, Volume 2: Differential Equations*. John Wiley & Sons, 1991. <http://eu.wiley.com/WileyCDA/WileyTitle/productCd-0471504394.html>
- [92] S. K. Godunov, “A difference method for numerical calculation of discontinuous solutions of the equations of hydrodynamics,” *Matematicheskii Sbornik*, vol. 89, no. 3, pp. 271–306, 1959.
- [93] A. Harten, “High resolution schemes for hyperbolic conservation laws,” *Journal of Computational Physics*, vol. 49, no. 3, pp. 357–393, 1983. [https://doi.org/10.1016/0021-9991\(83\)90136-5](https://doi.org/10.1016/0021-9991(83)90136-5)
- [94] P. K. Sweby, “High resolution schemes using flux limiters for hyperbolic conservation laws,” *SIAM Journal on Numerical Analysis*, vol. 21, no. 5, pp. 995–1011, 1984. <https://doi.org/10.1137/0721062>

## Bibliography

- [95] M. Brocchini, I. Svendsen, R. Prasad, and G. Bellotti, “A comparison of two different types of shoreline boundary conditions,” *Computer Methods in Applied Mechanics and Engineering*, vol. 191, no. 39-40, pp. 4475–4496, 2002. [https://doi.org/10.1016/s0045-7825\(02\)00392-4](https://doi.org/10.1016/s0045-7825(02)00392-4)
- [96] M. Postacchini, “Numerical hydro-morphodynamic 2DH model for the shallow waters,” Ph.D. dissertation, Università Politecnica delle Marche, 2011.
- [97] D. M. Kelly and N. Dodd, “Beach-face evolution in the swash zone,” *Journal of Fluid Mechanics*, vol. 661, pp. 316–340, 2010. <https://doi.org/10.1017/s0022112010002983>
- [98] E. Meyer-Peter and R. Müller, “Formulas for bed-load transport.” IAHR, 1948.
- [99] G. Besio, P. Blondeaux, and P. Frisina, “A note on tidally generated sand waves,” *Journal of Fluid Mechanics*, vol. 485, pp. 171–190, 2003. <https://doi.org/10.1017/S0022112003004415>
- [100] B. Camenen and M. Larson, “A general formula for non-cohesive suspended sediment transport,” *Journal of Coastal Research*, vol. 243, pp. 615–627, 2008. <https://doi.org/10.2112/06-0694.1>
- [101] B. Launder and D. Spalding, “The numerical computation of turbulent flows,” *Computer Methods in Applied Mechanics and Engineering*, vol. 3, no. 2, pp. 269–289, 1974. [https://doi.org/10.1016/0045-7825\(74\)90029-2](https://doi.org/10.1016/0045-7825(74)90029-2)
- [102] L. Prandtl, “Bericht über Untersuchungen zur ausgebildeten Turbulenz,” *Zeitschrift für Angewandte Mathematik und Mechanik*, vol. 5, no. 2, pp. 136–139, 1925. [https://doi.org/10.1007/978-3-662-11836-8\\_57](https://doi.org/10.1007/978-3-662-11836-8_57)
- [103] C. W. Hirt, “Computer studies of time-dependent turbulent flows,” *Physics of Fluids (Supplement II)*, vol. 12, no. 12, pp. 219–227, 1969. <https://doi.org/10.1063/1.1692441>
- [104] U. Piomelli, “Large-eddy simulation: achievements and challenges,” *Progress in Aerospace Sciences*, vol. 35, no. 4, pp. 335–362, 1999. [https://doi.org/10.1016/s0376-0421\(98\)00014-1](https://doi.org/10.1016/s0376-0421(98)00014-1)
- [105] C. Keylock, R. Hardy, D. Parsons, R. Ferguson, S. Lane, and K. Richards, “The theoretical foundations and potential for large-eddy simulation (LES) in fluvial geomorphic and sedimentological research,” *Earth-Science Reviews*, vol. 71, no. 3-4, pp. 271–304, 2005. <https://doi.org/10.1016/j.earscirev.2005.03.001>

- [106] C.-H. Moeng and P. Sullivan, “Large-eddy simulation,” in *Encyclopedia of Atmospheric Sciences*. Elsevier, 2015, pp. 232–240. <https://doi.org/10.1016/b978-0-12-382225-3.00201-2>
- [107] J. C. McWilliams, “The emergence of isolated coherent vortices in turbulent flow,” *Journal of Fluid Mechanics*, vol. 146, pp. 21–43, 1984. <https://doi.org/10.1017/S0022112084001750>
- [108] O. Bühler, “On the vorticity transport due to dissipating or breaking waves in shallow-water flow,” *Journal of Fluid Mechanics*, vol. 407, pp. 235–263, 2000. <https://doi.org/10.1017/s0022112099007508>
- [109] M. Brocchini, A. Kennedy, L. Soldini, and A. Mancinelli, “Topographically controlled, breaking-wave-induced macrovortices. part 1. widely separated breakwaters,” *Journal of Fluid Mechanics*, vol. 507, pp. 289–307, 2004. <https://doi.org/10.1017/s002211200400878x>
- [110] J. L. Best and A. G. Roy, “Mixing-layer distortion at the confluence of channels of different depth,” *Nature*, vol. 350, no. 6317, pp. 411–413, 1991. <https://doi.org/10.1038/350411a0>
- [111] J. M. Gaudet and A. G. Roy, “Effect of bed morphology on flow mixing length at river confluences,” *Nature*, vol. 373, no. 6510, pp. 138–139, 1995. <https://doi.org/10.1038/373138a0>
- [112] A. Provenzale, “Transport by coherent barotropic vortices,” *Annual Review of Fluid Mechanics*, vol. 31, pp. 55–93, 1999. <https://doi.org/10.1146/annurev.fluid.31.1.55>
- [113] R. Mazumder, “Turbulence–particle interactions and their implications for sediment transport and bedform mechanics under unidirectional current: some recent developments,” *Earth-Science Reviews*, vol. 50, no. 1–2, pp. 113–124, 2000. [https://doi.org/10.1016/s0012-8252\(00\)00003-9](https://doi.org/10.1016/s0012-8252(00)00003-9)
- [114] M. Lesieur, P. Begou, E. Briand, A. Danet, F. Delcayre, and J. L. Aider, “Coherent-vortex dynamics in large-eddy simulations of turbulence,” *Journal of Turbulence*, vol. 4, 2003. <https://doi.org/10.1088/1468-5248/4/1/016>
- [115] D. Elhmaïdi, A. Provenzale, and A. Babiano, “Elementary topology of two-dimensional turbulence from a lagrangian viewpoint and single-particle dispersion,” *Journal of Fluid Mechanics*, vol. 257, pp. 533–558, 1993. <https://doi.org/10.1017/s0022112093003192>

## Bibliography

- [116] O. Bühler and T. E. Jacobson, “Wave-driven currents and vortex dynamics on barred beaches,” *Journal of Fluid Mechanics*, vol. 449, pp. 313–339, 2001. <https://doi.org/10.1017/s0022112001006322>
- [117] M. F. Yossef and G. J. Klaassen, “Reproduction of groynes-induced river bed morphology using les in a 2-d morphological model,” in *River Flow 2002 - Proceedings of the International Conference on Fluvial Hydraulics, Louvain-la-Neuve, Belgium*, vol. 2, 2002, pp. 1099–1108.
- [118] M. Yossef and H. de Vriend, “Mobile-bed experiments on the exchange of sediment between main channel and groyne fields,” in *River Flow 2004*. CRC Press, 2004, pp. 127–133. <https://doi.org/10.1201/b16998-17>
- [119] L. Soldini, A. Piattella, A. Mancinelli, R. Bernetti, and M. Brocchini, “Macrovortices-induced horizontal mixing in compound channels,” *Ocean Dynamics*, vol. 54, no. 3-4, 2004. <https://doi.org/10.1007/s10236-003-0057-4>
- [120] B. C. van Prooijen, J. A. Battjes, and W. S. J. Uijttewaal, “Momentum exchange in straight uniform compound channel flow,” *Journal of Hydraulic Engineering*, vol. 131, no. 3, pp. 175–183, 2005. [https://doi.org/10.1061/\(ASCE\)0733-9429\(2005\)131:3\(175\)](https://doi.org/10.1061/(ASCE)0733-9429(2005)131:3(175))
- [121] G. Grosso, M. Brocchini, and A. Piattella, “Modeling horizontal coastal flows: assessing the role of coastal contributions,” in *Applied and Industrial Mathematics in Italy II*. World Scientific, 2007, pp. 410–421. [https://doi.org/10.1142/9789812709394\\_0036](https://doi.org/10.1142/9789812709394_0036)
- [122] A. Okabe, B. Boots, K. Sugihara, S. N. Chiu, and D. G. Kendall, *Spatial Tessellations*. John Wiley & Sons, Inc., 2000. <https://doi.org/10.1002/9780470317013>
- [123] R. Sibson, “A brief description of natural neighbor interpolation,” in *Interpreting Multivariate Data*. John Wiley & Sons, 1981, pp. 21–36.
- [124] I. Amidror, “Scattered data interpolation methods for electronic imaging systems: a survey,” *Journal of Electronic Imaging*, vol. 11, no. 2, pp. 157–176, 2002. <https://doi.org/10.1117/1.1455013>
- [125] R. Sibson, “A vector identity for the Dirichlet tessellation,” *Mathematical Proceedings of the Cambridge Philosophical Society*, vol. 87, no. 1, pp. 151–155, 1980. <https://doi.org/10.1017/s0305004100056589>
- [126] A. Savitzky and M. J. Golay, “Smoothing and differentiation of data by simplified least squares procedures,” *Analytical Chemistry*, vol. 36, no. 8, pp. 1627–1639, 1964. <https://doi.org/10.1021/ac60214a047>

- [127] J. Luo, K. Ying, and J. Bai, “Savitzky–Golay smoothing and differentiation filter for even number data,” *Signal Processing*, vol. 85, no. 7, pp. 1429–1434, 2005. <https://doi.org/10.1016/j.sigpro.2005.02.002>
- [128] L. C. van Rijn, *Principles Of Sediment Transport In Rivers, Estuaries And Coastal Seas*. Aqua Publications, 1993. <https://www.aquapublications.nl/page9.html>
- [129] K. Hasselmann *et al.*, “Measurements of wind wave growth and swell decay during the Joint North Sea Wave Project (JONSWAP),” *Ergänzungsheft zur Deutschen Hydrographischen Zeitschrift Reihe*, vol. 8, no. 12, 1973.
- [130] Y. Goda, *Random Seas and Design of Maritime Structures*. World Scientific, 2010. <https://doi.org/10.1142/7425>
- [131] M. J. Kennish, Ed., *Encyclopedia of Estuaries*. Springer Netherlands, 2016. <https://doi.org/10.1007/978-94-017-8801-4>
- [132] G. H. Jirka, “Shallow jets,” in *Recent Research Advances in the Fluid Mechanics of Turbulent Jets and Plumes*, P. A. Davies and M. J. Valente Neves, Eds. Kluwer Academic Publishers, 1994, pp. 155–175.
- [133] A. Canestrelli, W. Nardin, D. Edmonds, S. Fagherazzi, and R. Slingerland, “Importance of frictional effects and jet instability on the morphodynamics of river mouth bars and levees,” *Journal of Geophysical Research: Oceans*, vol. 119, pp. 509–522, 2014. <https://doi.org/10.1002/2013jc009312>
- [134] W. S. J. Uijttewaal and R. Booij, “Effects of shallowness on the development of free-surface mixing layers,” *Physics of Fluids*, vol. 12, no. 2, pp. 392–402, 2000. <http://dx.doi.org/10.1063/1.870317>
- [135] G. H. Jirka, “Large scale flow structures and mixing processes in shallow flows,” *Journal of Hydraulic Research*, vol. 39, no. 6, pp. 567–573, 2001. <http://dx.doi.org/10.1080/00221686.2001.9628285>
- [136] A. Okubo, “Horizontal dispersion of floatable particles in the vicinity of velocity singularities such as convergences,” *Deep Sea Research and Oceanographic Abstracts*, vol. 17, no. 3, pp. 445–454, 1970. [https://doi.org/10.1016/0011-7471\(70\)90059-8](https://doi.org/10.1016/0011-7471(70)90059-8)
- [137] J. Weiss, “The dynamics of enstrophy transfer in two-dimensional hydrodynamics,” *Physica D: Nonlinear Phenomena*, vol. 48, no. 2-3, pp. 273–294, mar 1991. [https://doi.org/10.1016/0167-2789\(91\)90088-q](https://doi.org/10.1016/0167-2789(91)90088-q)

- [138] D. Peregrine, “Surf zone currents,” *Theoretical and Computational Fluid Dynamics*, vol. 10, no. 1-4, pp. 295–309, 1998. <https://doi.org/10.1007/s001620050065>
- [139] M. Brocchini, A. Russo, J. Calantoni, A. Reed, M. Postacchini, C. Lorenzoni, S. Corvaro, A. Mancinelli, G. Moriconi, and L. Soldini, “A natural-scale study of cohesive sediment transport: The Misa River case,” in *River Flow 2014*. CRC Press, 2014, pp. 843–850. <https://doi.org/10.1201/b17133-115>
- [140] M. Brocchini, J. Calantoni, A. H. Reed, M. Postacchini, C. Lorenzoni, A. Russo, A. Mancinelli, S. Corvaro, G. Moriconi, and L. Soldini, “Summertime conditions of a muddy estuarine environment: the EsCoSed project contribution,” *Water Science and Technology*, vol. 71, no. 10, pp. 1451–1457, 2015. <https://doi.org/10.2166/wst.2015.116>
- [141] M. Brocchini, J. Calantoni, M. Postacchini, A. Sheremet, T. Staples, J. Smith, A. H. Reed, E. F. Braithwaite, C. Lorenzoni, A. Russo, S. Corvaro, A. Mancinelli, and L. Soldini, “Comparison between the wintertime and summertime dynamics of the Misa River estuary,” *Marine Geology*, vol. 385, pp. 27–40, 2017. <https://doi.org/10.1016/j.margeo.2016.12.005>
- [142] M. Postacchini, L. Soldini, C. Lorenzoni, and A. Mancinelli, “Medium-term dynamics of a middle Adriatic barred beach,” *Ocean Science*, vol. 13, no. 5, pp. 719–734, 2017. <https://doi.org/10.5194/os-13-719-2017>
- [143] J. A. Puleo and T. Butt, “The first international workshop on swash-zone processes,” *Continental Shelf Research*, vol. 26, no. 5, pp. 556–560, 2006. <https://doi.org/10.1016/j.csr.2006.01.008>
- [144] J. A. Puleo and A. Torres-Freyermuth, “The second international workshop on swash-zone processes,” *Coastal Engineering*, vol. 115, pp. 1–7, 2016. <https://doi.org/10.1016/j.coastaleng.2015.09.007>
- [145] M. Barnes and T. Baldock, “A lagrangian model for boundary layer growth and bed shear stress in the swash zone,” *Coastal Engineering*, vol. 57, no. 4, pp. 385–396, 2010. <https://doi.org/10.1016/j.coastaleng.2009.11.009>
- [146] T. O'Donoghue, D. Pokrajac, and L. Hondebrink, “Laboratory and numerical study of dambreak-generated swash on impermeable slopes,” *Coastal Engineering*, vol. 57, no. 5, pp. 513–530, 2010. <https://doi.org/10.1016/j.coastaleng.2009.12.007>

- [147] R. Briganti, N. Dodd, D. Pokrajac, and T. O'Donoghue, "Non linear shallow water modelling of bore-driven swash: Description of the bottom boundary layer," *Coastal Engineering*, vol. 58, no. 6, pp. 463–477, 2011. <https://doi.org/10.1016/j.coastaleng.2011.01.004>
- [148] S. Clarke, N. Dodd, and J. Damgaard, "Modeling flow in and above a porous beach," *Journal of Waterway, Port, Coastal, and Ocean Engineering*, vol. 130, no. 5, pp. 223–233, 2004. [https://doi.org/10.1061/\(asce\)0733-950x\(2004\)130:5\(223\)](https://doi.org/10.1061/(asce)0733-950x(2004)130:5(223))
- [149] J. R. Cash and A. H. Karp, "A variable order Runge-Kutta method for initial value problems with rapidly varying right-hand sides," *ACM Transactions on Mathematical Software*, vol. 16, no. 3, pp. 201–222, 1990. <https://doi.org/10.1145/79505.79507>
- [150] W. H. Press, B. P. Flannery, S. A. Teukolsky, and W. T. Vetterling, *Numerical Recipes in Fortran 77: The Art of Scientific Computing*. Cambridge University Press, 1992. <https://goo.gl/HXjwnb>